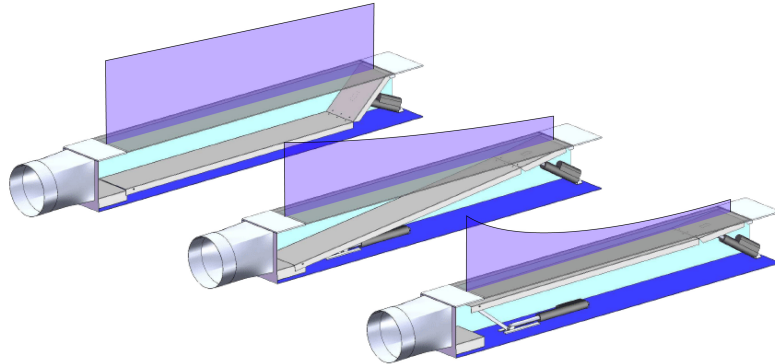Master of Science Thesis

Control of Suction Distributions on Boundary Layer Suction Systems for Automotive Wind Tunnels

Jeroen Bink

August 20, 2008

Actiflow
Removing Boundaries in Aerodynamics

TUDelft
Delft University of Technology

Control of Suction Distributions on Boundary Layer Suction Systems for Automotive Wind Tunnels

MASTER OF SCIENCE THESIS

Master's Thesis at the Faculty of Embedded Systems of the Delft University of Technology for the Degree of Master of Science

Jeroen Bink

August 20, 2008

Committee Members:

dr. ir a.j. van Genderen, supervisor
ir. r. Campe, daily supervisor
dr. ir. k.l.m. Bertels
ir. w.a. Timmer

Faculty of Embedded Systems · Delft University of Technology
Actiflow B.V. · Delft

Abstract

Wind tunnels are used to study airflows around objects like cars, airplanes and ice-skaters. This is done, simulating the real world, by blowing an airflow over a fixed body. In the real situation an object moves through the air, while in a wind tunnel it is the air that is moving. So a wind tunnel needs to generate an airflow. In this airflow, at the walls of the wind tunnel, an undesired effect occurs called *boundary layer development*. A thin layer of air is retarded due to friction of the airflow with the walls of the tunnel. In an automotive wind tunnel, which simulates airflows around cars, this boundary layer will also develop over the ground plane under the car. Because this boundary layer is not present on the road, this ground plane boundary layer should be minimized for accurate simulations. To minimize the ground plane boundary layer many techniques are implemented in wind tunnels and one of them is boundary layer suction. With boundary layer suction, a suction section in the wind tunnel floor removes, or partly removes, the boundary layer by sucking air away from the main airflow. This suction section is the main subject of this master thesis. Research will be done on a new suction system with an adaptive suction duct geometry. It will explore the possibilities to control the suction speed distribution on this suction system by adapting the geometry of the duct by actuators.

A model of a system with an adaptive geometry is made based on the physical properties of the airflow in the duct. This model is verified by measurements on a test setup. It is found that different control techniques can be used to control the suction speed distribution of the airflow through a porous material. The capabilities of the controlled system are quantified for wind tunnel integration.

Preface

This research is done as a master thesis project for the master Embedded Systems at the Delft University of Technology. The research is done in association with Actiflow B.V. Actiflow is a spin off company of the TU Delft and is specialized in active aerodynamics. The system presented in this research is a new boundary layer reduction system.

During this research this system is patented by Actiflow[12]. The research was supervised by Eric Terry and Roy Campe, management of Actiflow. Oskar van Dijk was responsible for the design and production of the test section used in this research. Thanks go to all people who supported this research.
Special thanks go to Eric, Roy, Oskar, Jorrit, Bart, Vincent, Roland and Okke.

<div align="right">

Jeroen Bink
19 augustus 2008

</div>

Table of Contents

List of Figures

List of Symbols

1 Latin symbols

p	pressure	Pascal
p_x	pressure component	Pascal
p_y	pressure component	Pascal
T	temperature	Kelvin
U_∞	free stream velocity	m/s
p_∞	reference static pressure	Pascal
q	dynamic pressure	Pascal
q_∞	reference dynamic pressure	Pascal
C_p	static pressure	Pascal
T_u	turbulence level	
$S0, S1, S2$	positions on plates	(x, y)
A_s	area of porous surface	m^2
A	area of duct cross section	m^2
V	in duct flow speed	m/s
V_s	porous surface flow speed	m/s
$\dot{m}$	mass flow	kg/s
F_m	momentum flux term	Newton
F_p	pressure force	Newton
F_d	friction force	Newton
R_1	friction factor	kg/m^3
R_2	friction factor	kg/m$^2 s$
n	number of cells	
Kp	proportional gain	
V_A	actuator speed	m/s
S_A	actuator stroke setpoint	mm
S_f	actuator stroke current	mm
R	resistance	Ohm
V	potential difference	Volt
K	gauge factor	

2   Greek symbols

α	plate angle	rad
β	plate angle	rad
δ	boundary layer thickness	mm
δ^*	displacement thickness	mm
ρ	density	kg/m^3
μ	viscosity	

Chapter 1

Introduction

Wind tunnels are used to study airflows around objects like cars, airplanes and ice-skaters. This is done, simulating the real world, by blowing the airflow over a fixed body. In the real situation an object moves through the air, while in a wind tunnel it is the air that is moving. So a wind tunnel needs to generate an airflow. In this airflow, at the walls of the wind tunnel, an undesired effect occurs called *boundary layer development*. A thin layer of air is retarded due to friction of the airflow with the walls of the tunnel. In an automotive wind tunnel, which simulates airflows around cars, this boundary layer will also develop over the ground plane under the car. Because this boundary layer is not present on the road, this ground plane boundary layer should be minimized for accurate simulations. To minimize the ground plane boundary layer many techniques are implemented in wind tunnels and one of them is boundary layer suction. With boundary layer suction, a suction section in the wind tunnel floor removes or partly removes the boundary layer by sucking air away from the main airflow. This suction section is the main subject of this master thesis. Research will be done on a new suction system with an adaptive suction duct geometry. It will explore the possibilities to control the suction speed distribution on this suction system by adapting the geometry of the duct by actuators.

1.1   system description

The proposed system consists of a suction duct. The upper side of the duct consists of a porous material. At the end of the duct a hose with a pump is attached. When the pump is activated it generates an underpressure in the channel, and airflows through the porous material. The rigid bottom plate of the duct can be adjusted in height and in angle in order to locally change the cross section area of the suction channel. This will adjust the pressure gradient in longitudinal direction in the duct and thus the airflow velocity through the porous material. This is illustrated in figure 1.1. When the system is implemented into a wind tunnel, with the porous upper side leveled with the wind tunnel ground plane, it can be used as a boundary layer suction system.
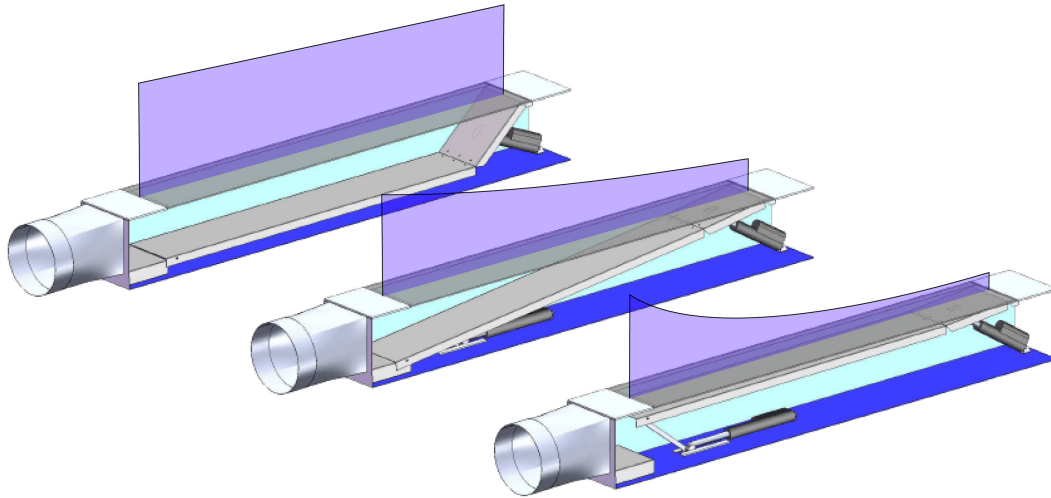
Figure 1.1: examples of suction distributions

1.2   research goals

Before the system can be produced as a wind tunnel suction system, the capabilities of the system need to be clear. Therefore, to study the system' s behaviour, a verified model of the system is needed. This model can be used for control and simulation of the system. The knowledge gained can be used to design a wind tunnel suction system based on the controlled system. Three research goals are recognized here:

1. **a verified model for the system** (chapter 5 and 6)
   A verified model of the proposed system is needed to study the behaviour of the suction system.

2. **comparison between control techniques** (chapter 7 and 8)
   A founded decision on the most suitable control technique for this system needs to be made.

3. **capabilities for wind tunnel integration** (chapter 9)
   The capabilities of the system integrated in a wind tunnel need to be quantified.

This report consists of two parts. The first part describes the context of the research on the new suction system. The second part describes the research itself.

Part I

Research context

Chapter 2

General airflow properties

In any wind tunnel an effect called *boundary layer development* occurs. Because boundary layer reduction is one of the main objectives of this research, this chapter will explain this boundary layer development. Also some basic airflow properties are presented.

2.1 basic airflow properties

The most interesting property of an airflow is its velocity field. In a velocity field a velocity vector (u, v, w) is associated to (x, y, z) points in an airflow. Because most other properties follow directly from the velocity field, determining the velocity field of a flow is often sufficient to solve a flow problem [14]. The velocity field interacts closely with the thermodynamic properties of an airflow;

1. Pressure p

2. Density ρ

3. Temperature T

4. Viscosity μ

Next to the velocity field, the pressure is the most dynamic variable in an airflow. Differences or gradients in pressure often drive an airflow. Density and temperature are directly related.

To describe the mechanical behaviour of a flow, the viscosity of the flow medium is also an important property. The viscosity relates the local stresses in a flow to the strain rate of the fluid element. The viscosity μ of air is $1.8e^{-5} \frac{kg}{m \cdot s}$ at 20 ^{o}C at atmospheric pressure. The viscosity varies with temperature and pressure. It changes only weakly with pressure, and in most problems these variations can be neglected [14]. The temperature however has a stronger effect on the viscosity; the viscosity increases with T for gases, and decreases for liquids.
Especially for wind tunnels, the behaviour of the airflow along the walls is of interest. At the

walls shear stress decreases the speed of the airflow. In common linear or *Newtonian* flows the applied shear stress τ is proportional to the velocity gradient. The constant of proportionality is the viscosity.

$$\tau = \mu \frac{du}{dy}$$
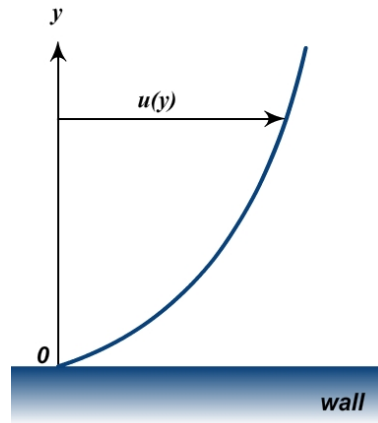
Figure 2.1: velocity profile of a flow near a solid wall

Figure 2.1 illustrates a velocity profile of a flow near a solid wall. The shear stress is proportional to the slope of the velocity profile. At the wall the velocity u is zero relative to the wall. This is called the *no slip* condition and is also characteristic for any Newtonian viscous-fluid flow.

2.2 boundary layer development
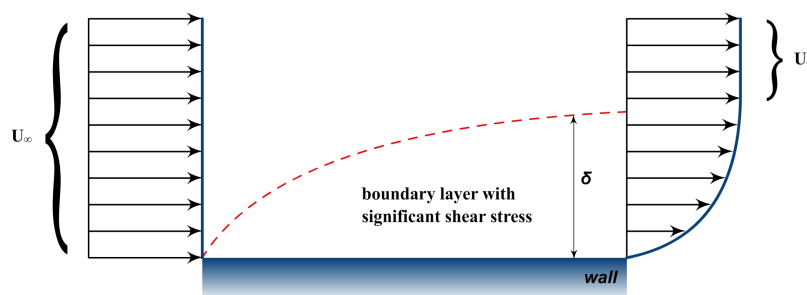
Figure 2.2: boundary layer development over a solid wall

Due to the shear stresses at a plate or a wall parallel to an oncoming flow, a boundary layer develops along the plate as shown in figure 2.2. The velocity of the flow at the wall is zero. Slowly moving particles retard their neighbours so a significant retarded shear layer develops. The oncoming flow of uniform velocity is called the *free stream* U_∞. The boundary layer

thickness, δ, is specified relative to this free stream. In other words the boundary layer is the part of the flow near to the wall where the velocity differs significantly from the free stream velocity. This is quantified by the quotient of the local flow velocity and the free stream velocity u/U_∞. In a wind tunnel, values of 0.99 (99 % of the free stream) are significant.

To quantify the boundary layer also the *displacement thickness*, δ^*, is used. The mathematical definition of the displacement thickness for incompressible flow is given by:

$$\delta* = \frac{1}{U_\infty}\int\limits_0^\delta (U_\infty - u)dz = \int\limits_0^\delta (1 - \frac{u}{U_\infty})dz$$

where U_∞ is the free stream velocity, u is the local flow velocity and z is the height above the ground. The displacement thickness is the deficit of mass flux in the flow due to the velocity loss in the boundary layer of the flow[7]. This is illustrated in figure 2.3.
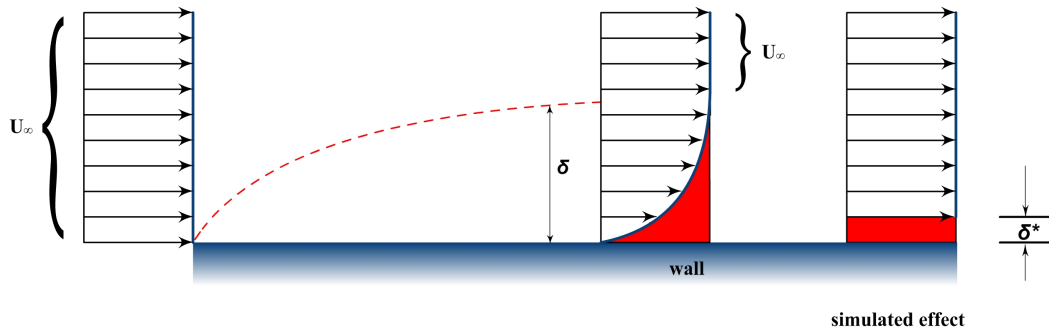
Figure 2.3: displacement thickness

Furthermore, in a wind tunnel, boundary layers develop along the walls of the test section. In case of simulating an airflow around a car, the boundary layer on the ground plane of the wind tunnel prevents a good road simulation. Therefore in automotive wind tunnels this ground plane boundary layer, GPBL, needs to be minimized [4]. Techniques to achieve this reduction are explained in the next chapter.

Chapter 3

Wind tunnels

This chapter will explore the existing boundary layer reduction systems. These systems try to improve the airflow quality in a wind tunnel. The parameters in a wind tunnel that are important for this airflow quality are explained. But first an overview of different wind tunnels and their different test sections is given.

3.1   wind tunnel lay-outs

In basic there are two types of wind tunnels, open and closed circuit wind tunnels. In an open circuit wind tunnel environmental air is being accelerated over a test section by a fan, and at the other end the air is exhausted into the environment. This can be seen in figure 3.1. In a closed circuit wind tunnel the air circulates with no or little exchange of air with the environment. This gives the the following advantages over an open circuit wind tunnel [3]:

1. a closed circuit is more energy efficient, not all the momentum of the airflow is lost into the environment.

2. the flow can be controlled independent of environmental properties like the weather.

3. noise levels can be minimized, as noise and sound waves are undesired pressure fluctuations. Also some aerodynamic measurement techniques are based on sound production (aeroacoustic). For such measurements a closed circuit wind tunnel can be made with less additive noise.

On the other hand, an open circuit wind tunnel is in most cases less expensive to build. Therefore they are mostly seen in schools and universities [3]. Some aerodynamic testing can be done by visualizing airflows with smoke. In this case an open wind tunnel can also have an advantage, because the smoke is exhausted to the environment and does not have to be filtered out.
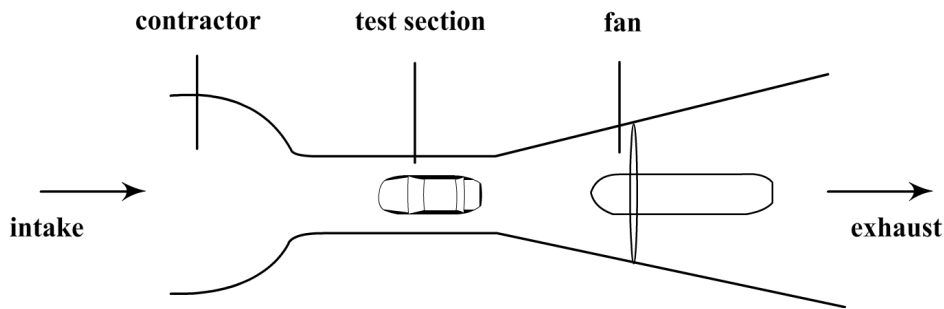
Figure 3.1: open circuit wind tunnel with closed test section

3.2   Test section lay-outs

A wind tunnel test section is the section in which the objects to be tested are placed. Because in this section all the measurements are done, the airflow quality in the test section is most important.

3.2.1   open and closed test sections

Basically both a closed and open circuit wind tunnel have two types of test sections, an open or a closed test section. Figure 3.2 shows a wind tunnel with a closed test section, the test section has solid boundaries. Figure 3.3 shows a wind tunnel with an (semi) open test section where the test section has no solid boundaries, except for the wind tunnel floor [15].
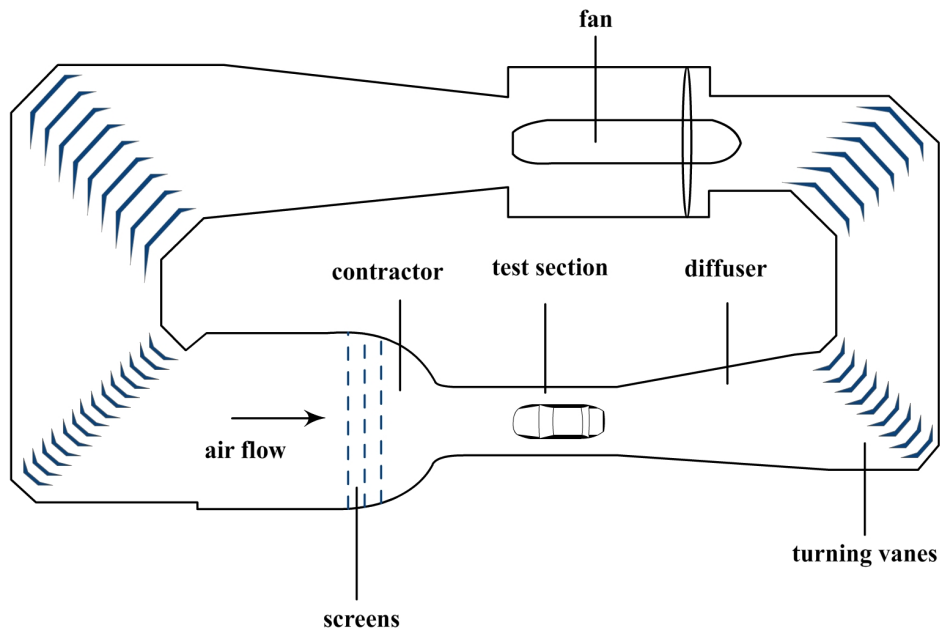
Figure 3.2: closed circuit wind tunnel with closed test section
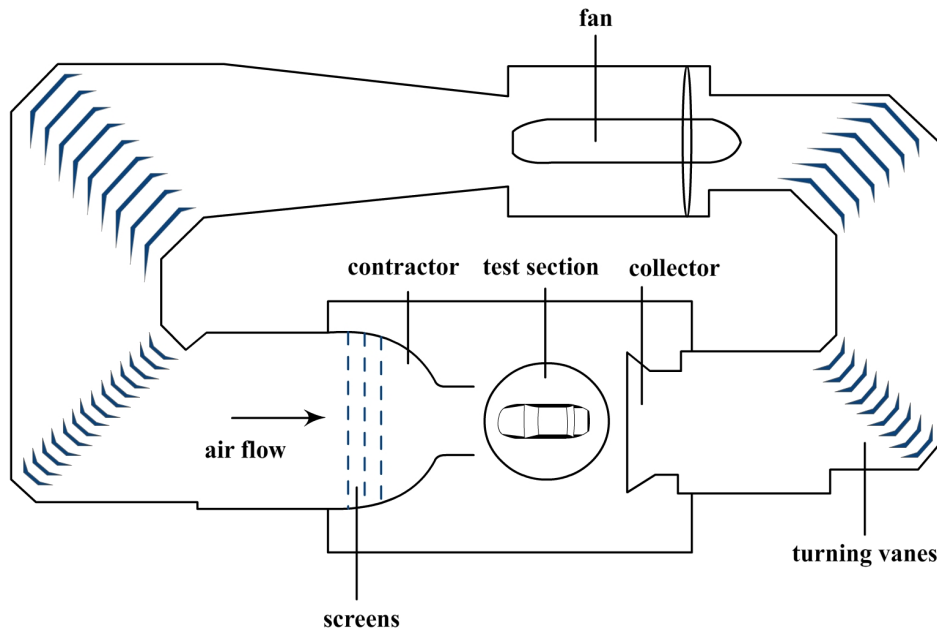
Figure 3.3: closed circuit wind tunnel with open test section

When a car is placed in a closed test section, the walls of the test section have an influence on the airflow. On the road the car does not have these influences besides the influences of the road. One of the influences of the side walls, when an aerodynamic body is placed in the test section, is called the *blockage effect*. This blocking effect causes lower pressures around the aerodynamic body because the airflow in between the body and the walls is accelerated.[13]. On measurements corrections for this blockage effect need to be done. An open test section can reduce this blockage effect, but many open-test section tunnels have experienced severe flow fluctuation problems that require extensive corrective actions [3].

3.2.2 slotted-wall test sections

In between open and closed test section lay-outs, there exist slotted-wall test section lay-outs. In this case multiple slots of constant width are present in the side walls and ceiling of the test section. Under relatively high area blockage levels, the substantial blockage corrections which would be present with solid walls can be effectively eliminated with slots of sufficient open area ratio[13]. A slotted wall configuration is illustrated in figure 3.4. As an example slotted walls are used in wind tunnels of Porsche and Volvo [1].

3.2.3 adaptive-wall test sections

As an alternative, adaptive-wall test sections exists [2]. In this configuration the test section walls may be adapted mechanically to simulate a free-air stream line. This is shown in figure 3.5.

slotted wall test section
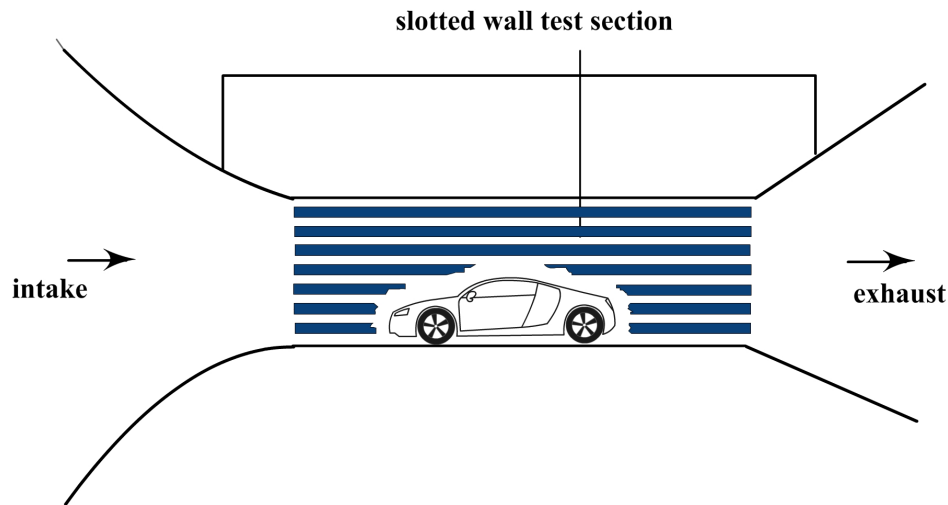
Figure 3.4: slotted wall test section configuration
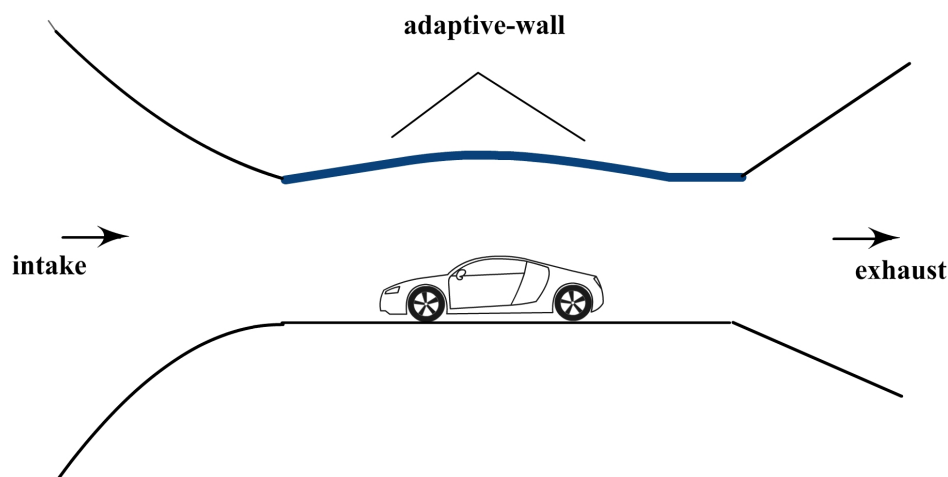
adaptive-wall

Figure 3.5: adaptive wall test section configuration

3.3 Airflow quality in wind tunnels

All wind tunnels are dealing with blowing air over and around aerodynamic bodies. Generating an airflow can be done by a fan or compressor and is not to complex for low-speed airflows (U_∞ < Mach 0.7). The problem however is to deliver a high quality airflow at the test section. A high quality airflow for most wind tunnels is a flow with uniform velocity and pressure distributions at the test section.

As a base for the airflow quality different parameters are considered [1] [3] [13] :

1. velocity uniformity / boundary layer thickness

2. flow angularity

3. static pressure gradient

4. velocity fluctuations in time

5. turbulence level

6. noise levels

3.3.1 velocity uniformity

The velocity uniformity is defined as the percentage deviation of local stream wise velocity, u from the average, free stream velocity value, U_∞.

$$\frac{\Delta u}{U_\infty} \cdot 100\% = \frac{u - U_\infty}{U_\infty} \cdot 100\%$$
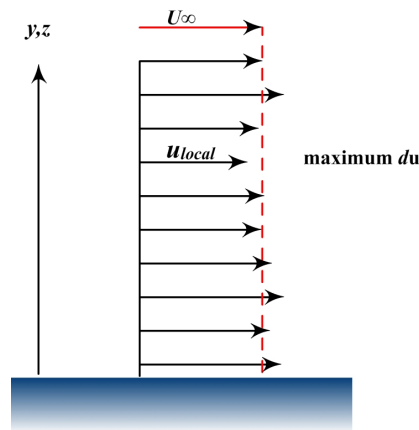
Figure 3.6: velocity uniformity requirement

The maximum relative difference between the average flow velocity and local flow velocities is used as a quantification of the velocity uniformity. This is illustrated in figure 3.6. Typical values of deviation are between ± 0.1 and $\pm 1\%$. These velocity variations are mostly caused by the wind tunnel geometry [1].

3.3.2 boundary layer thickness

As a special case of velocity deviation, the decrease in velocity of the airflow at the walls of the test section is recognized. As said before a wind tunnel facility is a test environment that tries to simulate a real world situation. In a simple wind tunnel, both the model and the ground plane are stationary. In this case a boundary layer develops over the ground plane as explained in section 2.2, in wind tunnel terms called the Ground Plane Boundary Layer (GPBL), which is illustrated in figure 3.7. This shear layer, or boundary layer, is not present on a road and therefore needs to be minimized for automotive wind tunnel simulations to
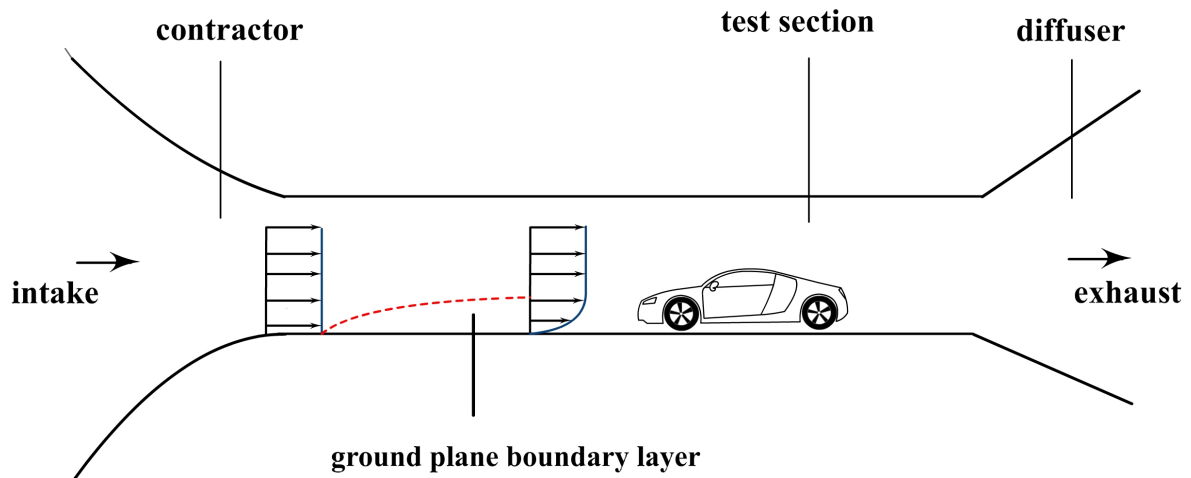
Figure 3.7: the Ground Plane Boundary Layer (GPBL)

obtain correct test results.

Different techniques are developed to reduce the ground plane boundary layer, these are explained in section 3.4.

3.3.3 flow angularity

Velocity components in an other direction than the flow direction, u, can cause undesired forces on the body in the test section of the wind tunnel. This is illustrated in figure 3.8. Pitch angles (w direction) can cause undesired pitch effects on the vehicle. Angles in the yaw direction (v direction) can also generate undesired forces, but can in some circumstances be compensated by yawing the vehicle itself. Acceptable pitch and yaw angles should are below 0.15 degrees in the test section [13].
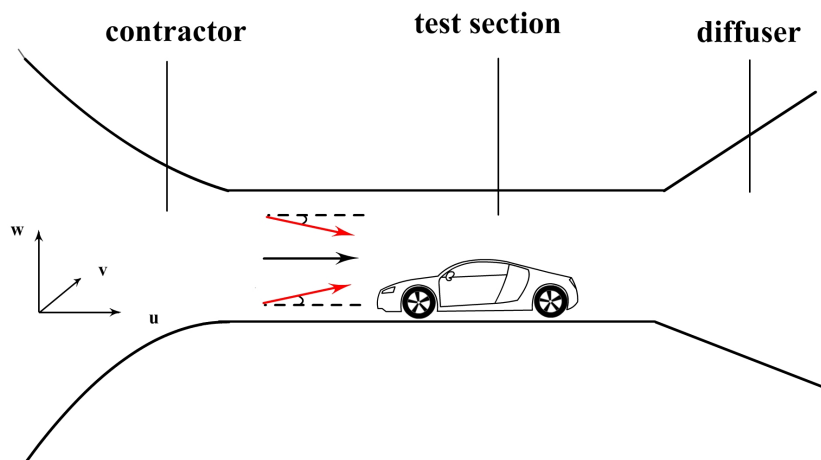
Figure 3.8: local pitch variations in the flow

3.3.4 static pressure gradient
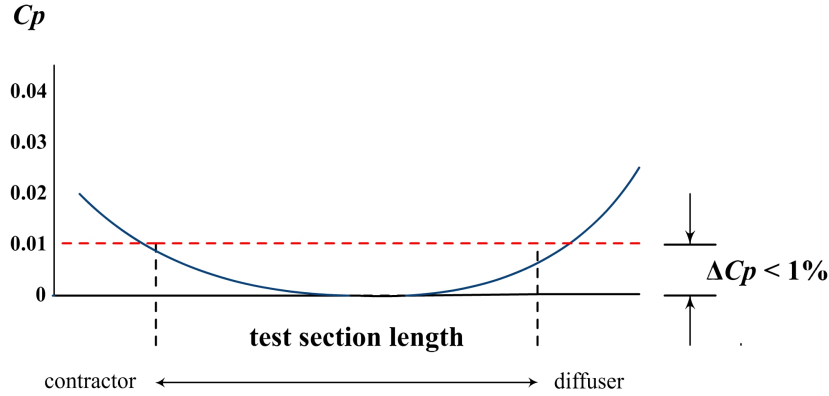
Figure 3.9: static pressure variations in longitudinal direction

Ideally in longitudinal direction of the test section no pressure gradients exists. This is closely related to longitudinal velocity deviations in the flow. Slowing down or speeding up the flow in x direction, causes pressure gradients. The local static pressure variation is defined as the deviation in pressure coefficient from a reference pressure, in the longitudinal direction:

$$Cp = \frac{(p_x - p_\infty)}{q_\infty}$$

with p_x the local static pressure, p_∞ a reference static pressure and q_∞ the reference for the dynamic pressure. The variation of the static pressure coefficient, Cp, is acceptable when less than 1% over the test section (Δ Cp < 0.01)[1]. This is illustrated in figure 3.9.

Causes for static pressure gradients are influences from the boundary layers on all the walls of the tunnel. Also the *blockage effect*, mentioned in section 3.2.1 can cause static pressure gradients [13].

3.3.5 velocity fluctuations in time

Velocity fluctuations are local variations of flow speeds over time. These are mostly caused by the fan's design and operation. It is derived from pressure measurement with pitot-static probes.

3.3.6 turbulence level

The turbulence level, T_u, is defined as the ratio of the root mean square of the local velocities and the free stream velocity, U_∞.

$$T_u = \frac{u_{rms}}{U_\infty} \cdot 100\%$$

With u_{rms} the root mean square of the velocity components.

$$u_{rms} = \sqrt{\frac{1}{3}(u'^2 + v'^2 + w'^2)}$$

The turbulence level quantifies the velocity fluctuations in three directions.

3.3.7   noise levels

Noise consists of pressure fluctuations. The goal is to keep the background noise as low as possible. The noise is mostly generated by the fan and fan motor. In some cases aero-acoustic measurement techniques are used to study flows around bodies. In this case the sound waves that are generated by the airflow around the body are evaluated. A wind tunnel in which these aeroacoustic measurements are done needs to be free of environmental noise.

3.4   Boundary layer control techniques in wind tunnels

In a wind tunnel 3 zones of different near ground flow control can be described [10] This is shown in figure 3.10.
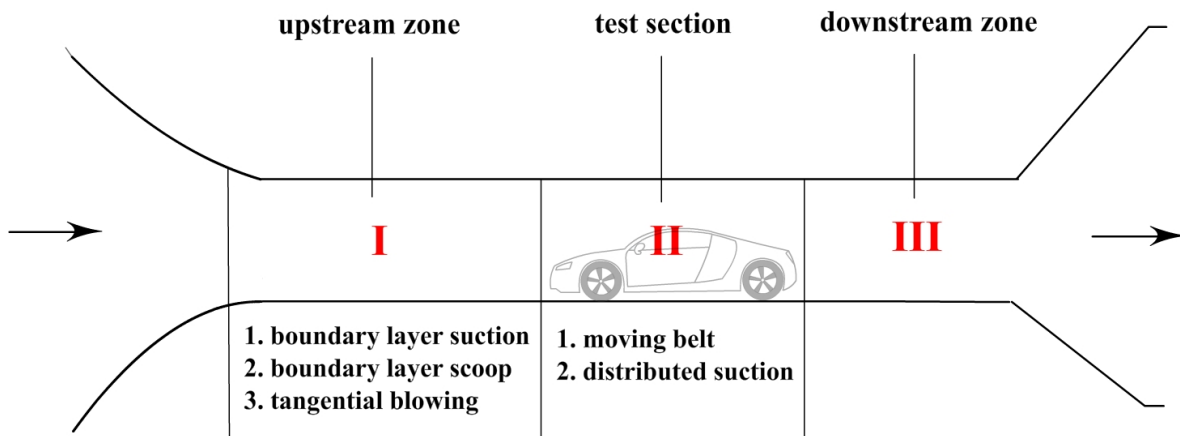
Figure 3.10: flow control techniques in different regions of a wind tunnel

The first zone, referred as the upstream zone, is the area upstream of the test section where the boundary layer starts to develop. The second zone is the test section itself where the body to be tested is placed and a boundary layer develops (further) under the object. The third zone, downstream the test section is also an important zone for the behaviour of the airflow, but less interesting in terms of boundary layer reduction.

In this research boundary layer control at the upstream zone (I) is of special interest. However because it affects the flow at the test section itself also techniques used to control the airflow at the test section are globally explored. At the test section the term *ground simulation* is mostly used, in the upstream zone the term *boundary layer control* is preferred although the two are closely related [10].

3.4.1 test section ground simulation

moving belt

At the test section the relative motion between the road and the vehicle has to be simulated. This is almost perfectly achieved by means of a moving belt [10][6], which is shown in figure 3.11. This technique however, requires the removal of the approaching boundary layer in front of the belt in order to avoid boundary layer relaxation on the moving belt.
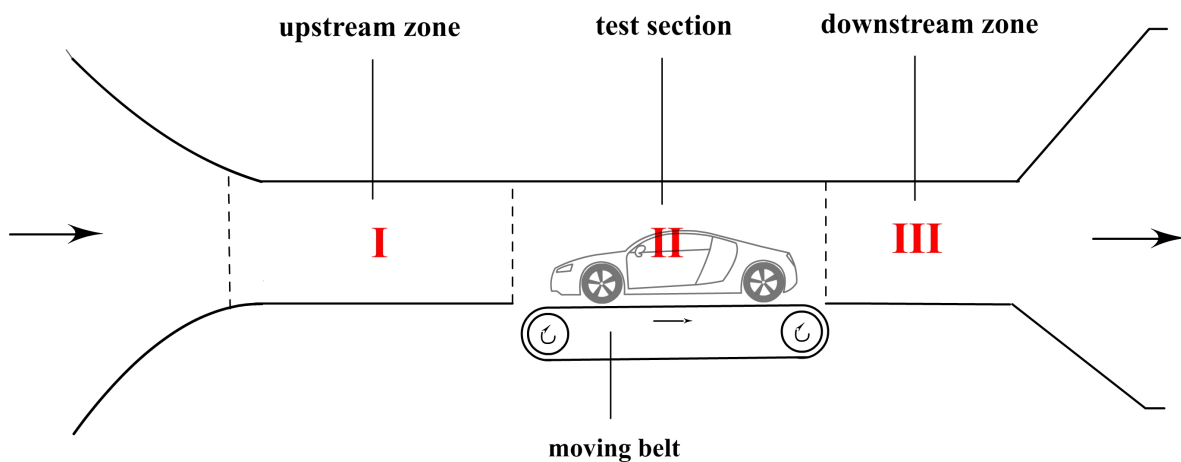
Figure 3.11: location of ground simulation by a moving belt

Although a moving belt is a very good simulation of the real world movement between a car and a road, it is complex to construct and needs intensive maintenance. Other problems are due to finite belt dimensions, belt stability (flutter) and dynamic pressure calibration. As an alternative, tangential blowing or distributed suction is used [1].

distributed suction

Distributed suction uses a stationary ground plane, but in this case the ground plane is made porous and air from the boundary layer is sucked away from the test section, which can be seen in figure 3.12. At the test section (II) these systems are tuned for ground simulation which includes some form of boundary layer control. This research is mostly concentrated on systems controlling the boundary layer in front of the test section (I). This boundary layer control is further explored in the next section.
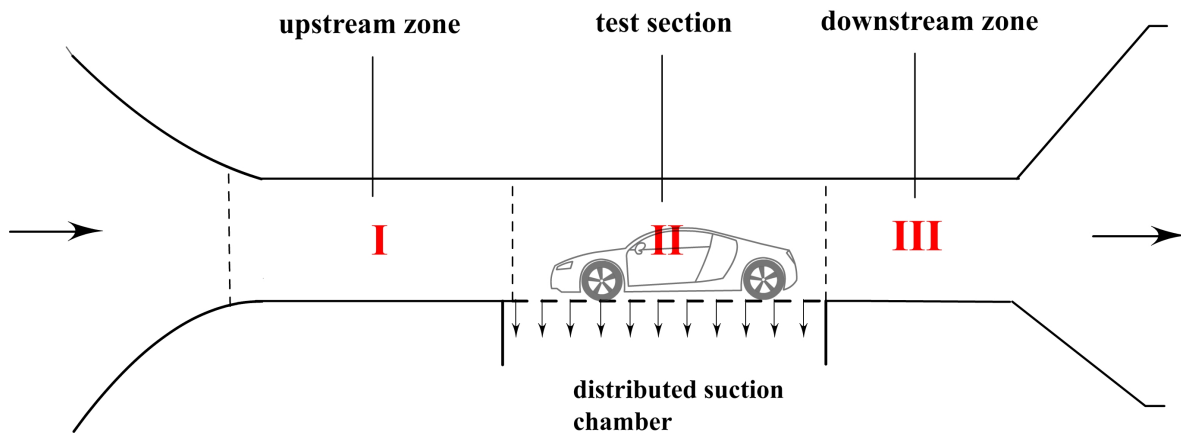
Figure 3.12: location of ground simulation by distributed suction

3.4.2 upstream zone boundary layer control

To minimize the approaching boundary layer several techniques are applied in different wind tunnels including [9]:

1. boundary layer scoop

2. tangential blowing

3. boundary layer suction

boundary layer scoop
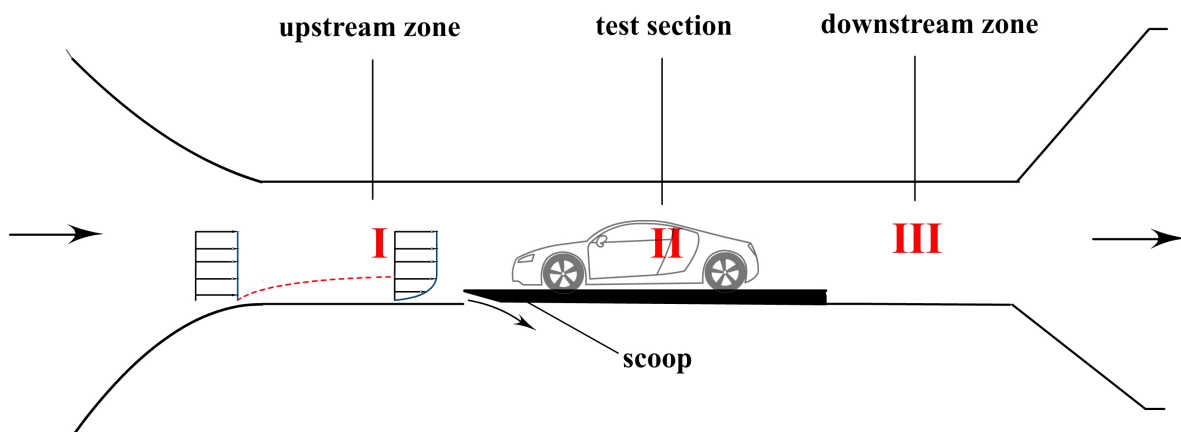
Figure 3.13: boundary layer control by scoop

For many applications without special interest in the vehicle's underside, it is generally sufficient to use a stationary ground board with a scoop to peel off the oncoming boundary layer [1] as can be seen in figure 3.13.

tangential blowing

With tangential blowing a thin high-momentum wall jet is blown into the lower part of the boundary layer. Depending on the momentum ratio between jet and boundary layer the displacement thickness of the combination can be adjusted to zero. However, this technique requires costly technical effort in full scale facilities [10]. This is mainly because the velocity of the jet has to be multiple times the velocity of the free stream velocity [1] [7]. The tangential blowing technique is illustrated in figure 3.14.
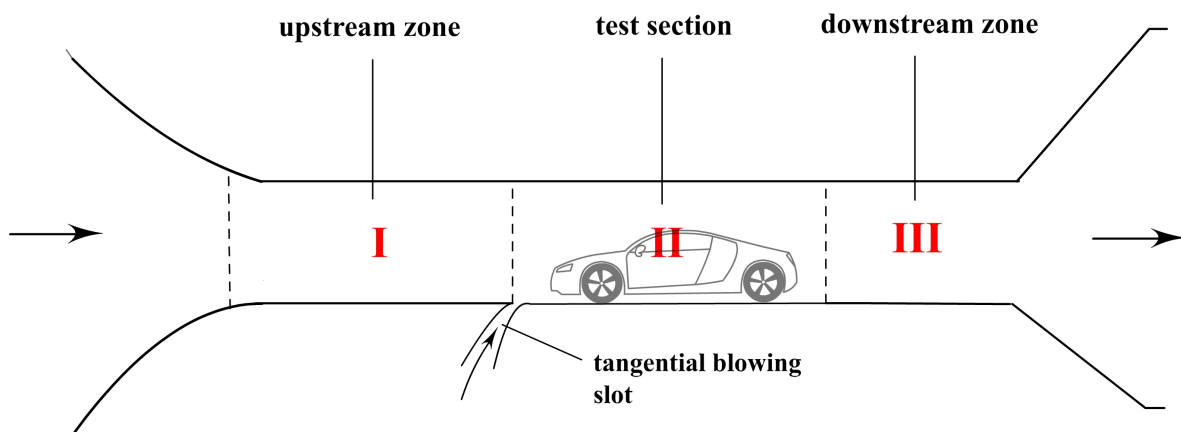
Figure 3.14: location of ground simulation by tangential blowing

boundary layer suction

Boundary layer suction in front of the test section is often referred to as boundary layer pre-suction. Air from the boundary layer is sucked away by a suction section at one location illustrated in figure 3.15. The boundary layer can be removed completely (after the suction section) when enough air is sucked away. Of course after the suction section, a new boundary layer will start to develop [5].

Removing the boundary layer by suction has some side effects. The consequence of boundary layer pre-suction is an additional pressure gradient in front of the model [7] [16]. This is illustrated in figure 3.16. To minimize the additional pressure gradient the model could be moved toward the diffuser and therefore away from the additional gradient. Alternatively the relative suction velocity could be reduced. Both these measures have the disadvantage of a thicker boundary layer[16].
Another consequence of boundary layer suction is undesired flow angles relative to the stream direction. Air that is removed from the boundary layer is replaced by free stream air from above and this causes pitch angles in the main air stream.

To reduce the undesired pressure gradient and angularity effects, another approach could be chosen. As said before these effects could be reduced by placing the vehicle further away from the suction section. The disadvantage of this approach is that a new boundary layer develops in between the suction section and the vehicle. This boundary layer, could be sucked
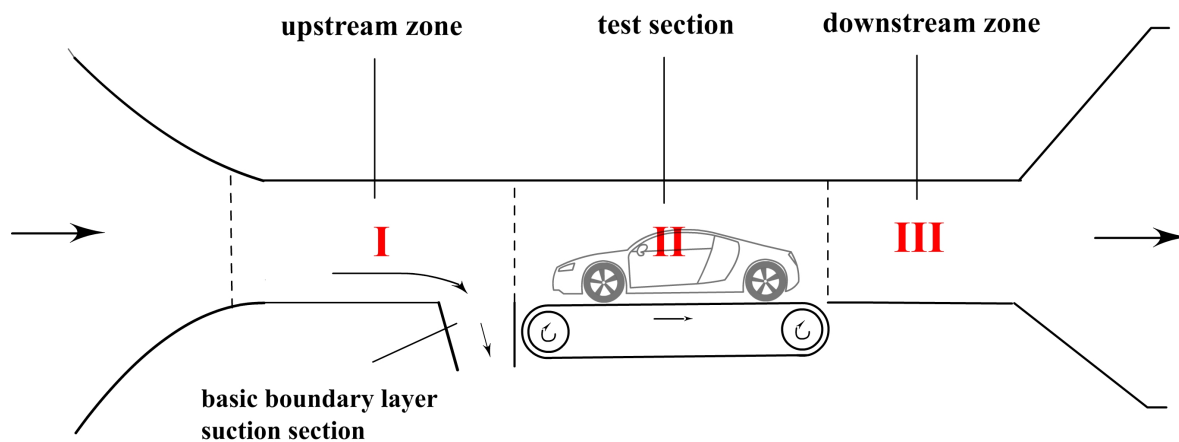
Figure 3.15: basic boundary layer suction
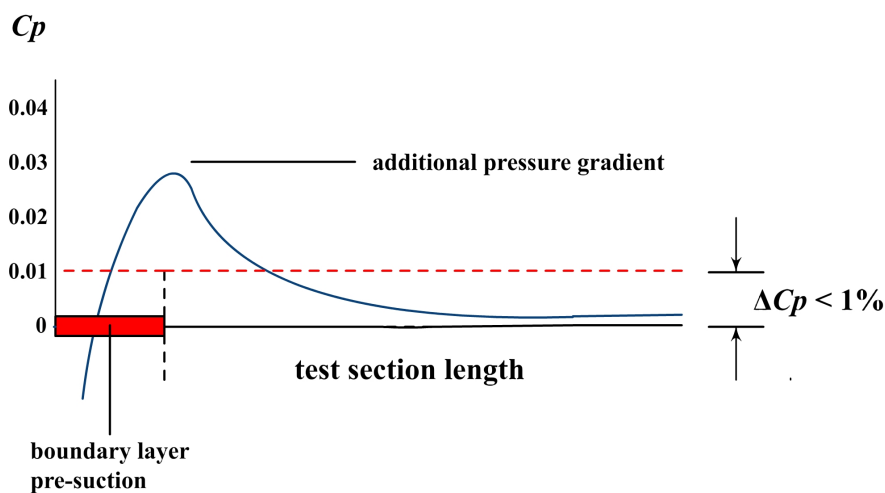
Figure 3.16: additional static pressure gradient in front of the test section due to boundary layer pre suction

away again, at a lower suction speed. A suction section with a gradient in suction speed could minimize the angularity and pressure gradient effects, and find a balance between those effects and the boundary layer thickness. This is illustrated in figure 3.17.

The balance between undesired effects and boundary layer thickness can be different for different measurements. Also the gradient needed is hard to compute. A system which is capable of producing different suction speed distributions, and can be adapted to tune the system is the subject of the the research described in the second part of the report.

upstream zone   test section   downstream zone

I   II   III
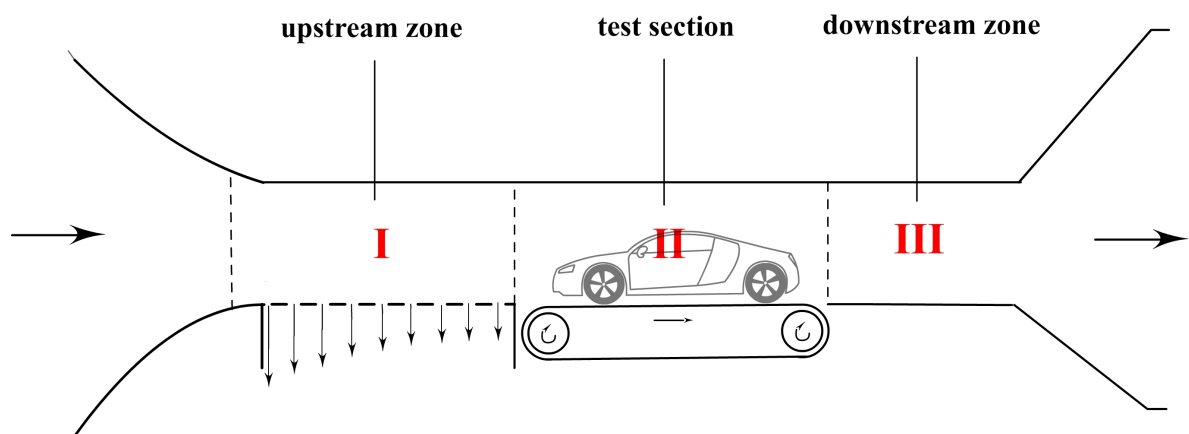
Figure 3.17: gradient flow speed boundary layer suction

Part II

The research

Chapter 4

System description

In the first part of this report the context of boundary layer suction systems in wind tunnels is explained. A description of a system that can be adapted to generate different suction distributions is presented in this chapter. A test section of the system is build for the research on the adaptive system. This test setup is also described in this chapter.

4.1 proposed system

The proposed system consists of a suction duct. The upper side of the duct consists of a porous material. At the end of the duct a hose with a pump can be attached. When the pump is activated it generates an underpressure in the channel, and airflows through the porous material. The rigid bottom plate of the duct can be adjusted in height and in angle in order to locally change the cross section area of the suction channel. This will adjust the pressure gradient in longitudinal direction in the duct and thus the airflow velocity through the porous material. The system is illustrated in figure 4.1. When the system is implemented
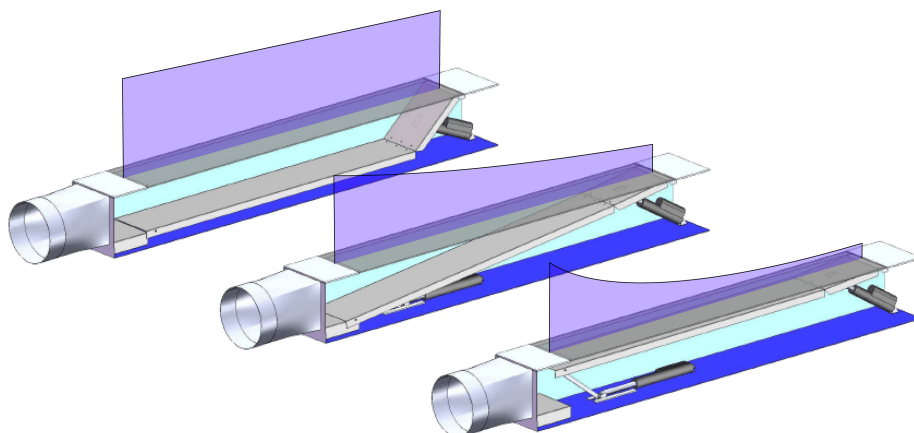
Figure 4.1: examples of the suction distribution

into a wind tunnel, with the porous upper side leveled with the wind tunnel ground plane, it can be used as a adaptive boundary layer suction system.

4.2   test setup

For this research a test channel is built. Besides this test duct the complete test setup consists of a sensor system, and actuating system. The test setup is illustrated in figure 4.2.
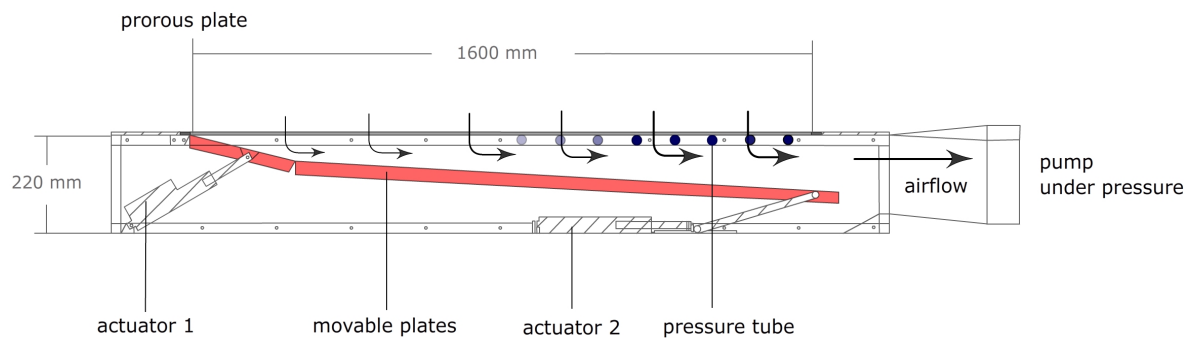
Figure 4.2: test setup

4.2.1   sensor system

The sensor system measures the underpressure at 16 places under the porous material. It uses a Scanivalve digital sensor array, software is written to read out this sensor array at 10 Hz with an accuracy of 0.2 % in a range from 0 to 2500 Pa.

4.2.2   actuator system

The two actuators used are linear actuators that can be speed controlled in two directions. Inside the actuators a variable resistor produces a variable voltage signal proportional to the position or stroke length of the actuator.

4.2.3 duct composition

An exploded view of the construction of the duct is given in figure 4.3.

porous upper side

movable plates

hose connection

actuator 1

actuator 2

under side
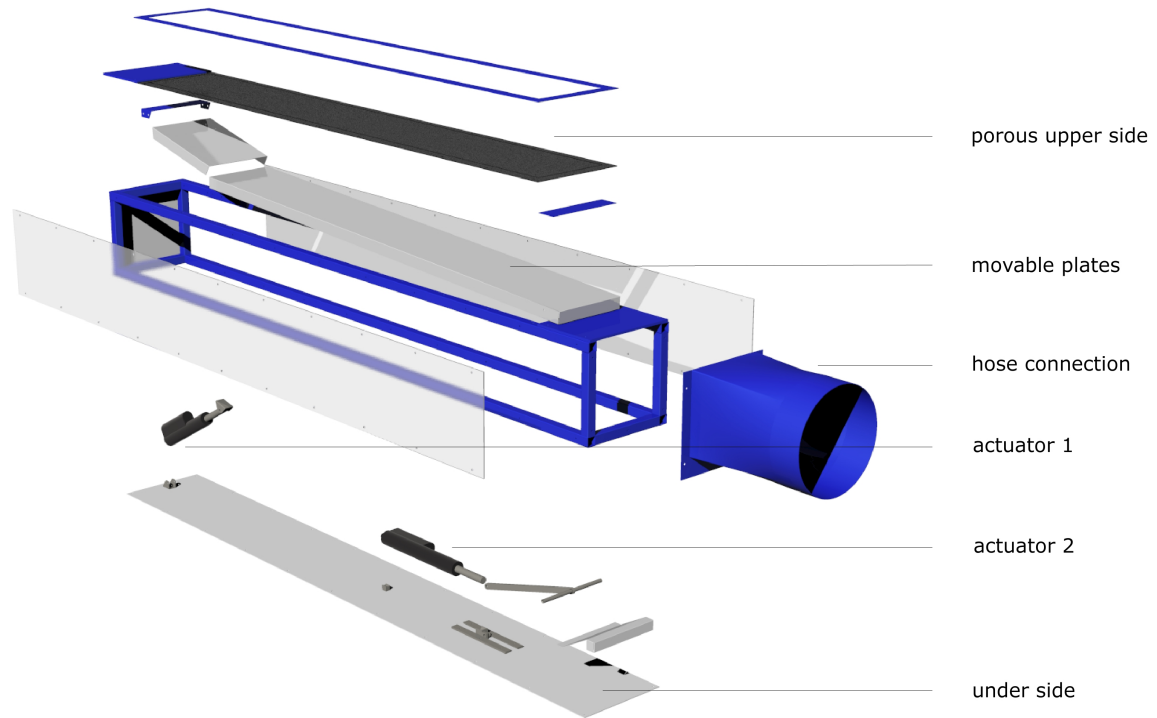
Figure 4.3: exploded view of the construction of the duct

The sides of the duct are made of transparent plastic, so the positions of the plates can also be visually checked. The upper side of the duct is made of a porous plastic. The two actuators can change the positions of the movable plates, changing the geometry of the duct.

In the following chapters a model for this suction system is implemented and verified with the test setup described above.
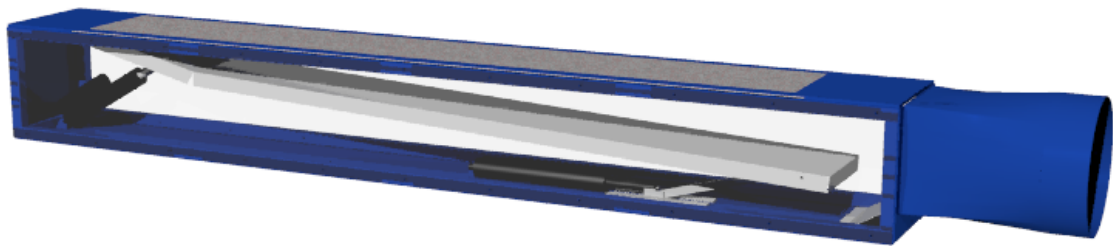
Geometry model

Figure 5.1: render of the actual suction duct

To be able to control the movable plates in the test section, a model of the geometry of the suction duct is made. This model has the actuator strokes or lengths as inputs and the positions of the two movable plates, and thereby the geometry of the duct as output. The duct geometry is defined as shown in figure 5.2. It is defined as the space between the movable plates and the porous upper side of the test section. The duct geometry is an input for the airflow model described in the next chapter.
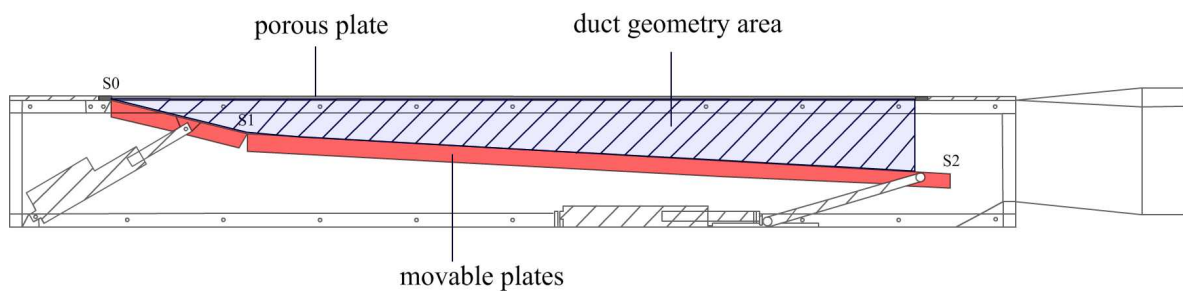
Figure 5.2: the duct geometry

5.1   constructing the geometry model

A closer look on the geometry of the test section is shown in figure 5.3. Here point $S0$ and point $S1$ are the positions of the begin and end of movable plate 1. $S1$ and $S2$ are the begin and end positions of plate 2. These points define the current geometry of the duct, and the volume in the duct through which the air will flow.
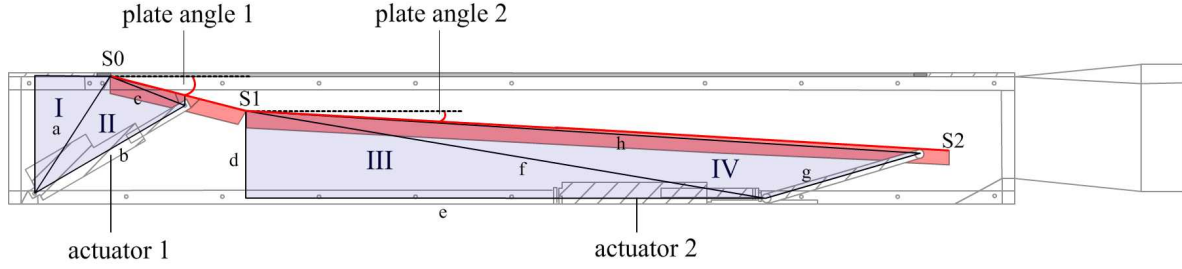
Figure 5.3: a closer look on the geometry of the test section

With known actuator strokes the positions of the plates ($S1$ and $S2$) can be calculated. $S0$ is fixed, so has always the same position $(0, 0)$. $S1$ is influenced solely by actuator 1, while point $S2$ depends on the position of $S1$ and the stroke of actuator 2. In the geometry model, with known length of actuator 1, and help of the triangles I and II, the angle of plate 1, α is calculated. The angle of plate 1 together with the length of plate 1, defines the (x, y) position of $S1$ as in 5.1 and 5.2.

Knowing the (x, y) position of $S1$, the angle of movable plate 2, β, can be calculated in an analogue way with help of triangles III and IV. Again from this angle and the length of the second plate, the (x, y) position of $S2$ can be calculated as in 5.3 and 5.4.

$$S1x = cos\alpha \cdot L_{plate1} \tag{5.1}$$

$$S1y = sin\alpha \cdot L_{plate1} \tag{5.2}$$

$$S2x = S1x + cos\beta \cdot L_{plate2} \tag{5.3}$$

$$S2y = S1y + sin\beta \cdot L_{plate2} \tag{5.4}$$

5.2   simulation of the geometry model

From calculations on all possible actuator strokes, it can be seen that not all pair of actuator settings produce plate positions which are inside the duct geometry. Those actuator pair values are noted as unsafe because they can damage the duct by pushing the movable plates against the upper side and the bottom of the duct. The vertical position of the end of the second plate (point S2) is always the closest to the duct upper side and bottom and can therefore be used as a reference point to determine the safe domain of the actuators. Figure 5.4 shows an example of S2 being out of its safe domain.
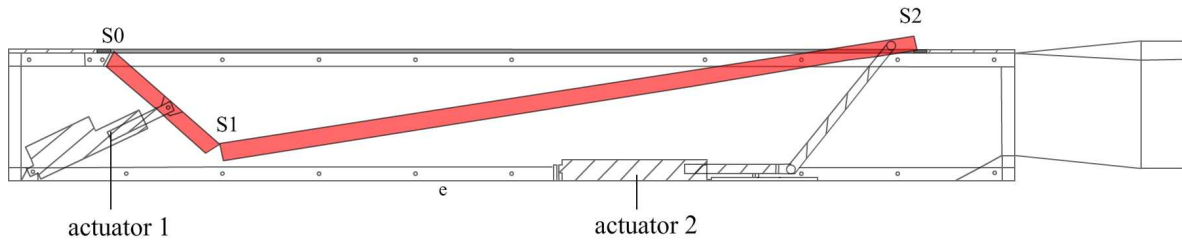
Figure 5.4: unsafe geometry

To determine the range of safe actuator positions the y positions of S2 are simulated on the whole actuator stroke domains. The stroke domain of actuator 1 is 0 to 115 mm and of actuator 2 is o to 170 mm. The vertical (y) positions of the plates have to stay within the height of the duct, meaning within 0 and 220 mm.

A 3d plot of these calculations can be seen in figure 5.5. A contour plot of this graph can be seen in figure 5.6, here the darker area is the safe area. From this plots can be seen that the strokes of both the actuators need to be considered to determine the allowed plate positions. This information is used later on to control the plate in a safe way without destructing the test section.
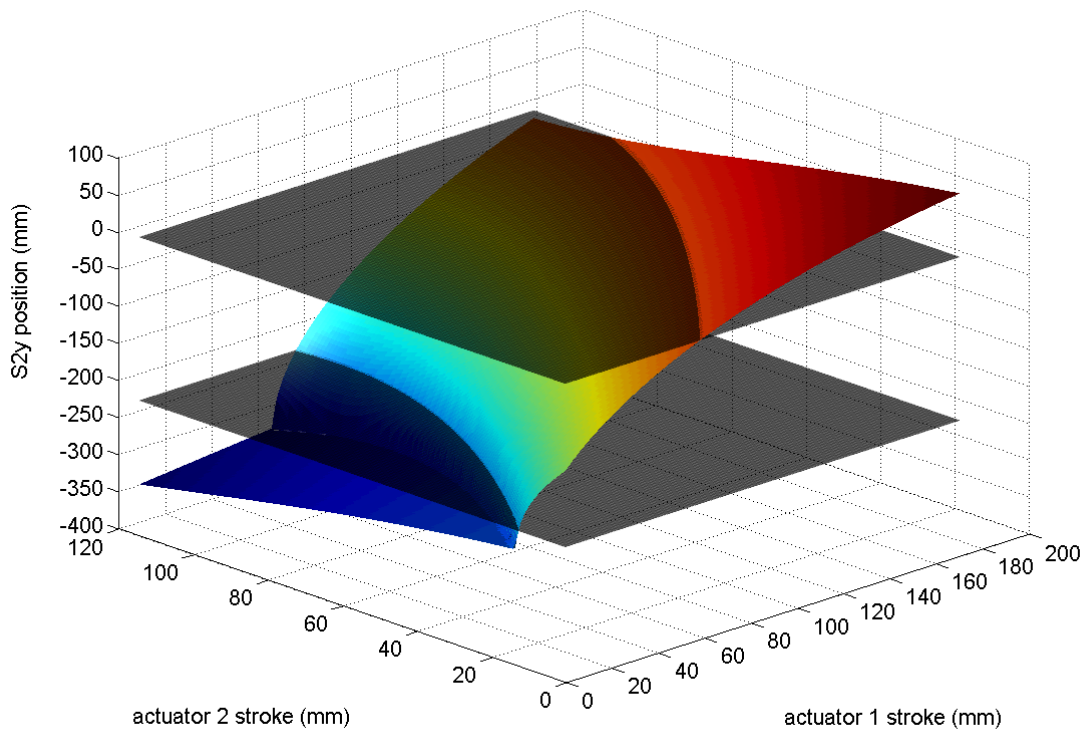
Figure 5.5: graph of critical plate positions at different actuator strokes
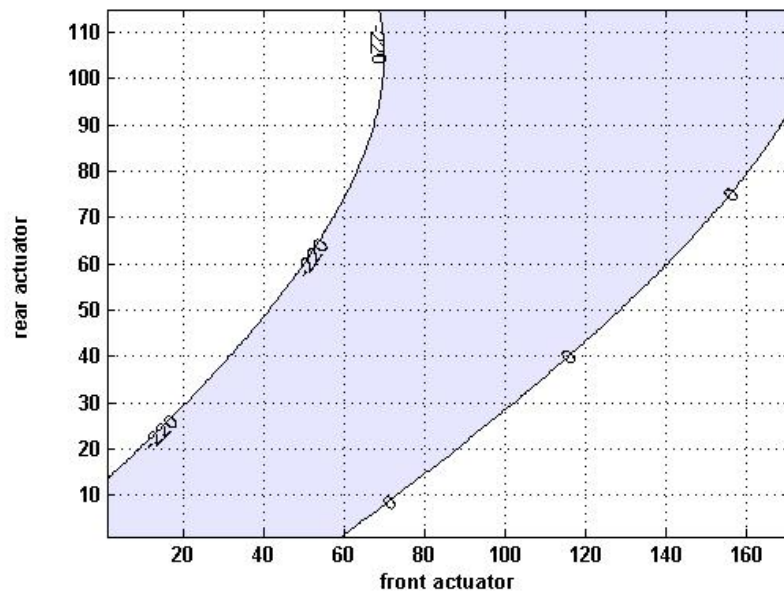
Figure 5.6: contour plot of the critical plate positions (0 to 220 mm) at different actuator strokes

5.3   implementing the geometry model

Besides the safe positions of the two movable plates, with known actuator strokes, all duct geometries can be calculated. To determine the current actuator strokes a potential meter inside the actuators is used as a position feedback. A voltage signal produced by these variable resistors is proportional to the actuator stroke. This signal is read out and the stroke is determined. A real time visualization of the geometry of the duct is made to visually compare the positions of the plates in the model to the real plate positions, at all time. A visualization is shown in figure 5.7. This visualization is used to quick check the plate positions while doing measurements on the duct.
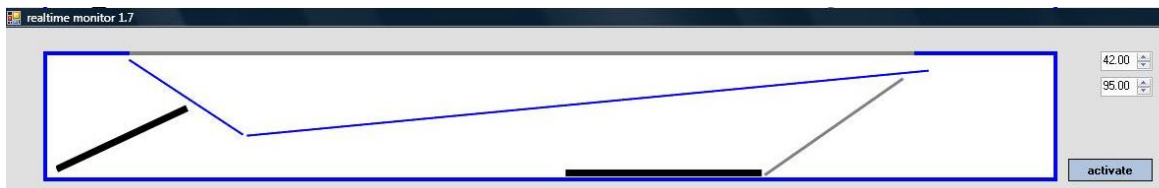
Figure 5.7: real time visualization of the current duct geometry
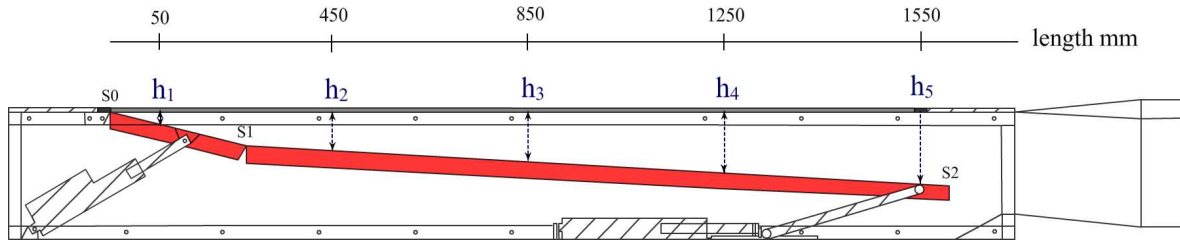
Figure 5.8: measurement positions in duct geometry

5.4 correctness and accuracy of the geometry model

5.4.1 measurements

The accuracy of the geometry model is determined by manual measurements on different plate positions with a caliper rule (dutch: schuifmaat). The measurements are done on different locations in the length (x) direction of the duct as shown in figure 5.8. This is repeated for different actuator settings, and thus for different duct geometries. The plate position data from the model on these locations are used to determine the deviation from the real positions.

5.4.2 results

mean absolute error	0.9	mm
mean relative error	1.56	%
arithmetic mean error	-0.55	mm

Table 5.1: geometry model accuracy

Table 5.1 gives a summary of the measurements on the geometry. An absolute error mean is used to quantify the errors , the arithmetic mean of the error is used to check if the error is on average positive or negative.

From the table can be seen that the mean error is +/- 0.9 mm. Also a normalization of the error to the average duct height is given. From the arithmetic mean can be seen that the heights of the duct in the model are on average 0.55 mm to low. The errors occur random as can be seen in the error distributions of figure 5.9.

5.4.3 error causes

The errors in the geometry model are mainly caused by the play of the mechanical components and flexing of the two plates. They are also caused by the actuator read out non-linearity and drift but these values are much lower (within 0.1 mm).
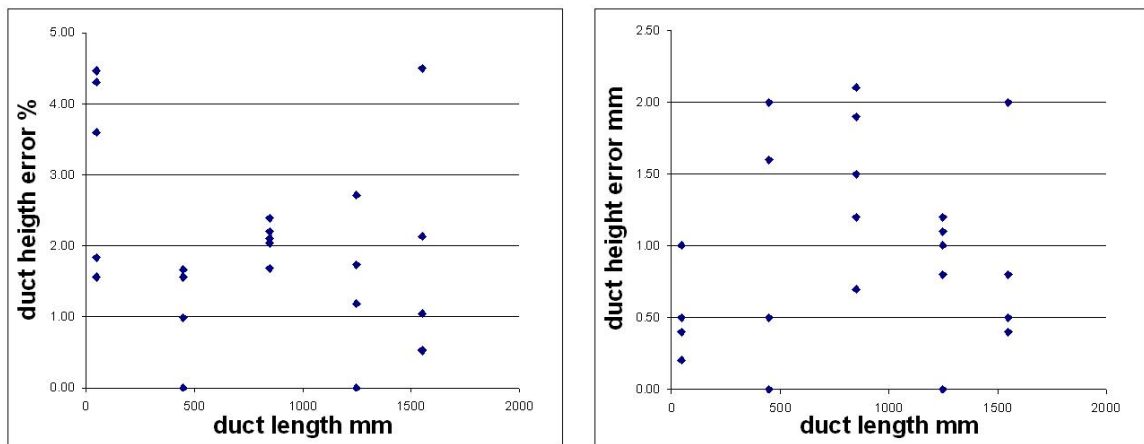
Figure 5.9: error distributions of the geometry measurements

Chapter 6

Airflow model

To get insight into the behaviour of the air flowing through the porous surface and in the duct another model is made. This model has two inputs, the geometry of the duct and the pressure generated by the pump. The outputs of this model are the flow speed of air through the porous surface, the flow speed of air in the duct, and the pressures under the porous surface as shown in figure 6.1. In this model the different system parameters are referenced as in table 6.1.
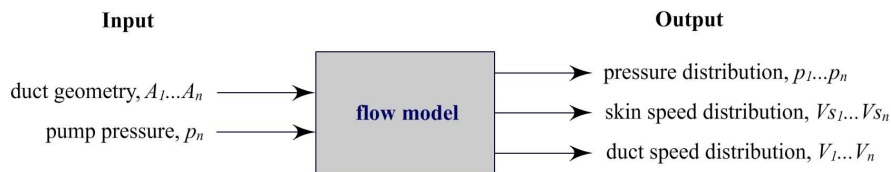
Figure 6.1: inputs and outputs of the flow model

The aim of this research is to study control techniques of the suction distribution and therefore the pressure distribution along the length of the duct. Therefore the model must be able to produce the values of these parameters at different locations in the duct. The test section itself, which will be used to check the models, is able to measure the pressure at 16 different locations in x direction (the length of the duct). The model should at least be able to produce accurate pressure values at these 16 places in the duct.

description	parameter	units
area of the porous surface	As	m^2
area of the duct cross section	A	m^2
pressure in the duct	p	Pa
airspeed in the duct	V	m/s
airspeed through the porous surface	Vs	m/s

Table 6.1: flow model unit table

6.1   modeling method

To study fluid motion in basic two methods are used:
(1) seeking to describe the detailed flow pattern at every point (x, y, z) in the field, or
(2) working with a finite region, making a balance of flow in versus flow out, and determining gross flow effects such as the force or torque on body.[14]

In this research little interest is in knowing the detailed flow pattern at every point of the flow. The flow parameters at different regions in the duct geometry are of interest. Therefore the second method or 'control volume method' is used. This method uses fixed volumes through which the airflows. Each of these volumes has its own system boundaries with air flowing in and air flowing out of the volume. All the pressure forces work on these region boundaries. In this research the fixed regions are constructed by dividing the duct geometry in discrete cells. This is shown in figure 6.2.
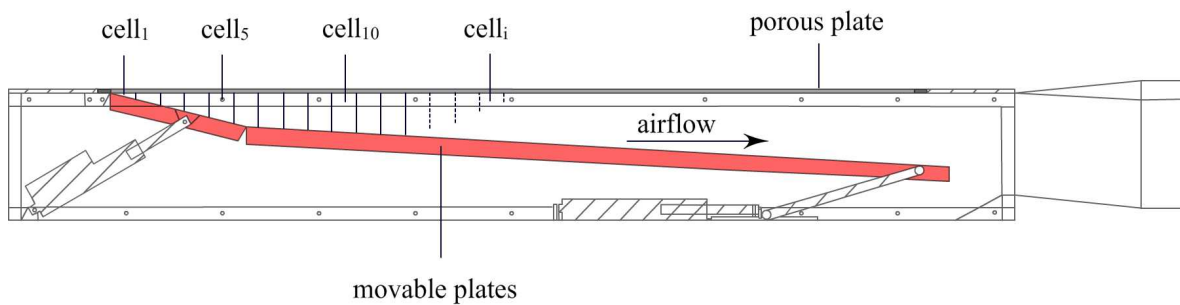
Figure 6.2: the duct geometry divided into discrete cells

Basic laws of physics are to some extent applicable on these discrete cells, such as mass conservation and Newton's force laws. In addition a relation exists between the pressure in the cell and the air flowing through the porous surface of the cell. In the next sections the equations of the above relations are derived. They form the basis for the airflow model. In this airflow model the underpressures,p_i, in the duct are defined as positive underpressures or pressure differences. In this way loss of pressure in the duct, will represent a decrease in underpressure. Furthermore in the model the following assumptions are made:

1. the system is in steady state

2. the velocity of the flow through a cell surface is constant

3. the flow is incompressible, with a constant density ρ

4. the air surrounding the duct is constant

6.2   a discrete model of the duct

An abstraction of the cell division is given in figure 6.3. The pressures p in the duct, are specified on all cell boundaries. The airflow speeds V in the duct are defined in one direction

on the cell boundaries. The speed of the airflow through the porous upper side of the cell Vs is specified in the same direction as the airflow speed in the cell. At first the equations for a duct with equal cell heights, and rectangular cells, are derived. Later on, an addition for different cell geometries is done.
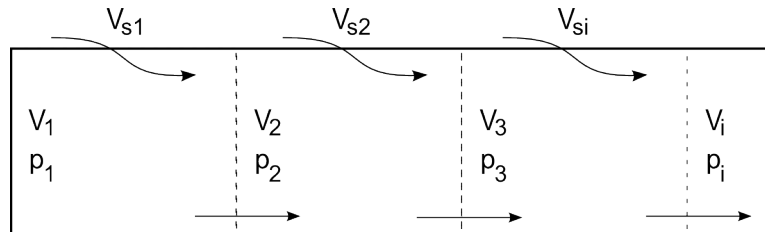
Figure 6.3: flow model

6.3 deriving the equations

6.3.1 conservation of mass

Contrary to a mechanical system with forces working on fixed masses, when dealing with control volumes and flows the mass conservation is of great interest. In equilibrium the mass of the air flowing out of the volume has to be equal to the mass of the air flowing into the volume. This is illustrated in figure 6.4.
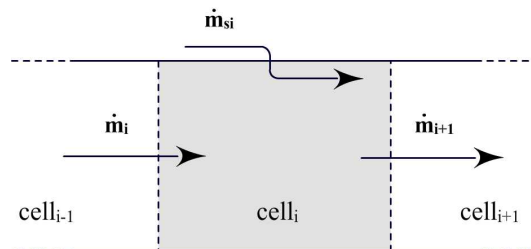
Figure 6.4: mass balance for an individual cell

The mass flow is denoted as $\dot{m}$ in kg/s. In the case of the different cells in the duct, the airflows in from a neighbour cell and from its own porous upper side. It flows out to the other neighbour cell. This is described by equation 6.1 with $\dot{m}_{i+1}$, being the mass flow out of the cell, $\dot{m}_i$, the mass flow into the cell from inside the duct, and $\dot{m}_{si}$, the mass flow through the porous surface.

$$\dot{m}_{i+1} = \dot{m}_i + \dot{m}_{si} \tag{6.1}$$

Because of the relative low expected velocity of the flow, the flow is expected to behave as an incompressible flow, with constant density. With constant flow density, the mass flow $\dot{m}$

equals $\rho \cdot A \cdot V$ and equation 6.1 becomes:

$$\rho A_{i+1}V_{i+1} = \rho A_i V_i + \rho A_{si}V_{si} \tag{6.2}$$

With the density constant, ρ is divided out of the equation:

$$A_{i+1}V_{i+1} = A_i V_i + A_{si}V_{si} \tag{6.3}$$

Equation 6.3 will be used in the model later on.

6.3.2 a momentum balance

Besides the balance of the masses, a momentum balance exists in equilibrium. To derive this momentum balance all different forces working on the control volume have to be explored. In basic three different forces work on the cells:
1. the momentum flux of the airflow, F_m
2. pressure forces, F_p
3. friction forces, F_d

The net sum of each particular force is the sum of its components. In equilibrium the net force of these different forces has to be equal to the momentum flux of the airflow as in equation 6.4.

$$\sum F_p + \sum F_d = \sum F_m \tag{6.4}$$

In the next sections equations for these different net forces are derived. Then these force equations are substituted in equation 6.4 to obtain the momentum balance equation.

momentum flux

The net force on a fixed control volume equals the rate of change of momentum within the control volume plus the vector sum of outlet momentum fluxes minus the sum of inlet fluxes as in equation 6.5[14].

$$\sum F_m = \frac{d}{dt}(\int V \rho dV) + \sum (\dot{m}_i V_i)_{out} - \sum (\dot{m}_i V_i)_{in} \tag{6.5}$$

Again with $\dot{m}$ being the mass flow, in kg/s. Equation 6.5 is an application of Reynold's transport theorem and Newton's second law, $F = ma = \frac{d}{dt}(mV)$ [14]. The equation should be used with care however, the term $\sum F_m$ is a vector sum of all forces working on the control volume.
In equilibrium, the rate of change of momentum within the control volume is zero, and 6.5 becomes equation 6.6.

$$\sum F_m = \sum (\dot{m}_i V_i)_{out} - \sum (\dot{m}_i V_i)_{in} \tag{6.6}$$

With two inlets and one outlet, the momentum flux terms are illustrated in figure 6.5.
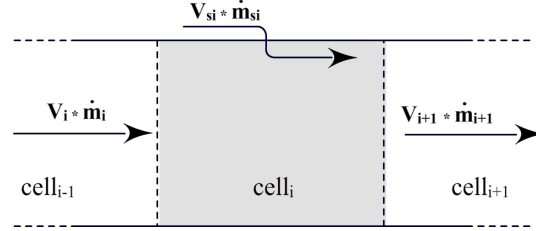
Figure 6.5: momentum flux terms in an individual cell

The terms in figure 6.5 can be expressed in the model parameters as in equations 6.7.

$$\sum F_m \;=\; \dot{m}_{i+1}V_{i+1} - \dot{m}_{si}V_{si} - \dot{m}_i V_i \tag{6.7}$$
$$=\; \rho A_{i+1}V_{i+1}V_{i+1} - \rho A_{si}V_{si}V_{si} - \rho A_i V_i V_i \tag{6.8}$$
$$=\; \rho A_{i+1}V_{i+1}^2 - \rho A_{si}V_{si}^2 - \rho A_i V_i^2 \tag{6.9}$$

Equation 6.9 will be used as approximation for the net momentum flux in the model.
In the next section the forces driving the air to flow in the duct, the pressure forces, are explored.

pressure forces

The net forces working on the control volume by the pressures on the boundaries of the cell, for a rectangular cell are shown in figure 6.6.
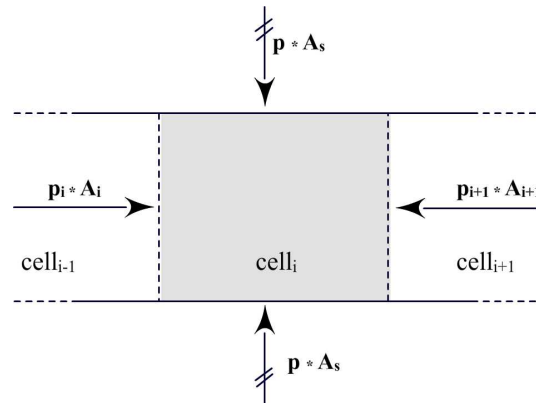
Figure 6.6: pressure forces working on an individual cell

The pressure surrounding the complete duct is uniform (atmospheric). All pressures inside the duct are pressure deviations from this uniform pressure. Again the net pressure force is

the sum of all the pressure forces working on all boundaries of the control volume. However the upper side and underside of the cells have equal pressures and equal surface areas on which this pressures work. These vertical pressure forces are the same and work in opposite directions. Therefore the net pressure force on the cell is only influenced by the horizontal pressure forces working on the left and right side of the cell:

$$\sum F_p = p_{i+1}A_{i+1} - p_i A_i \tag{6.10}$$

For a rectangular cell this pressure model is correct, however the movable plates can generate geometries in which the cell are not rectangular but have a geometry as shown in figure 6.7.
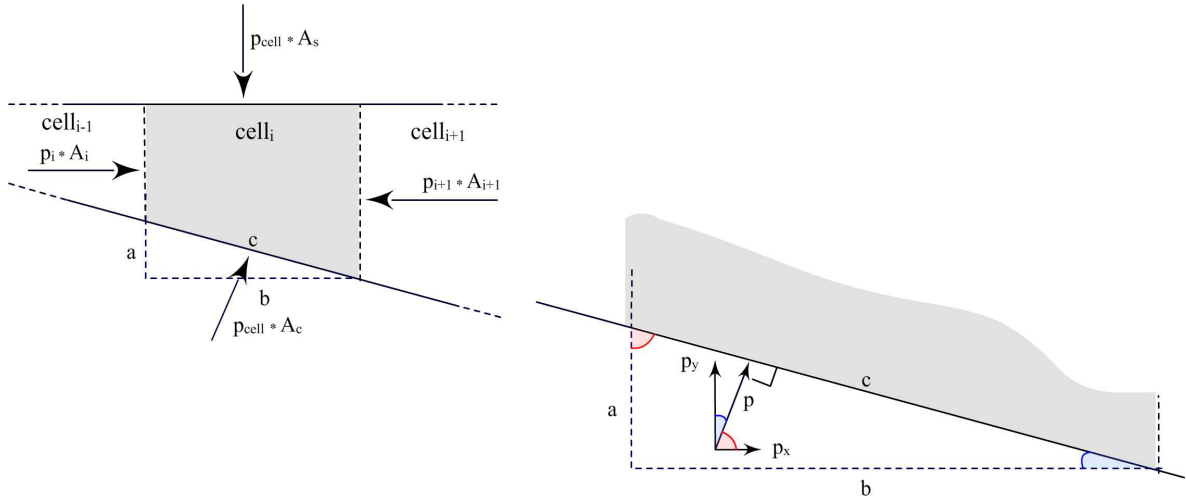
Figure 6.7: pressure forces working on an individual non rectangular cell

In this case the pressure at the underside of the cell works in another direction as in the rectangular case. The direction of the pressure force working on the sloped underside of the cell can be divided into an horizontal component, p_x and a vertical component p_y. The force of the pressures vertical component is the same in size and opposite in direction as the pressure force working on the upper boundary of the cell, therefore the vertical component can be left out of the equation for the net pressure on the cell.[1]

The x component of the force working on the underside of the cell however is influencing the net pressure force in horizontal direction. This force is equal to $p_x \cdot c$. Being the pressure component , p_x, times the area of the sloped underside of the cell, c in figure 6.7. This force component, $p_x \cdot c$, has to be expressed in the model parameters. By angle equivalence for corners $(\angle p, p_x)$ and $(\angle a, c)$ equation 6.11 holds:

$$cos(\angle p_x, p) = \frac{p_x}{p} = cos(\angle a, c) = \frac{a}{c} \tag{6.11}$$

So the force component in x direction, $p_x \cdot c$, can be expressed by, $p_{cell} \cdot a$. This is the pressure inside the cell, times the difference in height between the left and right side of the cell. This

---

[1] By angle equivalence for corners $(\angle p, p_y)$ and $(\angle b, c)$: $cos(\angle p_y, p) = \frac{p_y}{p} = cos(\angle b, c) = \frac{b}{c}$ and so $p_y \cdot c = p \cdot b$, which is the same as the force on the upper side of the cell.

factor is easier to express in the model parameters because $a = A_{i+1} - A_i$. For the pressure in the cell, p_{cell}, the linear average, between p_i and p_{i+1} is used. In reality this pressure distribution will not at all times be linear, but when a sufficient amount of cells is used it will be a good approximation.

So with $a = A_{i+1} - A_i$ and $p_{cell} = \frac{p_{i+1} - p_i}{2}$ the pressure force working in x direction on the sloped underside can be expressed in the model parameters:

$$
\begin{aligned}
F_{px-underside} &= p_x \cdot A_c & (6.12) \\
&= p_{cell} \cdot (A_{i+1} - A_i) & (6.13) \\
&= \frac{p_{i+1} - p_i}{2} \cdot (A_{i+1} - A_i) & (6.14)
\end{aligned}
$$

With equation 6.14 added to equation 6.10, the net pressure force on the cell or control volume is now defined as in 6.15.

$$
\sum F_p = p_{i+1} A_{i+1} - p_i A_i - \frac{p_{i+1} - p_i}{2} \cdot (A_{i+1} - A_i) \qquad (6.15)
$$

This equation also holds for the rectangular cell case with the $A_{i+1} - A_i$ component being zero.

Equation 6.15 is used in the model, again with the note that the $\frac{p_{i+1} - p_i}{2}$ is a linear average. A sufficient number of cells has to be used to overcome the error caused by this approximation.

friction forces

Besides the pressure and momentum forces, also friction forces from the duct walls work on the airflow in the duct. These friction forces are influenced by roughness of the material of the walls and the flow characteristics (referenced by its Reynolds number). The volume of air flowing in a particular way over the surfaces, over a particular distance, determines the amount of friction in the duct. This friction causes an additional pressure loss. To estimate these pressure losses, multiple mostly empirical models are available. However, most of these models deal with fully developed flows in closed ducts, in which the flow speed distributions have a predefined shape. In our case however the flow speed distribution is constantly changing because air is added from the upper side of the duct. To get a basic idea of the flow speed distribution a CFD (computational fluid dynamics) simulation of a duct with a porous surface is shown in figure 6.8.
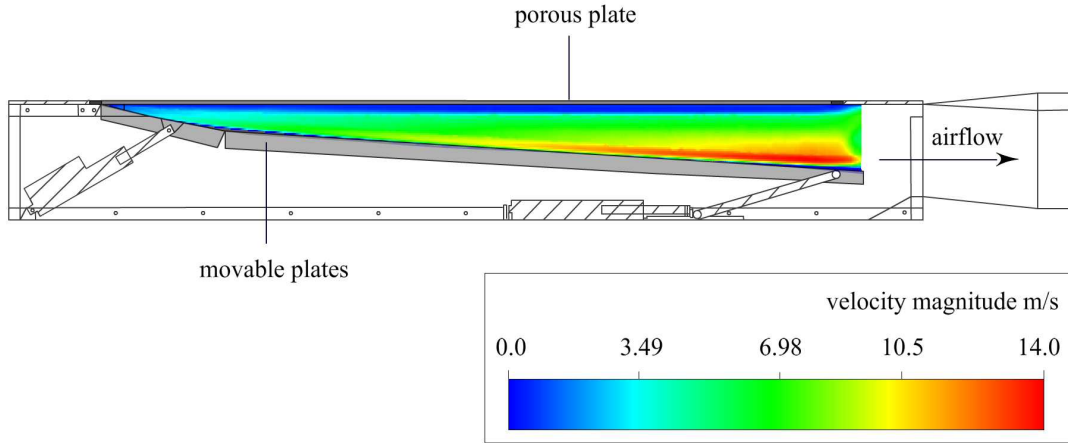
Figure 6.8: cfd simulation of velocity distribution in the duct

The flow speed distribution in the duct with porous surface is, according to this CFD simulation, very different from the fully developed flows in closed or non porous ducts. Therefore it is not sound to use the available models to determine the friction losses in the porous duct. In the model we can only assume that the friction forces are very low at the relative low velocity of air in the duct. In this model this assumption is made however, and the airflow is modeled with zero friction force.

equilibrium equations

From the momentum equation 6.7 and pressure force equation 6.15, with zero friction, equation 6.16 is derived for the momentum flux balance in a cell in equilibrium.

$$p_{i+1}A_{i+1} - p_iA_i - \frac{p_{i+1} - p_i}{2} \cdot (A_{i+1} - A_i) = \rho A_{i+1}V_{i+1}^2 - \rho A_{si}V_{si}^2 - \rho A_iV_i^2 \qquad (6.16)$$

Equation 6.16 will be used in the flow model later on.

6.3.3 speed and pressures over the porous skin

The last physical property of the air flowing in the duct, is the speed of air flowing into the duct through its porous upper side. This speed is proportional to the pressure difference over the porous skin. It is defined by the manufacturer of the porous material but with a rather low accuracy (speed +/- 10 %). For this model however the relation between the pressure over the porous skin and the speed of air through the skin is of high importance. So for this research the manufacturer's specification is inaccurate. To overcome this measurements on the porous skin are done and an accurate emperical model of the speed/pressure relation of the porous material is made. This model is defined as shown in equation 6.17.

$$\Delta p = R_1 V_{si}^2 + R_2 V_{si} \tag{6.17}$$

In the model Δp is defined as the average cell pressure being approximated by $(p_i + p_{i+1})/2$. Again with a sufficient number of cells this approximation is accurate. In the model parameters equation 6.17 becomes:

$$(p_i + p_{i+1})/2 = R_1 V_{si}^2 + R_2 V_{si} \tag{6.18}$$

The coefficients $R1$ and $R2$ are different for different porous materials. For the porous material on the test section these values are 543 and 343 for $R1$ and $R2$ resp. In this model however these constant values can be used as input parameters so the model can be used for different porous materials.

6.3.4 equation summary

In the previous section the following equations of the physical processes in the suction duct, in equilibrium, are derived:

mass balance:

$$A_{i+1}V_{i+1} = A_iV_i + A_{si}V_{si} \tag{6.19}$$

force balance:

$$p_{i+1}A_{i+1} - p_iA_i - \frac{p_{i+1} - p_i}{2} \cdot (A_{i+1} - A_i) = \rho A_{i+1}V_{i+1}^2 - \rho A_{si}V_{si}^2 - \rho A_iV_i^2 \tag{6.20}$$

skin airflow speed:

$$(p_i + p_{i+1})/2 = R_1V_{si}^2 + R_2V_{si} \tag{6.21}$$

These are the equations used in the model. In the next section a method to solve these equations for different inputs will be developed.

6.4 solving the equations

6.4.1 proof of solvability

First it is proved that the set of derived equations is solvable with the given input parameters of the model. To be a solvable set the number of unique equations has to be equal to the number of unknown parameters. The input parameters are defined by the pump pressure being the pressure at the last cell n, p_n and the geometry of the cells, $(A_1...A_n)$. Furthermore in the test section the duct is closed at cell 1 and therefore, the speed of the air, V_1 will be zero at the first cell.

To prove the solvability of the set first it is proved that the set of equations of 3 cells is solvable. Later on this proof is extended for the general case. For the 3 cell case the set of equations is given by:

mass balance:

$$
\begin{align}
A_2V_2 &= A_1V_1 + A_{s1}V_{s1} \tag{6.22}\\
A_3V_3 &= A_2V_2 + A_{s2}V_{s2} \tag{6.23}\\
A_4V_4 &= A_3V_3 + A_{s3}V_{s3} \tag{6.24}
\end{align}
$$

force balance:

$$p_2A_2 - p_1A_1 - \frac{p_2 - p_1}{2} \cdot (A_2 - A_1) = \rho A_2V_2^2 - \rho A_{s1}V_{s1}^2 - \rho A_1V_1^2 \tag{6.25}$$

$$p_3A_3 - p_2A_2 - \frac{p_3 - p_2}{2} \cdot (A_3 - A_2) = \rho A_3V_3^2 - \rho A_{s2}V_{s2}^2 - \rho A_2V_2^2 \tag{6.26}$$

$$p_4A_4 - p_3A_3 - \frac{p_4 - p_3}{2} \cdot (A_4 - A_3) = \rho A_4V_4^2 - \rho A_{s3}V_{s3}^2 - \rho A_3V_3^2 \tag{6.27}$$

skin pressure loss:

$$(p_2 + p_1)/2 = R_1 V_{s1}^2 + R_2 V_{s1} \tag{6.28}$$
$$(p_3 + p_2)/2 = R_1 V_{s2}^2 + R_2 V_{s2} \tag{6.29}$$
$$(p_4 + p_3)/2 = R_1 V_{s3}^2 + R_2 V_{s3} \tag{6.30}$$

boundary conditions:

$$V_1 = 0 \tag{6.31}$$
$$p_4 = pump_p ressure \tag{6.32}$$

The number of equations is 11 (with the boundary conditions), and equals the number of unknown variables, therefore this set of equations for 3 cells is solvable.

By adding a cell, 3 equations are added to the set, as well as three unknown parameters, p_i, V_i and V_{si}. The number of equations will stay equivalent to the number of variables.

In general the number of equations, $NOE = 3 \cdot n$ and the number of unknown variables, $NOV = 3 \cdot n + 2$. So generally for n cell holds that $NOE - NOV = 2$. With n the number of cells. By the 2 boundary conditions the number of equations will always become equivalent to the number of variables. So the set is proved to be generally solvable for any number of cells.

6.4.2   implementing the model

Because of the quadratic terms in the force balance and the cross terms of almost all parameters, the derived set of equations is far from linear. So solving methods for linear sets of equations are not applicable. To solve this set of non-linear equations the model is implemented in the program environment of Matlab, and solved by the optimization toolbox of Matlab. Matlab solves these sets of equations iteratively. It starts with a guess and tries to iterate to a solution of the problem.

To avoid programming errors and to remain transparency, the implemented Matlab model, has to be recognizable as the physical model derived before. Therefore the implemented model uses the already available and tested Matlab solvers as much as possible.

First a Matlab model was made to solve sets of a predefined number of cells, and thus with a predefined number of equations. Later on a model was developed to generate sets of equations for the general case with different number of cells. In this step all the variables were vectorized. By this vectorization a certain amount of transparency was lost, on the other hand it made the program more powerful. However the physical equations can still be recognized in the code. The Matlab solver and optimizers can only solve to one vector of unknown parameters. For usability the tool is expanded with a wrapper function, which returns not all the solved parameters in one vector, but returns three vectors with parameters of the same units.[2]

---

[2]The total Matlab model consists of 2 short functions in 2 different m files, a function generator, a function solver, and a wrapper function to return the values in an organized way, they are attached in Appendix B

6.5   data visualization

To be able to solve the equations with multiple duct geometries and pump pressures a visual
user interface is made in C++. Basically this program is an interface to the Matlab model.
In this program a geometry can be selected as well as a pump pressure. It then generates
the intersections of the wanted number of cells. All the input parameters for the model are
passed to a Matlab Runtime Environment in which the model is solved. Then the calculated,
speed and pressure values are returned by Matlab. This data is presented in the visual C++
interface in a graph, and stored in a text file.
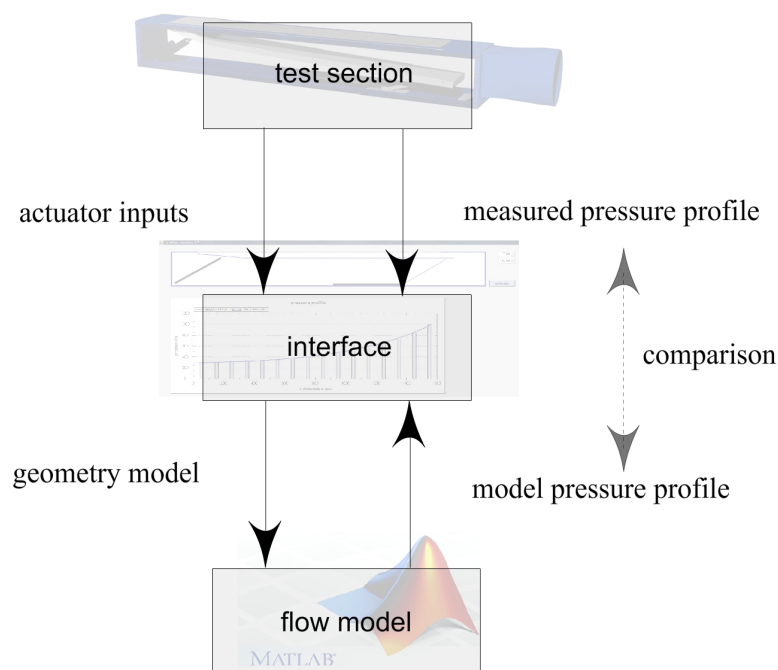
Figure 6.9: diagram of the measurement setup for the flow model

With the program coupled to the actuator outputs, also the current real time geometry model
can be generated. In this case the pressure and speed distributions can be calculated real
time at 1Hz.[3] This is illustrated by figure 6.9.

6.6   correctness and accuracy of the airflow model

To verify the airflow model, measurements are done on the test setup, the results of this
measurements are presented in this section.

---

[3]The Matlab runtime environment uses about 1 second to solve the model with 62 cells

6.6.1 measurements

With the test setup, the calculated pressures from the flow model are compared to measured pressures at the 16 locations in the test section. This is done for multiple duct geometries and multiple pump speeds. The measured duct pressures are visualized in a program and plotted together with the calculated pump pressures in one graph. This is shown in figure 6.10. All graphs of the measurements done are in Appendix A.
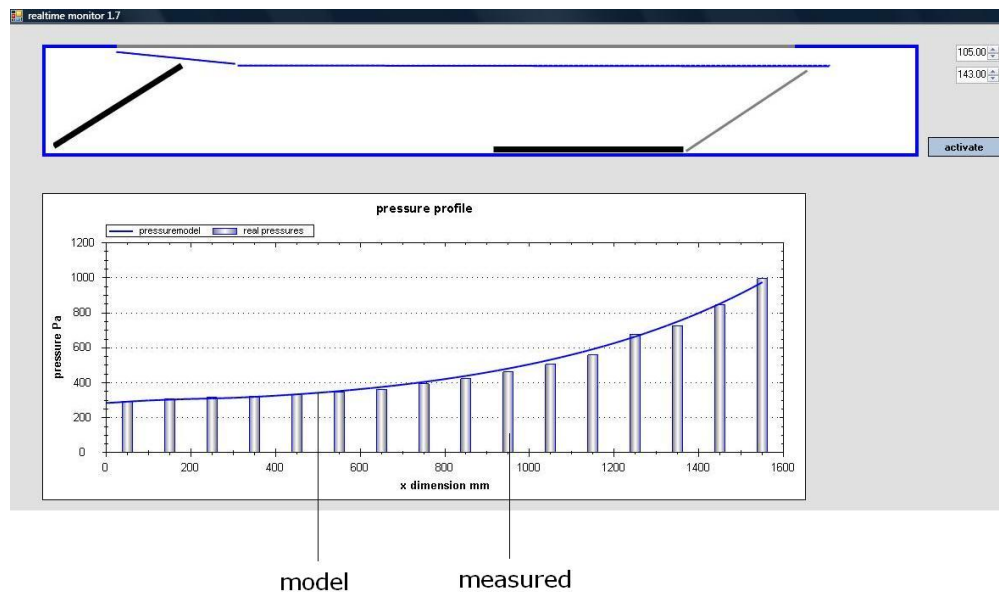
Figure 6.10: screen shot of the measurement program

A general root mean square error over the 16 positions, and an arithmetic mean error is calculated. This is done for the pressures and for the flow speed through the porous material at these 16 positions. To calculate the pressures and flow speeds at the 16 locations through the model, at least 15 cells are needed. In the model used to compare with the measurements, 62 cells are used. Expanding the number of cells in the model does not produce different outcomes.

The results in table 6.2 are the overall errors of 36 measurements [4] on 16 points in the duct. So in total 576 measured pressures were compared to the pressures produced by the model. The effect of the pressure error on the suction speed through the porous material is also given in table 6.2. These implications for the suction speeds are calculated with the empirical model from 6.3.3. From this calculations can be seen that the error on the suction speeds, Vs, is lower than the error on the pressures. Both the RMS error and the arithmetic mean error are given. The RMS (root mean square) error is calculated as in 6.33. The arithmetic mean error is calculated as in 6.34. To get the relative errors in %, these values are devided by the mean measured pressures. The RMS errors in table 6.2 give an indication for the mean

---

[4]6 different geometries were measured with 6 different pump pressures

RMS errors		pressure	units	suction speed	units
	overall	17.2	Pa	0.016	m/s
		3.66	%	2.45	%
	highest	50.4	Pa	0.032	m/s
		6.05	%	3.45	%
arithmetic mean errors		pressure	units	suction speed	units
	overall	+14.8	Pa	+0.014	m/s
		+3.02	%	+2.11	%

Table 6.2: flow model accuracy

absolute deviations from the measured values and are within 4 %. The arithmetic mean errors are lower because here the negative and positve errors cancel each other out. Therefore the arithmetic mean is not very usable to determine the absolute errors. However it can be used to see that the model produces pressure values that are on average 3 % too high.

$$RMS_{error} = \sqrt{\frac{1}{16}\sum_{i=1}^{16}(p_{i\_model} - p_{i\_measured})^2} \qquad (6.33)$$

$$Amean_{error} = \frac{\sum_{i=1}^{16}(p_{i\_model} - p_{i\_measured})}{n} \qquad (6.34)$$

6.6.2 error causes
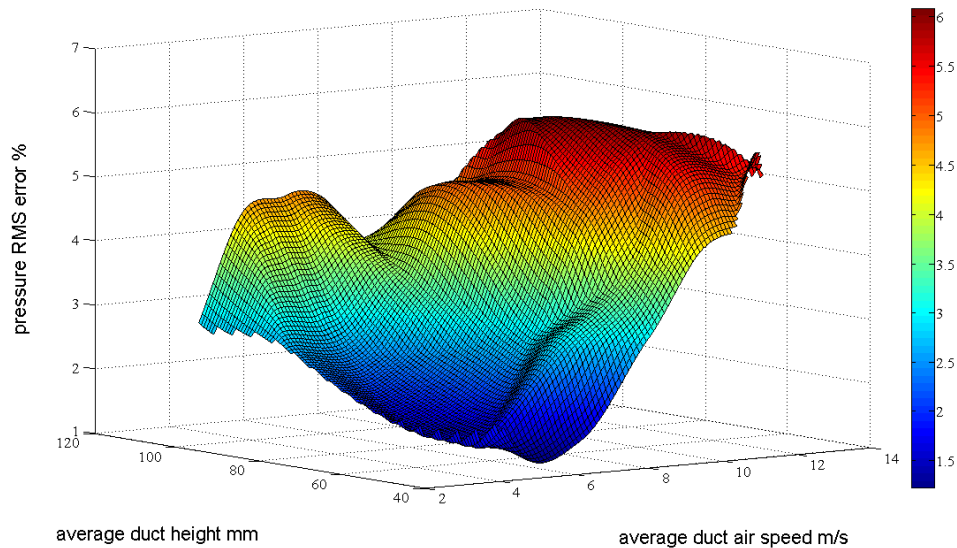
Figure 6.11: rms error distribution of all measurements

The errors generated by the flow model have different causes:

1. There exists an error in the geometry model (about 1mm in duct height), this causes an error up to 1 % on the average flow model pressure output[5].

2. The pressures in the test duct are not completely stable, they vary about 2 Pa at low underpressures to 10 Pa at high underpressures in the duct, generating an error of 0 to 1.5 % on the average duct pressure.

3. A third cause are the neglected friction forces in the duct. Figure 6.11 shows an increase in error when the air speed in the duct increases. This could be an indication for friction losses, but with the other random error causes from the geometry and air flow instability the friction losses cannot be quantified by these measurements.

4. A fourth error cause is the assumed direction of the airflow through the porous material, which is chosen in x direction. (section 6.6.3)

5. A last cause could be the discretion in cells in the model itself but test have been done with a higher number of cells, and no significant change in outcome of the model can be seen. So the discretion itself does not contribute to the errors.

---

[5]this is measured by adapting different geometry settings by 1 mm and comparison of the pressure measurements

6.6.3 model optimization

In the model of the suction duct the assumption was made that the direction of the flow through the porous material is in flow (x) direction. The momentum of the velocity of this incoming flow was therefore added to the momentum of the flow in the duct. In reality the incoming flow direction will not be the same as the direction of the flow in the duct. Although the precise direction of the incoming flow through the porous material is not known, it will be closer to perpendicular to the duct flow direction than parallel to the duct flow direction.

In the perpendicular case the momentum of the air flowing into the duct only works in y direction, because the speed is chosen in y direction. It does not contribute to the momentum of the flow inside the duct. To test and quantify this property, the model of previous sections is adapted. Therefore the momentum flux term for the incoming flow is chosen to be zero(for the perpendicular flow). In this case the force balance in equation 6.35 becomes equation 6.37. Here the speed in x direction is chosen zero, for the in flow through the porous material.

$$p_{i+1}A_{i+1} - p_i A_i - \frac{p_{i+1} - p_i}{2} \cdot (A_{i+1} - A_i) = \rho A_{i+1}V_{i+1}^2 - \rho A_{si}V_{si}^2 - \rho A_i V_i^2 \tag{6.35}$$

$$p_{i+1}A_{i+1} - p_i A_i - \frac{p_{i+1} - p_i}{2} \cdot (A_{i+1} - A_i) = \rho A_{i+1}V_{i+1}^2 - \rho A_{si}0^2 - \rho A_i V_i^2 \tag{6.36}$$

$$p_{i+1}A_{i+1} - p_i A_i - \frac{p_{i+1} - p_i}{2} \cdot (A_{i+1} - A_i) = \rho A_{i+1}V_{i+1}^2 - \rho A_i V_i^2 \tag{6.37}$$

As more force is needed to accelerate the incoming air, the pressure drop over the duct in the model will increase.
The model is implemented again in Matlab and compared against the already tested model. Pressure profiles on different geometries are calculated with both the models. An output is given in figure 6.12.

As expected the pressure drop has increased in the new model. On average the pressure at the left side of the duct is decreased by 2.01 %. To check whether the new force balance will improve the model, for all measured cases the model outputs are recalculated. The model outputs are then compared to the measured pressure values as in section 6.6.1. The accuracy of that comparison are given in table 6.3.

RMS errors		pressure	units	suction speed	units
	overall	13.8	Pa	0.013	m/s
		3.01	%	1.95	%
	highest	40.3	Pa	0.032	m/s
		4.83	%	3.18	%
arithmetic mean errors		pressure	units	suction speed	units
	overall	+10.6	Pa	+0.010	m/s
		+2.08	%	+1.41	%

Table 6.3: improved flow model accuracy
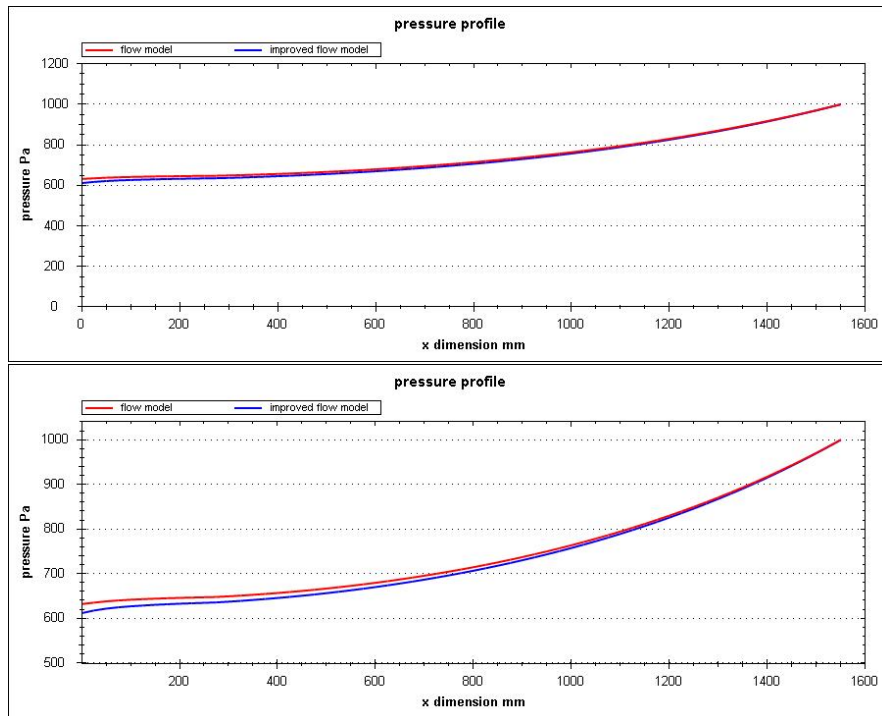
Figure 6.12: pressure output from the flow model and the improved flow model

From comparing table 6.2 to table 6.3 it can be seen that the overall error on the pressure curves of 3.66% is reduced by 0.65%, wich is a reduction of the error of 17.8%.
The error on the suction speed curves of 2.45% is reduced by 0.5%, which is an improvement on the error of 20.4%.

Chapter 7

Open loop control

One of the two controllers compared in this research is an open loop controller based on a mathematical model of the total system. The other is a closed loop control that uses a feedback optimization based on measurements. In this chapter the research on the on the open loop controller is described.

7.1 control method

The previous chapter describes a developed and tested model to calculate the flow speeds and pressures in the duct, when a geometry is given. This model is used in an adapted form to control the movable plates in the duct on a given pressure distribution, or suction speed distribution.
An open loop controller or non-feedback controller uses no feedback of the set point parameters from the real system, it only uses a model to calculate the expected system settings [8].

7.2 implementation controller

The calculations in the previous chapters were done to verify the correctness of the model with measurements. The calculated input and output data of the geometry model and flow model were as shown in figure 7.1. Here a read out voltage signal of the actuator positions eventually leads to a calculated pressure distribution.

actuator strokes, S_{A1} S_{A2} → **geometry model** → duct geometry, $A_1...A_n$ → **flow model** → pressure distribution, $p_1...p_n$
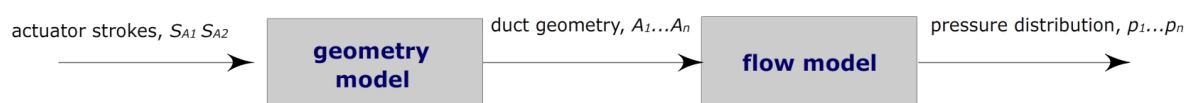
Figure 7.1: data flow used during measurements to check the the models

Now to use these verified models in a controller, the input and output of the geometry model and of the flow model need to be reversed. This is illustrated in figure 7.2. The inputs become the wanted pressure distribution and the geometry needed for pressure distribution is calculated. The next sections describes each step in this reversed calculation chain.

pressure distribution, $p_1...p_n$ duct geometry, $A_1...A_n$ actuator strokes, S_{A1} S_{A2}

flow model   **geometry model**
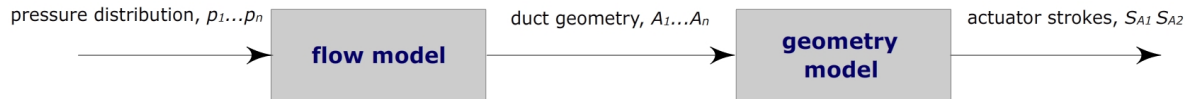
Figure 7.2: data flow used for controlling the pressure distribution

7.2.1 generating input pressure set points

First a pressure distribution along the duct needs to be given in. To generate different pressure curves, a small user interface is made. Here two parameters can be entered; one to control the pressure loss from the begin to the end of duct, and one to change the shape of the pressure curve in between. An illustration is given in figure 7.3.
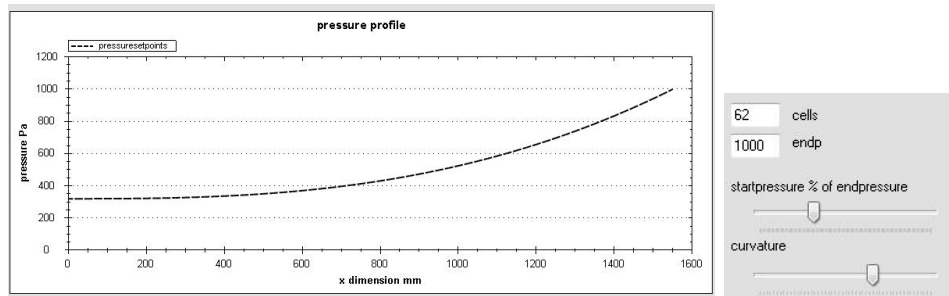
Figure 7.3: pressure distribution input interface

The start pressure is a percentage of the end pressure. The shape of the curve is generated by different polynoms set by the second input parameter. The input of pressure curves is constraint by the end pressure at the pump side of the duct. There the underpressure will be highest. Along the duct underpressure is always lost (by the porous material on the upper side), and never gained.

7.2.2 using the flow model to calculate the geometry

As said before the main input and outputs, of the flow model need to be reversed. It has to generate a geometry with a given pressure distribution in the duct. To do this the Matlab model is adapted. The known parameters are now the pressures at different discrete positions

in the duct. To the unknown parameters, the duct heights at these positions are added as in figure 7.4.
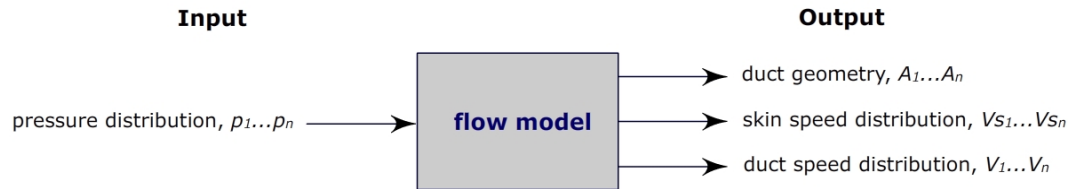
Figure 7.4: inputs and outputs of the flow model with pressure input

This does not change the number of unknown parameters in the set of equations for the discrete cells. And thus this system is also solvable by the model programmed in Matlab. It will now generate a free (unbounded) geometry when a pressure profile is given. Figure 7.5 shows a few examples of free geometries calculated by the model.
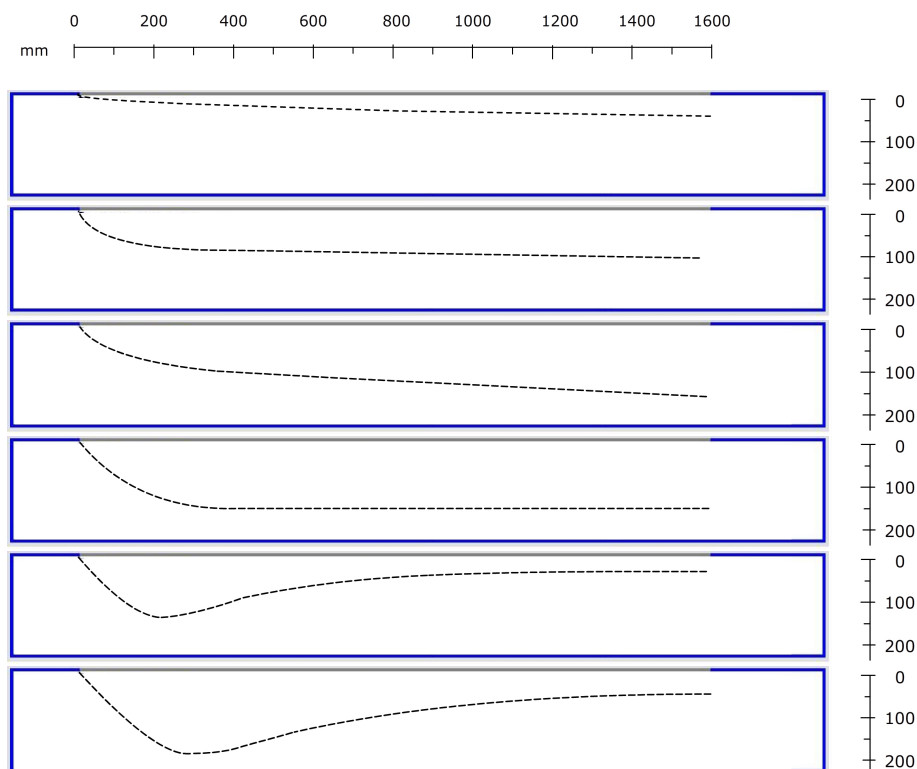
Figure 7.5: example geometries generated by the flow model

7.2.3   using the geometry model to calculate the actuator strokes

Also the geometry model implementation is adapted. Now a duct geometry is specified and the actuator strokes to set the plate positions need to be calculated as in figure 7.6.

Input **Output**

duct geometry, $A_1...A_n$ ⟶ geometry model ⟶ actuator strokes, S_{A1} S_{A2}
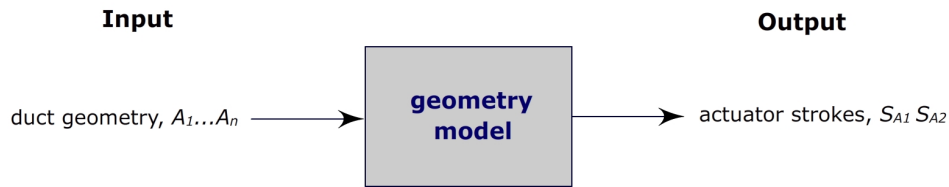
Figure 7.6: inputs and outputs of the geometry model with geometry input

But first another function in the geometry model implementation has to be added:
The flow model now produces a free, unbounded geometry. The test section is only equipped with two movable plates and two actuators to produce this geometry. Therefore the plates have to be fitted into the free geometry. To search for the best fit an optimization of the plate positions is done. It uses a least square optimization (Gauss,1794 ea); the sum of square position deviations from the calculated free curve is minimized. Some examples of the fitted plates into the calculated free curves are given in figure 7.7.
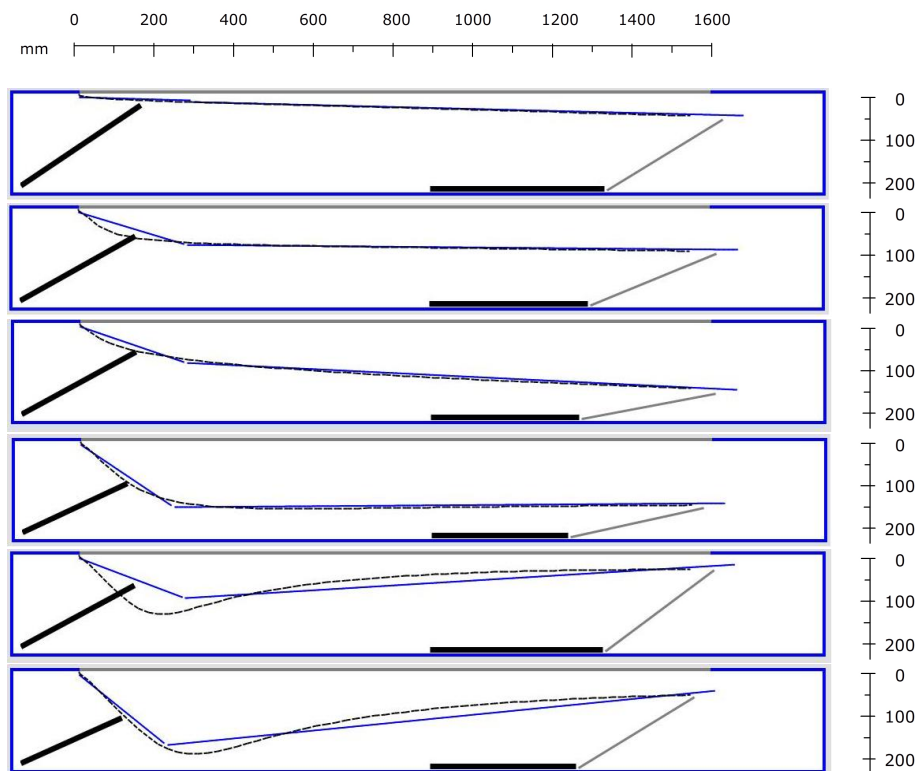
Figure 7.7: example fittings of the plates into the geometries

The plate fitting will of course generate errors, when the input pressure distributions are unconstrained. The suction duct can not produce the geometries calculated but it will find

the best fit. The contribution of these errors to the total control system error, is further explored in section 7.3.

With the plate positions calculated the geometry can produce the actuator strokes to set the position of the plates in the duct.

7.2.4   controlling the actuators

To actually put the plates into position, the actuators have to move to their calculated strokes. The actuators however are controlled with a speed driver and a direction control. It can either go forward or backward at a desired input speed. A position controller is implemented in a controller interface with a small processor. It uses a proportional feedback controller which uses the position read out of the actuators as feedback input parameters. The position controller is illustrated in figure 7.8.
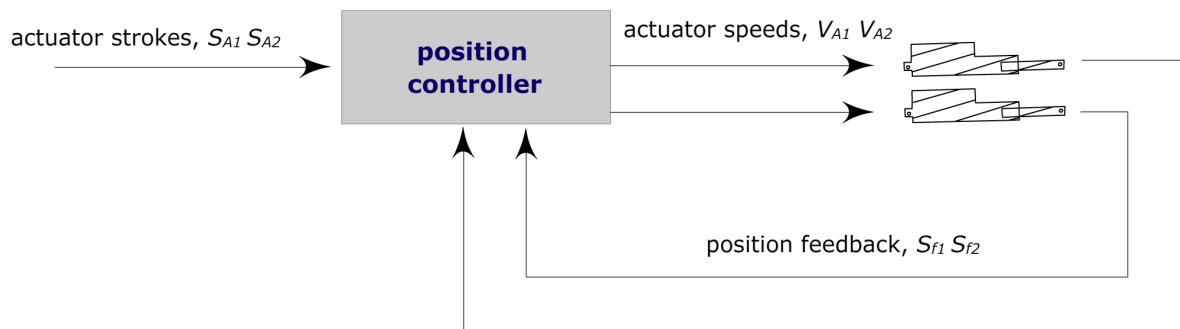
Figure 7.8: a feedback position controller to control the actuator positions

The controller will drive the actuators until the desired calculated positions are reached. The speed is proportional to the error between the current position and the desired position set points.

$$V_A = Kp \cdot (S_A - S_f) \tag{7.1}$$

Here V_A is the actuator speed, Kp, is the amount of error response. S_A-S_f is the current position error. So when the actuator is far away from its position set point, it will move faster. It will move slower when reaching its set point.

The position controller will reach its calculated set point very accurate and produces only marginal errors to the present errors of the geometry model of section 5.4.

With the ability of positioning the plates to its positions, the controller is finished, and measurements on the accuracy of the total controller can be done. The results are in the next section.

7.3 correctness and accuracy of the controller (measurements)

To determine the accuracy of the controller again pressure measurements are done. The plates in the suction duct are controlled to produce 20 different given pressure curves. The pressures are measured again at 16 places in the duct and compared to the desired pressure distribution. The overall results of these measurement are given in table 7.1.

RMS errors		pressure	units	suction speed	units
	overall	28.6	Pa	0.029	m/s
		6.08	%	4.36	%
	highest	72.9	Pa	0.06	m/s
		12.85	%	8.98	%
arithmetic mean errors		pressure	units	suction speed	units
	overall	+6.5	Pa	+0.003	m/s
		+0.94	%	+0.23	%

Table 7.1: open loop controller accuracy

Again here the arithmetic mean errors looks very promising, but are not very useful to define the deviation from the wanted set point pressure curve. In the arithmetic mean error the positive and negative errors cancel each other out. Figure 7.9 gives an example of a good arithmetic mean error, but a inaccurate pressure shape. The negative and positive errors cancel each other out when a mean error is calculated. Again here the RMS (root mean square) is a much better base to define the quality of the control system.
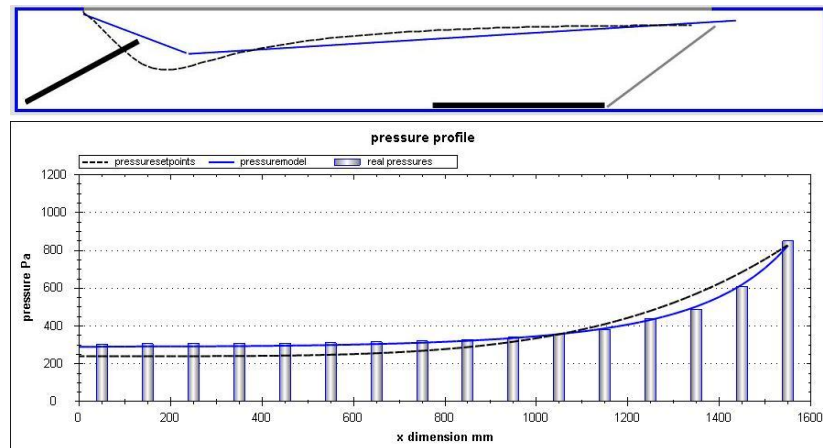
Figure 7.9: example geometry and curve with low mean error and relative high rms error

One of the causes of the error in this control system is due to the fitting of the two plates into the free geometry calculated by the model. To determine the contribution of this error, the pressure distribution is also calculated by the model. This pressure calculation is based on the geometry of the fitted plates. This error is calculated in the same way as in section 6.6.1. But now for these specific measurements. When subtracting these model errors from

the total errors, the contribution of the error caused by fitting the plates can be calculated as in figure 7.10. The results are in table 7.2.
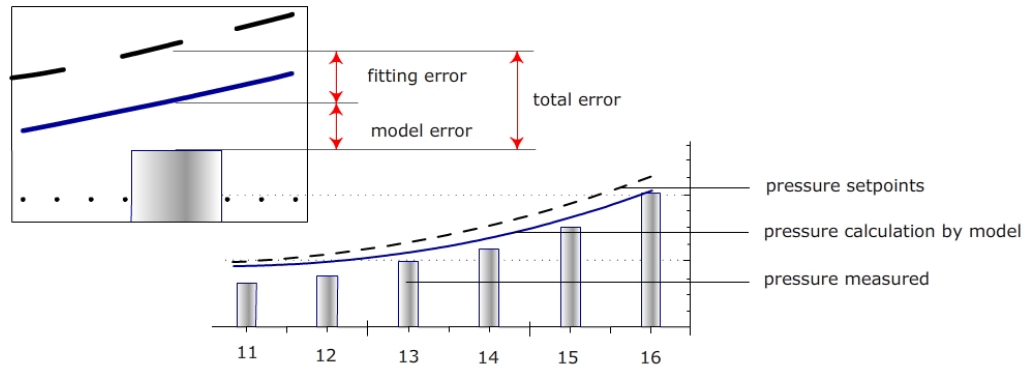
Figure 7.10: fitting error contribution calculation

pressure RMS errors	total error	model error	fitting error	units
overall	28.6	18.7	9.9	Pa
	6.08	3.82	2.25	%

suction speed RMS errors	total error	model error	fitting error	units
overall	0.029	0.018	0.011	m/s
	4.36	2.61	1.75	%

Table 7.2: error contribution of the fitting of the movable plates in the calculated geometry

The normalized RMS errors in the model itself are overall 3.82% for the pressures and 2.61% for the suction speeds, from these measurements. The total measured errors are 6.08% for the pressures and 4.36% for the suction speeds, this gives an additional 2.25% error for the pressures and 1.75% for the suction speeds, caused by the plate geometry deviation from the calculated geometry by the model.

7.4 error causes and optimization

The Matlab implementation calculates an unconstrained geometry given a pressure distribution or suction distribution. Because it is unconstrained the solution will iteratively converge to a geometry solution for every monotonically decreasing pressure distribution in the duct. In the duct however the geometry is constrained by the two movable rigid plates. The fitting of these plates in the unconstrained geometry causes errors, as seen in the previous section. When the Matlab implementation of the model is adjusted for the constrained geometry, this errors can be reduced. However it will not converge to a solution for every input, so also the available input pressure and suction distributions have to be further constrained.

The fitting of the position of the two plates will generate a geometry of the duct that is closest to the calculated geometry. This is not necessarily the optimum with the smallest error on the pressure distribution. A better strategy would be a best fit optimization of the pressure distribution or suction speed distribution. However in this case processor capacity problems occur. The available pressure and suction distributions need to be calculated over the plate position domain. To calculate this real time, over the actuator domains, with 1 mm accuracy, more than 10,000 calculations of the flow model implementation are needed. With the iterative solver this takes even on a fast processor over two hours of processing time. The geometry fit of the plates can be found with a fast processor within 200 ms.

Chapter 8

Closed loop control

This chapter will study the usability of a small feedback system to control the pressure distribution. This is done with a simple optimization technique.

8.1   control method

The controller in the previous chapter uses the model of the system as a base to control the movable plates in the duct. The controller explored in this section will not use this model, but uses the real time measured pressure distribution to optimize the plate positions. These measurements are used as a feedback input for the controller. It will use the error between the desired pressure distribution and the measured pressure distribution as a base for its control as illustrated in figure 8.1.
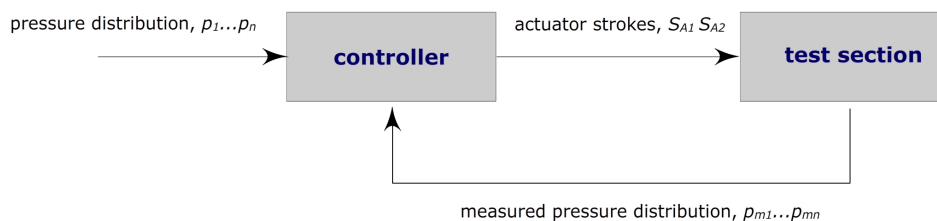
Figure 8.1: diagram of a feed back controller for the system

To study the usability of a feedback controller in the suction duct system, a simple optimization program is written. The controller uses two state machines as illustrated in figure 8.2, one for each actuator. The simple optimization program will increase the length of one actuator, state I, if this search direction is converging to a smaller error, it will search further in this direction, until no further improvement is found. Then, in state II, it has to step one step back to get back to the lowest error in this search direction. In state III it will try the

other search direction by decreasing the length of the actuator, then again until no further improvement in state IV it has to step back to its previous position. This process is then repeated for the other actuator, and further repeated until no further improvement on the error is found.[1]
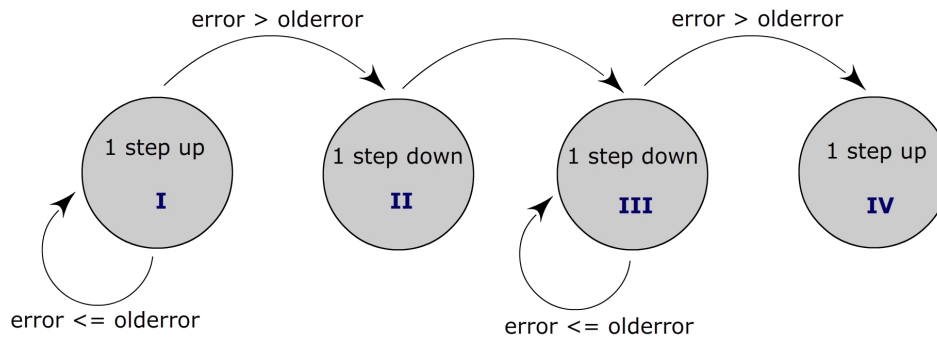
Figure 8.2: simple state machine used for the feedback optimization

8.2 implementation controller

To compare the usability of a feedback controller to the open loop controller of the previous chapter, the optimizer is implemented in the same (small) processor as the position controller from section 7.2.4. This controller reads out the current pressures, calculates the current error, and positions the actuators according to the state machine in figure 8.2. For testing purposes it gets a desired input pressure distribution from a computer, and sends back information about its system state. This information is used in the next section for comparison and to determine the accuracy of the controller.

8.3 correctness and accuracy of the controller (measurements)

To determine the accuracy of the feedback controller, the measurements of the previous chapter with the open loop controller are repeated. In addition also the feed back controller will try to find a geometry of the plates which generates the smallest rms error over the pressure curves. In this way the performance of the feed back controller can be compared to the performance of the open loop controller. The results of these tests on 40 different pressure distributions are in table 8.1. In addition also the feed back controller will try to find a geometry of the plates which generates the smallest rms error over the pressure curves.

---

[1] In the optimization chosen, the controller always starts in the same direction, when progression is made is will continue optimizing in that direction. As an alternative the controller could look around first to all its neighbours, and determine which direction converges fastest. But for this control system it would slow down the controller, because with every step it has to actually move to all its neighbour positions to get information on the converging speed. So for this controller the naive approach is chosen.

In this way the performance of the feed back controller can be compared to the performance of the open loop controller. The results of these tests on 40 different pressure distributions are in table 8.1.

pressure errors		feed back		open loop	
	overall	19.7	Pa	31.6	Pa
		3.35	%	5.94	%
	highest	47.62	Pa	72.91	Pa
		8.08	%	12.85	%

suction speed errors		feedback		open loop	units
	overall	0.019	m/s	0.029	m/s
		2.67	%	4.67	%
	highest	0.056	m/s	0.092	m/s
		7.61	%	11.26	%

Table 8.1: feedback controller accuracy and comparison to the open loop controller accuracy

In table 8.1 can be seen that for these measurements the open loop accuracy of the open loop controller is 5.94 % error on the pressure curve and 4.67 % on the suction speed distribution. This is consistent, within about 0.5 %, with the previous measurements done with only the open loop controller (section 7.3 and table 7.1). But more important, from the table can be seen that the feedback controller is more accurate than the open loop controller for these measurements. With 3.35 % overall rms error on the pressure distributions and 2.67 % for the suction speed distributions, the feedback controller is almost twice as accurate as the open loop controller on the measurements done.

8.4   error causes and optimization of the controller

The simple hill climbing algorithm used tries to find pairs of actuator positions in which the error is in a minimum. While searching for minima it uses only the information of the current error, and the previous errors. When the system arrives at a position with a minimum error, the system does not have the information on this position pair being a local or global error minimum. To study this problem, the model from previous chapter is used to simulate the optimizer in Matlab.

8.4.1 simulation of the controller

To simulate the controller first the search domain of the controller has to be defined. This domain consists of the safe actuator positions from section 5.2. The first actuator has, with an accuracy of 1 mm, 116 different positions. The second actuator with a stroke length of 172 mm can be at 172 different positions. As a result the plate positions can form $116 \cdot 172$, or about 20,000 different geometries. Half of these geometries are denoted unsafe, so about 10,000 positions are within the search domain of the controller.
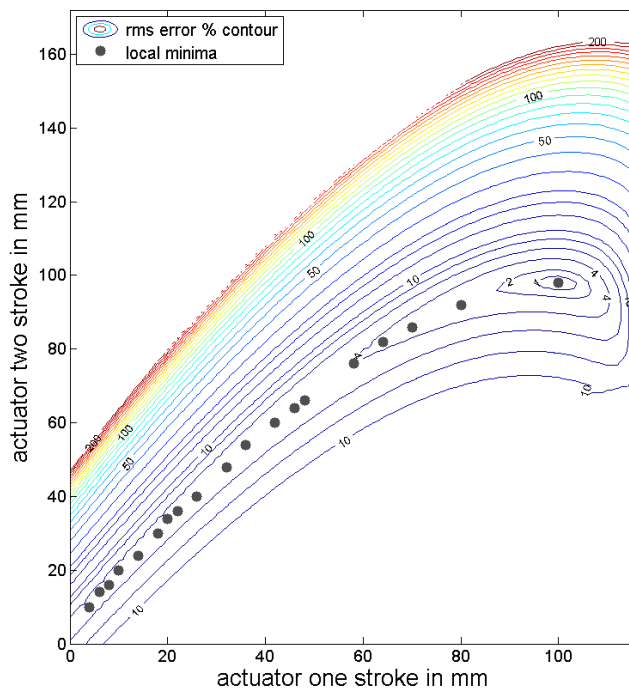
Figure 8.3: error distribution on different actuator strokes

The flow model is used to calculate all pressure distributions on these 10,000 different geometries. This dataset is used to simulate the optimization of the controller. Given a desired pressure distribution, all potential or possible pressure distributions are defined by the data set. So all potential or possible errors can be calculated. For an arbitrary desired pressure distribution input, the distribution of rms errors is visualized in figure 8.3. Again here different actuator position pairs (on the x and y axis) generate different errors (contour plot). In this error data the optimizer is simulated.

The simulation paths of different optimizations are shown in figures 8.4 and 8.5. They are representatives of all duct shapes that can be produced by the movable plates.
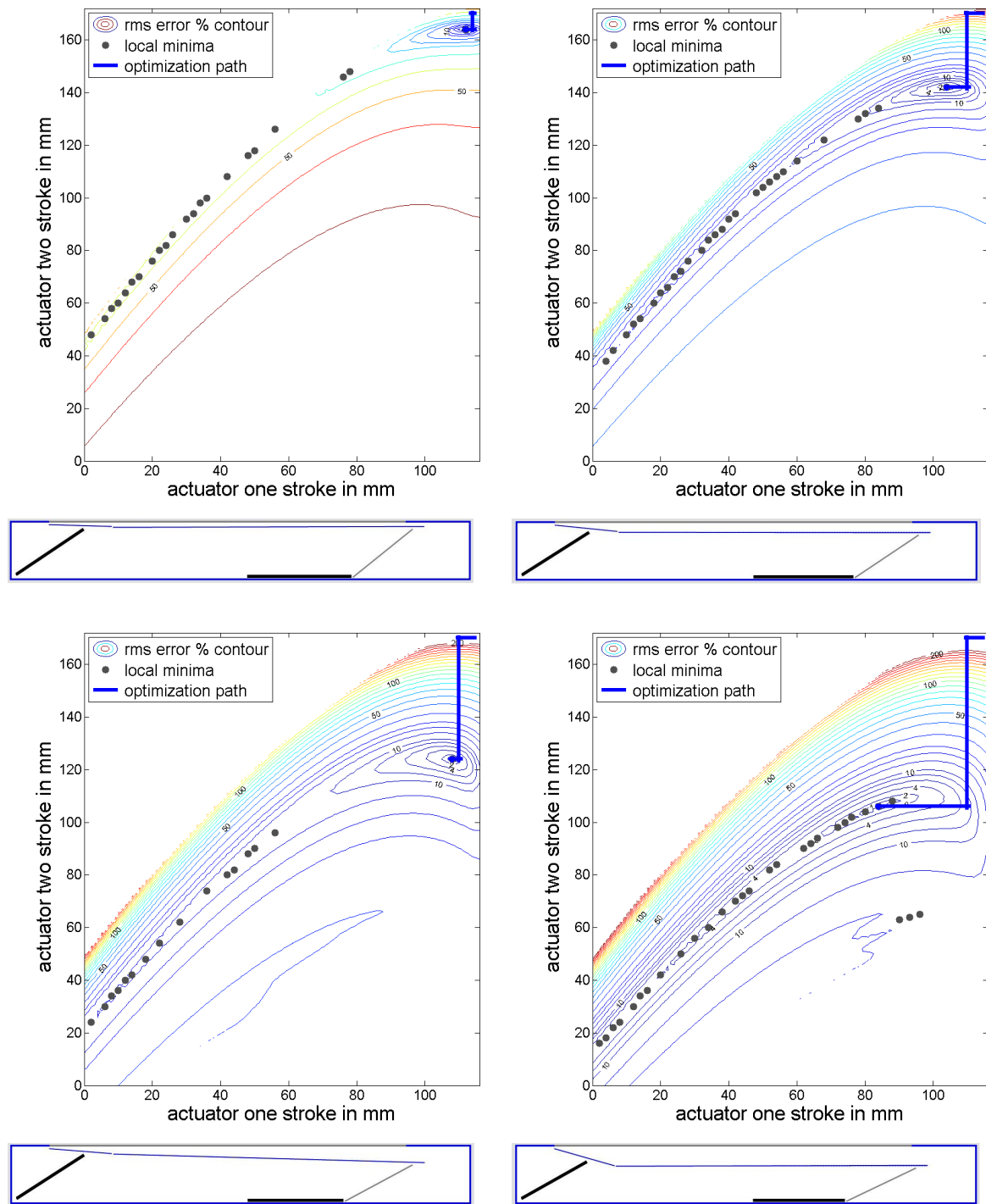
Figure 8.4: optimization through error distribution 1

In the contour plots can be seen that multiple local error minima exist. To avoid optimizations to these local minima, the start positions of the actuator strokes were chosen 172 and 116
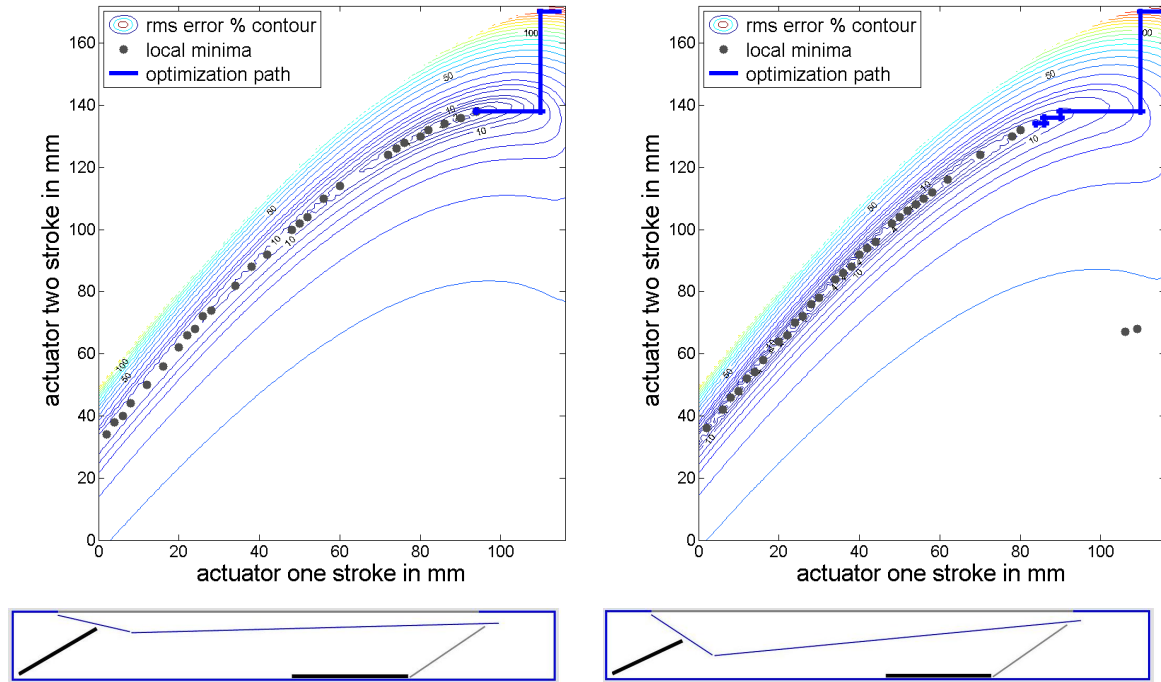
Figure 8.5: optimization through error distribution 3

mm. Here the actuators are in their maximum positions with the movable plates at the upper side of the suction duct. In the contour plots can be seen that this is also the area with the steepest error response. The optimization paths beginning in this starting position are also plotted in the contour plots.

From the simulations it is found that not all optimization paths end in the global minimum. The results of simulations with 2000 different input pressure distributions are in table 8.2. The simulations are done with input pressure curves which can be produced by the duct geometry. So every simulation has a global minimum error of 0%.

	4 direction search		8 direction search	
average minimum found	3.18	%	2.49	%
highest minimum found	26.79	%	19.00	%

Table 8.2: minima found by the simulations of the optimization controller

In table 8.2 also the simulation results for an optimization controller which can search in all 8 possible directions is given. This controller can move both actuators in and out, giving 4 search directions illustrated in figure 8.6a. In addition it can move both actuators at one time; both up, both down, one up one down, and vice versa. This gives another 4 search directions as illustrated in figure 8.6b.

Figure 8.7 gives the distribution of the found minima on the different actuator settings. The highest found minima are all in the same area. For this area the simple optimization technique
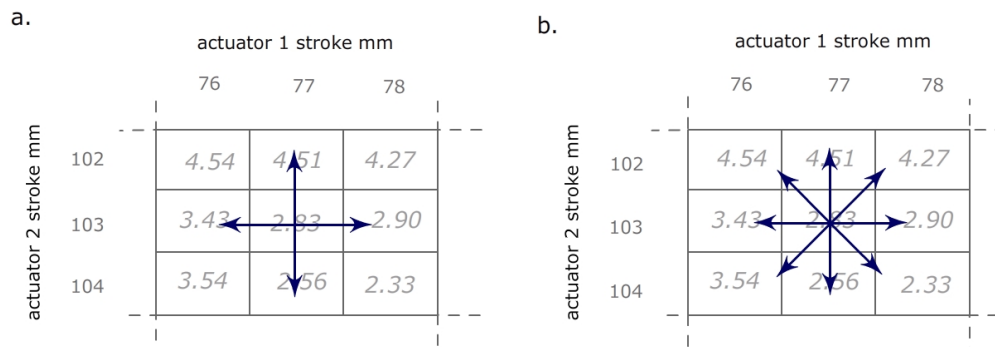
Figure 8.6: the search directions of the optimizers

used, will find relative large local minima (above 10% error). The duct geometry and pressure profile shape in this high area are given in figure 8.8.
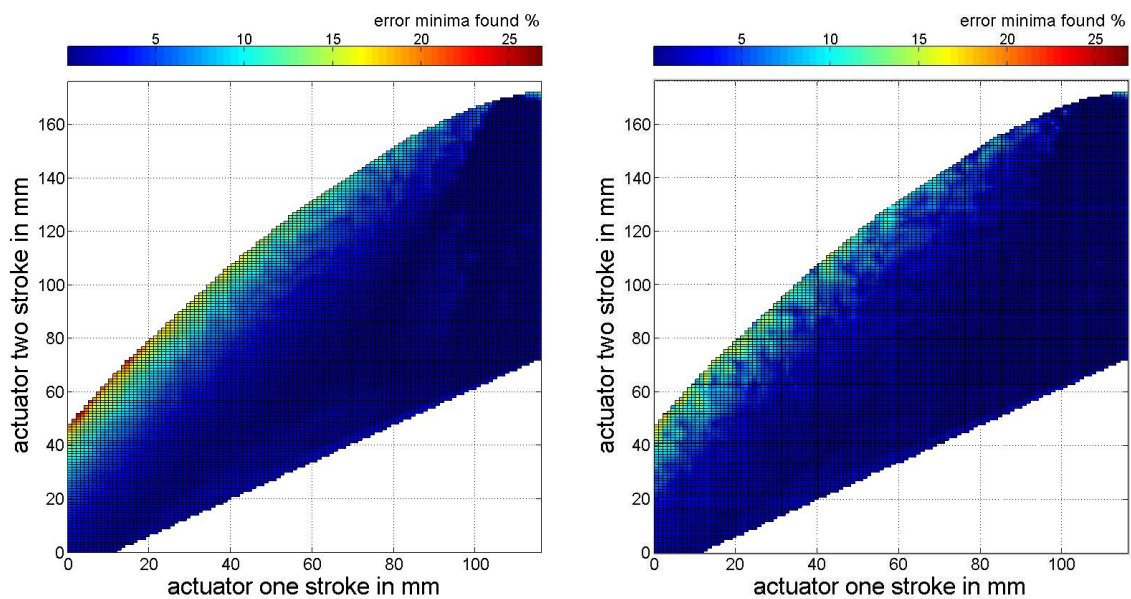
Figure 8.7: found minima for 4 direction optimization (left) and 8 direction optimization (right)

For the geometry shapes as in figure 8.8 the simple optimization technique finds relative high minima. For all other geometries is will find minima $\leq 3\%$ in the simulations done. This is consistent with the measurements done in the previous section (3.35 % overall error) for the 4-direction controller.

The model can be used to explore optimization techniques, and optimization starting points. It is already learned that for example the 8-direction controller performs better than the 4-direction optimizer. Furthermore it is seen that for a specific pressure distribution and duct geometry this optimizer is not useful (figure 8.8).
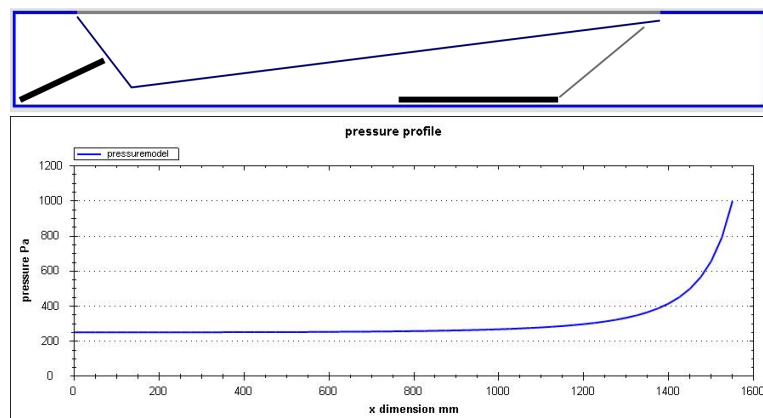
Figure 8.8: geometry and pressure distribution shape with relative high found minima

Chapter 9

Wind tunnel integration

In this chapter the usability of the tested model and measured test section in a wind tunnel is further explored.

9.1   wind tunnel requirements

When the system is to be integrated into a wind tunnel floor, the system can be tuned and calibrated for different requirements:

1. maximum additional pressure gradient caused by the boundary layer suction system
2. maximum angularity effect caused by boundary layer suction.
3. amount of boundary layer after the suction system.
4. amount of boundary built up between the suction system and the test section.

These requirements are explained in section 3.3. They may vary for different wind tunnels or different test scenarios in the same wind tunnel.

The system studied in the previous chapters is a system in which the pressure distribution and suction distribution can be controlled over the suction surface. In an ideal situation for a given wind tunnel a test scenario, this distribution can be calculated, with the above requirements satisfied. More likely, the distributions will be found by measurements of the above parameters in the wind tunnel. Examples of wind tunnel measurement techniques can be found in Appendix C.

9.2   system scaling

9.2.1   width scaling

For the integration in a wind tunnel the system needs to be scaled to a size that is appropriate for a wind tunnel floor. All models and flow properties studied in this research are studied

without the friction from the side walls of the suction duct. The model used can therefore be scaled in width without loss of accuracy. However it is important that the underpressure generated by the pump has no gradient over the width of the suction section as in figure 9.1.
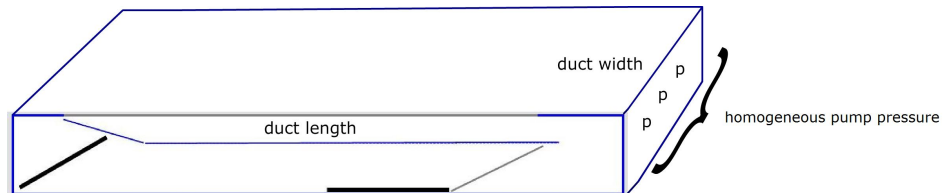
Figure 9.1: suction duct with no pressure gradient over the width of the section

9.2.2 length scaling

The length of the duct has a major influence on the system's behaviour. The suction section of the duct studied in the previous chapters has a length of 1600 mm. For a system design in a wind tunnel, different duct lengths can be studied with the flow model produced, but it is not verified by measurement, for other duct lengths than the 1600 mm of the test section[1].

---

[1]The model can be used for calculating flow properties is longer and shorter ducts, large differences in accuracy are not expected

9.3   system control inputs

The wind tunnel section should have an easy to control suction distribution, so the suction system can be tuned iteratively. In a first test the tuning can be done manual, in a later stadium this tuning can be automized. As an example the total volume of air that is sucked away can first be controlled, where after the suction distribution of this volume is adapted by two set points. In total three set points are defined:

1. total suction volume control

2. suction drop factor B/A

3. suction drop curvature from A to B

Here A and B are defined as in figure 9.2
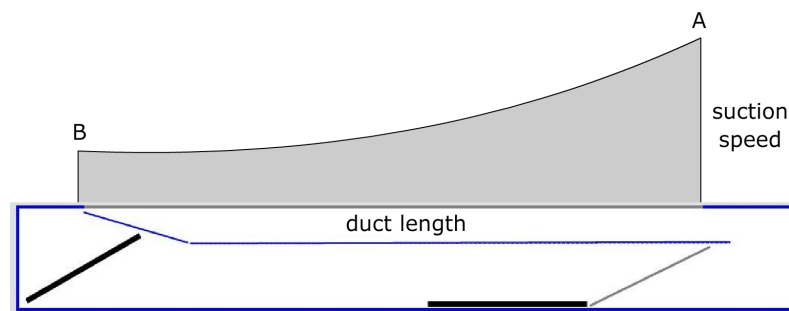
Figure 9.2: suction gradient control inputs

The measure of curvature from A to B is defined here as the area under the suction curve normalized to the area under the suction curve of the linear case as in figure 9.3
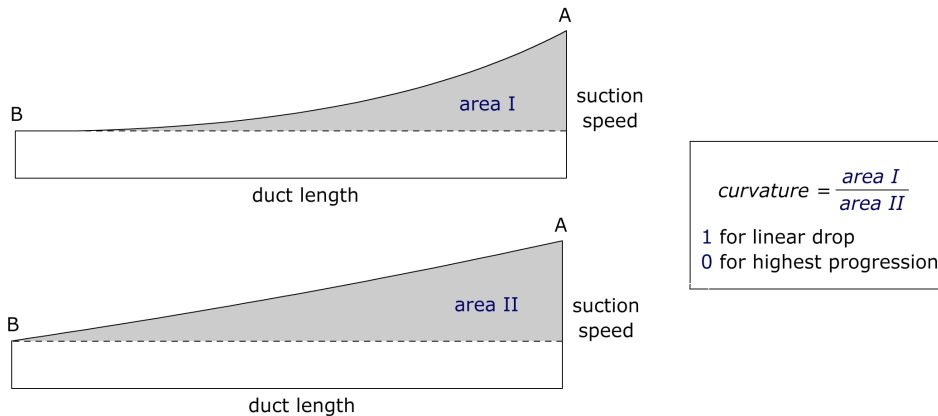
Figure 9.3: curvature definition

9.4 design parameters

For a full scale wind tunnel section the following design parameters are of interest:

1. the ranges of the system control inputs as in figure 9.2
2. the available height in the wind tunnel to build in the system (available space under or on a wind tunnel floor)

The range of the system control inputs has to be chosen and will determine the range of suction volume flows as well as the range of suction distributions that can be generated. Furthermore, the height of the system determines the range of geometries that can be made, and influences the range of suction distributions as well. The height of the system together with the available pump characteristics (volume flow and underpressure) determines the range of suction distributions that can be produced by the system.

For the wind tunnel suction system, again the model can be used to choose between different control input ranges, system heights and pump characteristics needed. As a base for this selection again the flow model can be used, to generate all flow parameters on the actuator stroke domains. The design parameters with a pump underpressure of 400 Pa are given in figure 9.4. The data in plots like figure 9.4 can be used to see which suction distributions can be made with a specific system height and pump underpressure (in this case 400 Pa). An example design specification is generated in this way in the next section for the Audi Aeroacoustic Wind Tunnel.
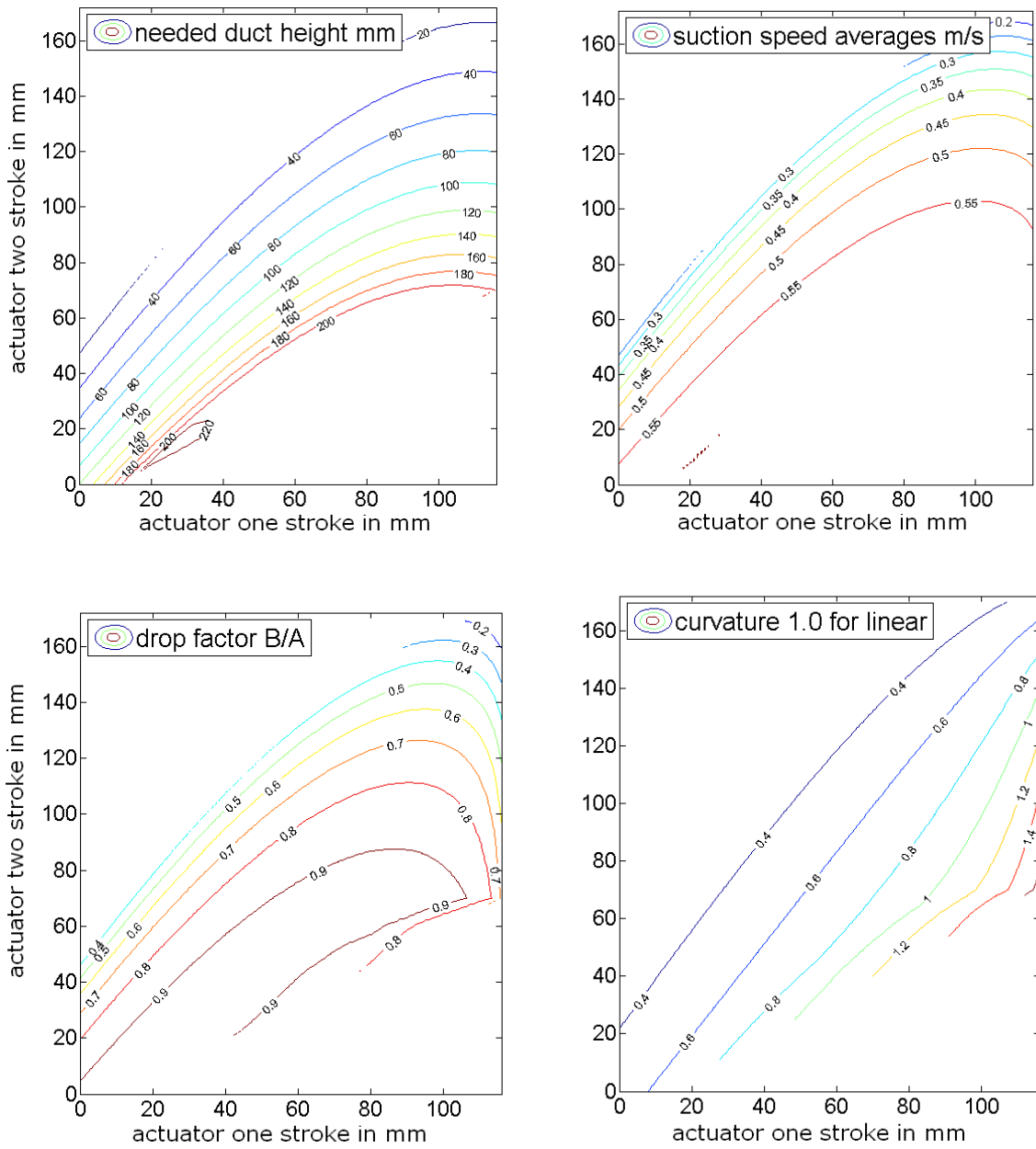
Figure 9.4: contour plots of the different design parameters @ 400 Pa pump underpressure

9.5   example design case

9.5.1   the Audi Aeroacoustic Wind Tunnel

As an example design case an integration of the system in the Audi Aeroacoustic Wind Tunnel is given in this section. A detailed description of the wind tunnel can be found in reference [15]. This tunnel is a wind tunnel with an open test section and a nozzle exit of 3.94 m in width. At the end of the nozzle exit in the ground plane of the tunnel, a boundary layer suction system already exists. The volume flow needed to remove the boundary layer coming out of the nozzle are given in table 9.1.

|	suction volume flow	section length	section width	suction speed
existing suction system	6.04 m^3/s	0.80 m	3.94 m	1.92 m/s
adaptive suction system	6.04 m^3/s	1.60 m	3.94 m	0.958 m/s

Table 9.1: volume flow properties of suction systems in the Audi Aeroacoustic Wind Tunnel

So when the air in the wind tunnel flows with 160 km/h (44.4 m/s) in this wind tunnel, a volume flow of 6040 l/s (6.04 m^3/s) $is used to remove^2 the boundary layer over a width of 3.94m.$

The volume flow of the existing suction system of 800 mm in length, will be used to get an indication of the suction speeds needed on a system with a length of 1600 mm. Here the assumption is made that the total volume flow of air needed to be sucked away is the same on suction systems of different length and equal width. This gives only an indication on suction speeds and suction volumes of a longer suction system, but it is usable to select duct geometries and to determine pump capacity ranges.
For the adaptive system a length of 1.6 m is chosen and a width of 3.94 m. To reach the same volume flow as in the existing suction system (6.04 m^3/s), $an average suction speed of 0.958 m/s is needed over the$

9.5.2   choice of system input ranges

So an estimate for the required average suction speed over the full scale adaptive suction section is 0.958 m/s. For system flexibility, the range of the suction volume is chosen to be 0.8 to 1.1 m/s. As a result, the system is able to reach suction volume flows from 5000 to 6900 l/s.

To be able to produce this suction speed range, the needed underpressure of the pump has to be found. The model of the system is used to generate information on different pump underpressures, and suction speed ranges as shown in figure 9.5. It can be seen from figure 9.5 that at 1000 Pa the required suction speed range of 0.8 to 1.1 m/s can not be reached. Therefore pump underpressure is increased to 1200 Pa. In the second contour plot of figure 9.5 can be seen that at 1200 Pa the full suction speed range is available.

---

[2]the velocity of air at the downstream end of the section at 2 mm above the ground plane is 99% of the free stream velocity in the tunnel
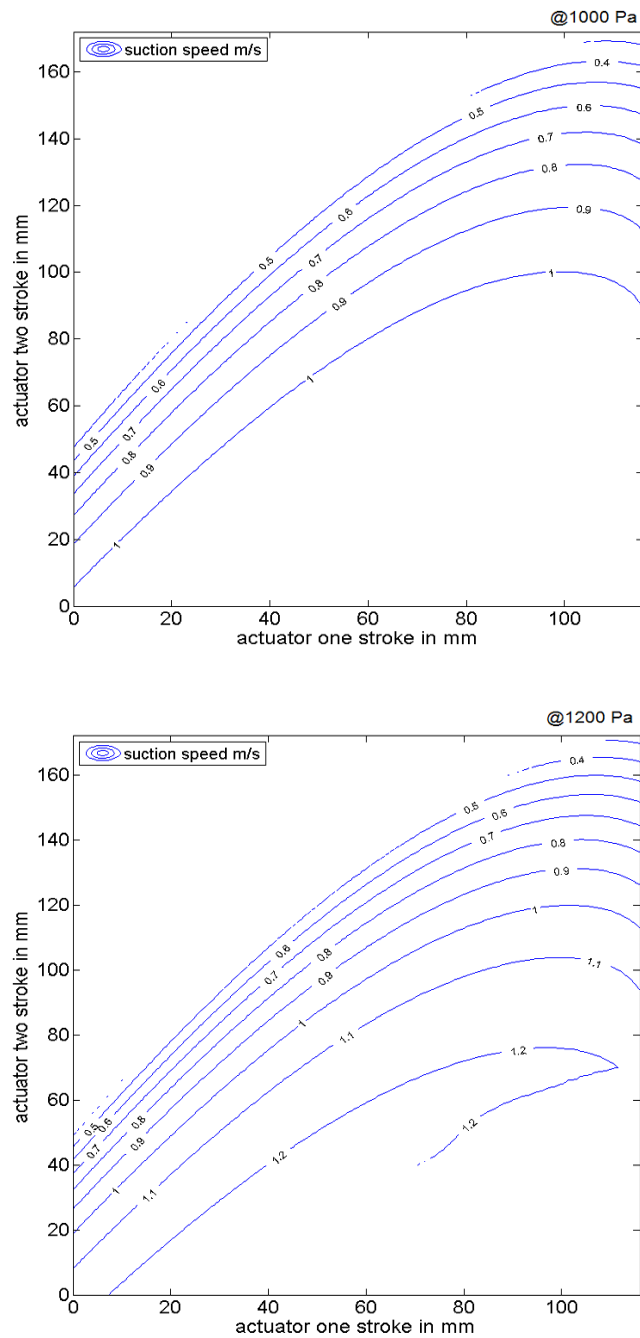
Figure 9.5: suction speed ranges at 1000 Pa (top) and 1200 Pa (bottom)

When the contour plots of all the design parameters are combined, the other available ranges of the design parameters can be read out; the height of the system needed to produce this suction speeds can be read from figure 9.6. Here can be seen that a duct height of about 120 mm can produce the specified suction speed range at 1200 Pa pump pressure. The available
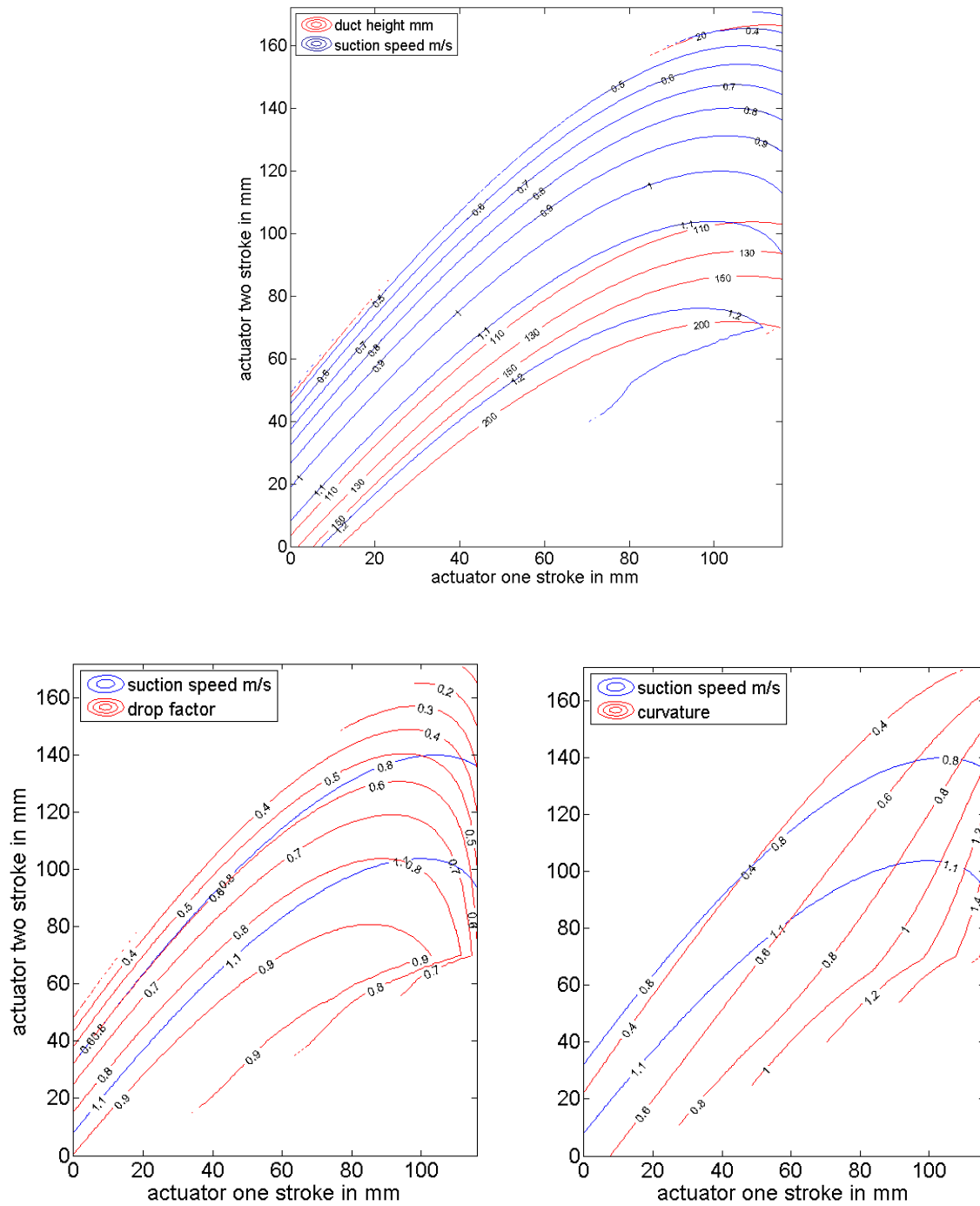
Figure 9.6: height needed, available drop factor, available curvature, at suction speeds from 0.8 to 1.1 m/s at 1200 Pa

drop factor and curvature ranges can be read from the other graphs of figure 9.6. It can be

seen that the drop factors in this range lie in between 0.4 and 0.8, and the curvature factors between 0.3 and 1.1. A visualization for the total case is given in figure 9.7.
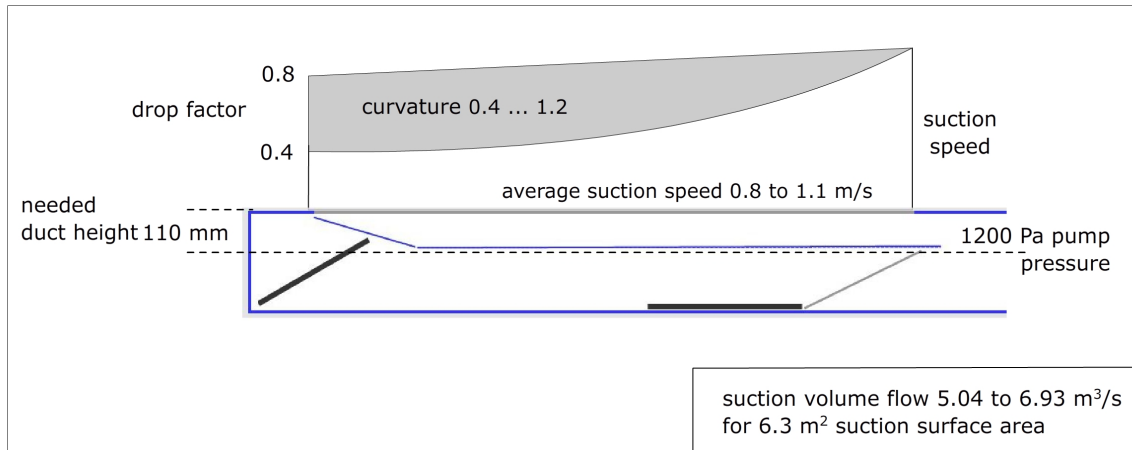
Figure 9.7: summary of the system input ranges in the Audi Wind Tunnel case at 1200 Pa

Chapter 10

Conclusions and recommendations

As an overall conclusion from this research, it is found that a suction distribution over a porous material can be controlled by the adaptive geometry of the proposed system, with an accuracy of <4% in suction speed error.

10.1 conclusions

10.1.1 context

It is found that in a wind tunnels different techniques are used to reduce the boundary layer on the ground plane of the wind tunnel test section. One of these techniques is boundary layer suction. As a disadvantage of this technique it is noticed that the systems generate undesired pressure gradients and angularity effects in the airflow.

An adaptive suction system is introduced that can reduce the undesired effects by controlling the suction distribution over the surface of a suction duct. This is done by adapting the geometry of the suction duct with two actuators.

10.1.2 models

A mathematical model is derived for the airflow in a suction duct of different geometries with one porous side. The model is implemented in Matlab in a transparent way, and contains 4 parameters sets; the duct geometry, the pressure distribution inside the duct, the velocity distribution of air through the porous side, and the velocity of air in the in the duct. When one of these parameter sets is given, the implemented model will produce the other 3. This model is verified by pressure measurements in the duct and it is found to be accurate within 5% for the pressures inside the duct. This generates errors within 4% in suction speed distribution.

10.1.3 control

To control the duct geometry a position controller for the actuators is implemented. Two techniques are studied to control and adapt the geometry of the duct. One is an open

loop control that uses the flow model as a base for its control and calculates on a given pressure profile inside the duct, the required duct geometry. The other is a feedback control which uses measured pressure data to optimize its geometry. The open loop control uses a computer and a lot of processing power to calculate the geometries. The feedback control uses a small processor with a simple optimization algorithm. The feedback controller was, based on measurements done, at least as accurate as the model based open loop control. The model however is found to be very useful for simulation and optimization of the feedback controller. With a closed loop controller that is as accurate as an open loop controller, the most suitable control technique for this system will be the closed loop controller. It requires less processing power, and does not necessarily need model updates, when changes in the system occur.

10.1.4   wind tunnel integration

To produce this system as a wind tunnel suction system, the control input ranges for this system are specified. They represent the capabilities of the suction system. They include, a pump pressure range, a system height, a suction volume range and a drop range in suction speed from one side to the other side of the suction system. Again the model of the system can be a powerful tool for designing a wind tunnel suction system.

10.2   recommendations

10.2.1   production

For the production of the system some improvements can be made by increasing the stiffness of the mechanical components used, so the play and flexing of the plates are reduced. Also the effect of dust in the porous surface can be studied to specify the needed maintenance on the system.

10.2.2   model improvement

The accuracy of the model used in this research can be improved further by adding an empirical or mathematical friction model for the airflow in the duct. The terms for the friction forces can be added to the force balance in the model.
The current model uses a uniform pressure surrounding the duct. For most applications, however, the pressure surrounding the duct will not be uniform, in addition also the suction itself will cause pressure gradients over the suction section. This effect should be studied further, and can be added to the model by correcting the relation between the pressure and velocity of air through the porous material for the outside pressures. The open loop control based on the model can be improved further by adapting the Matlab implementation for a constrained geometry.

10.2.3   wind tunnel measurements

Research must be done on the required suction distributions and input ranges required to reduce the undesired effects of conventional suction systems (pressure gradient and angular-

ity effects). In addition measurements on the system in a wind tunnel need to be done to quantify the value of the adaptive system. A feedback controller can be optimized further for the needed suction distributions and control input domains. Again model output data can be used for simulation and optimization of the controller.

Appendix A

Flow measurements

geometry:

measured pressure profiles:

Figure A.1: flow measurements geometry 1

geometry:

measured pressure profiles:

Figure A.2: flow model pressure measurements geometry 2

geometry:

measured pressure profiles:

Figure A.3: flow model pressure measurements geometry 3

geometry:
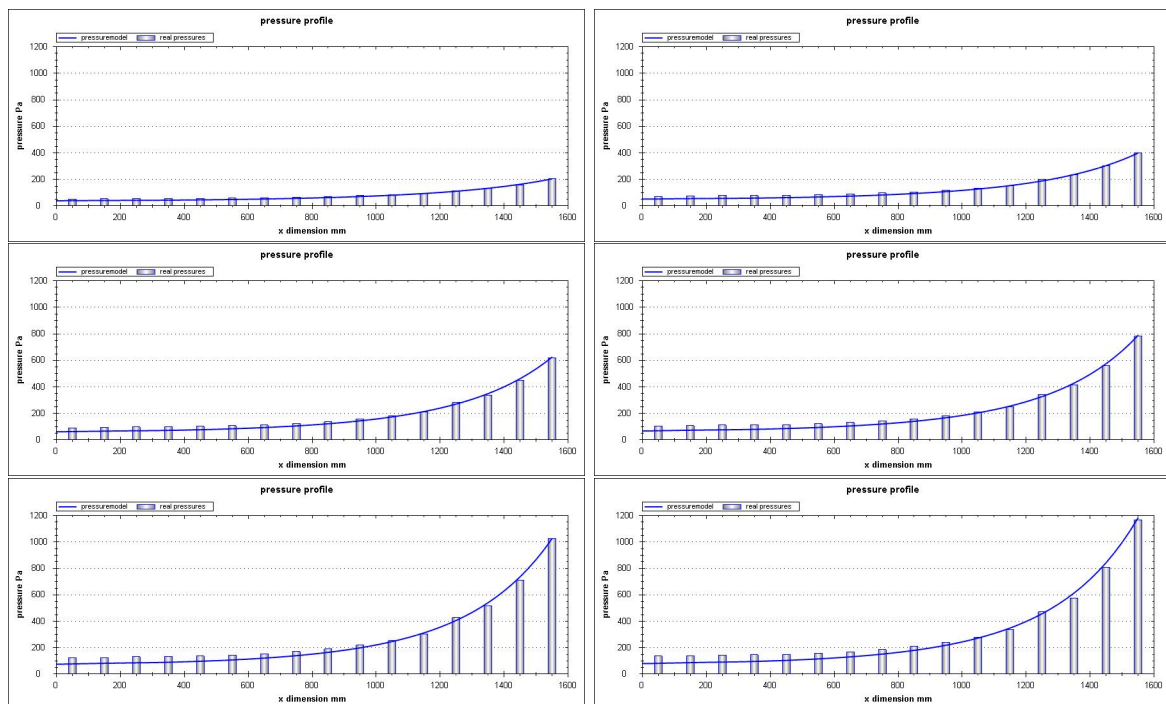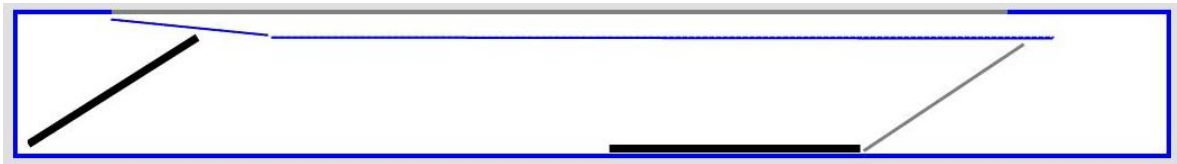

measured pressure profiles:

Figure A.4: flow model pressure measurements geometry 4

geometry:

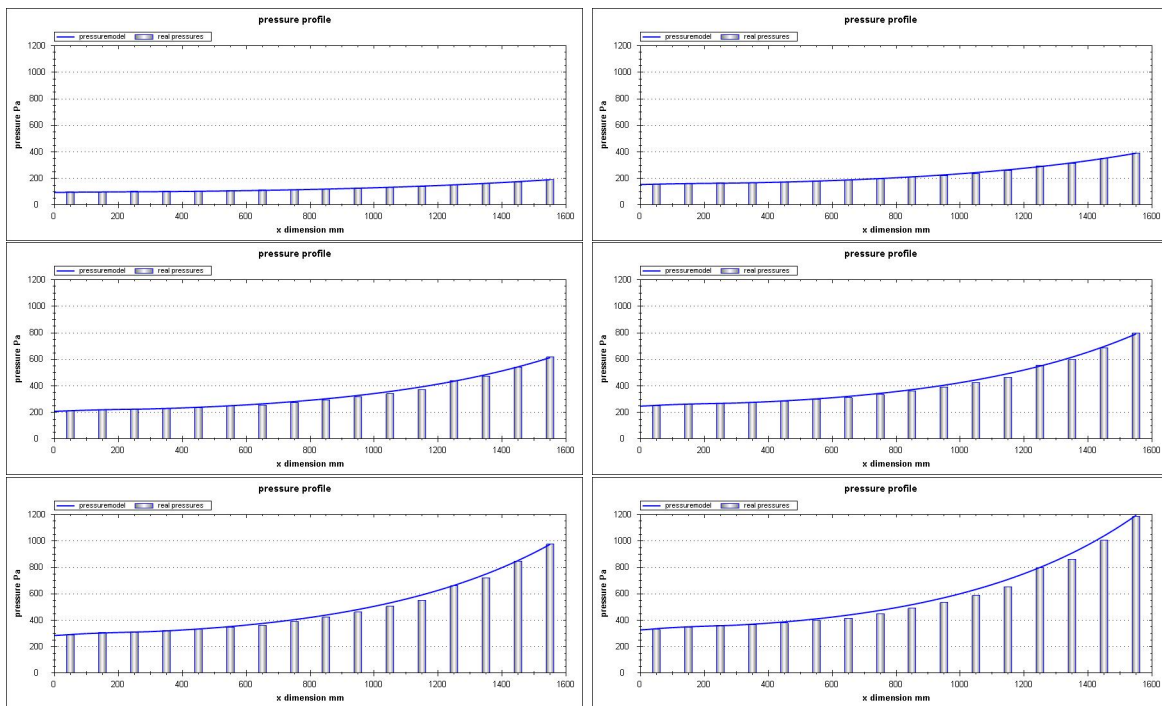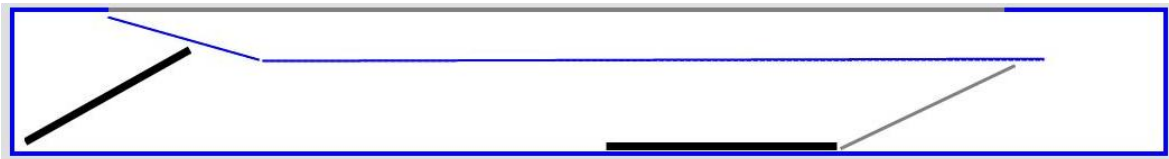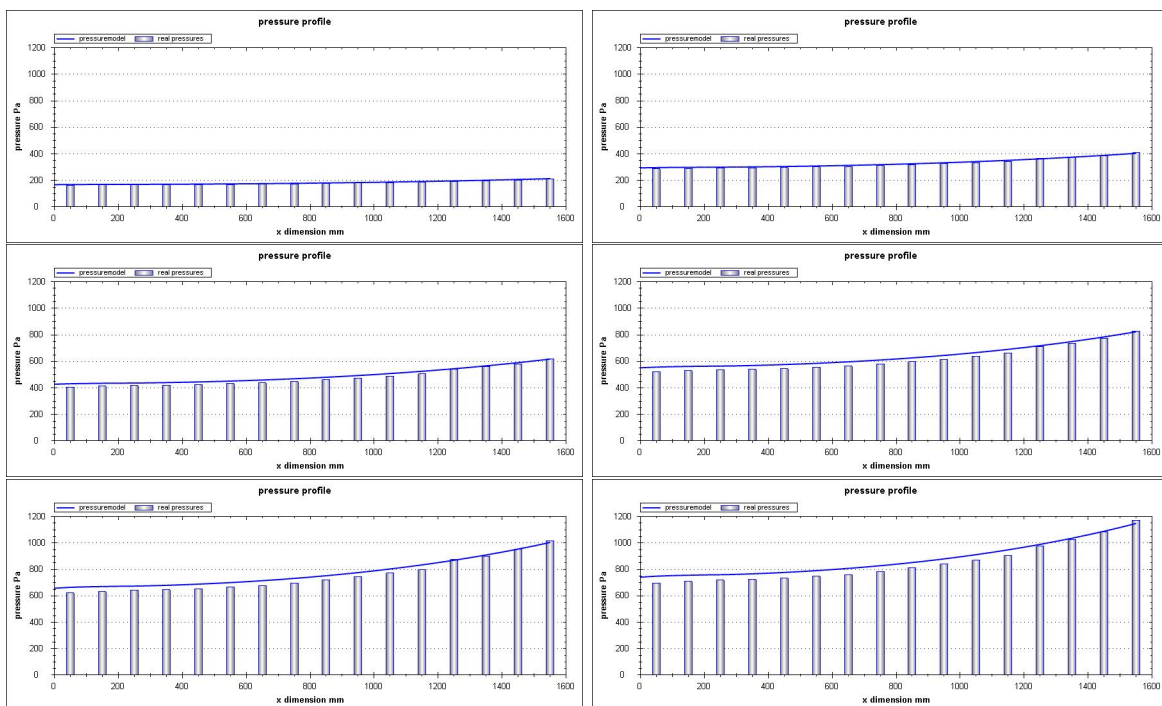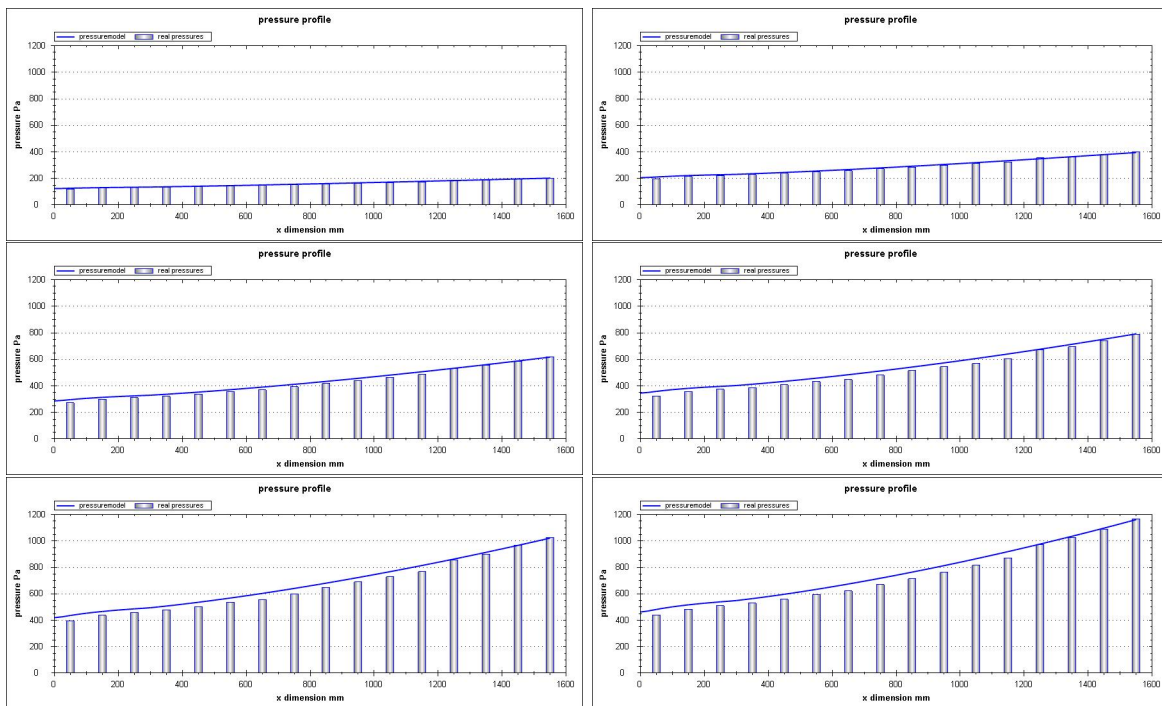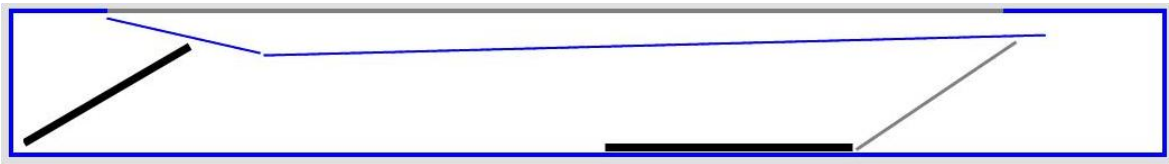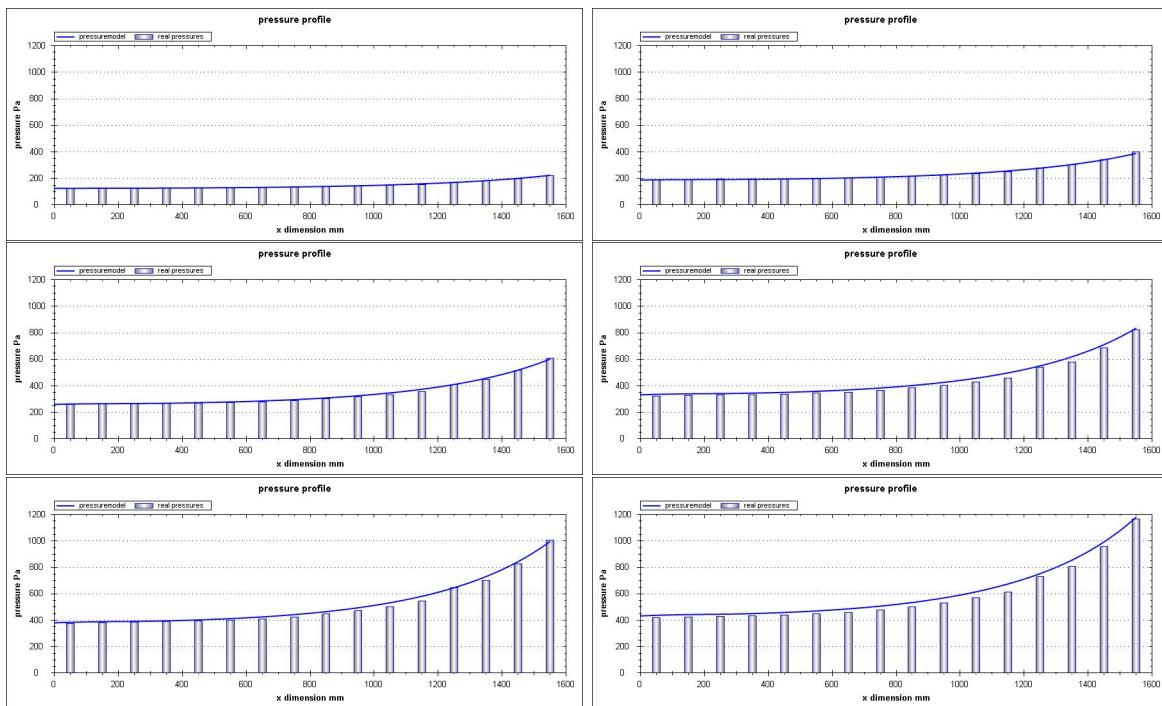measured pressure profiles:

Figure A.5: flow model pressure measurements geometry 5

geometry:
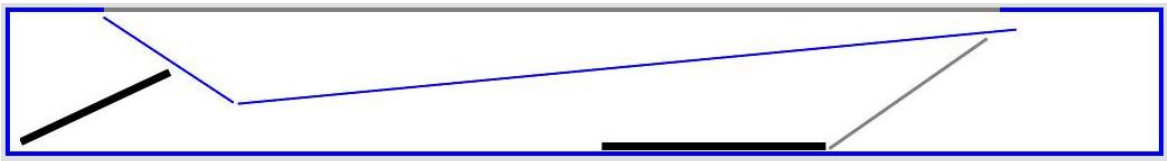
measured pressure profiles:
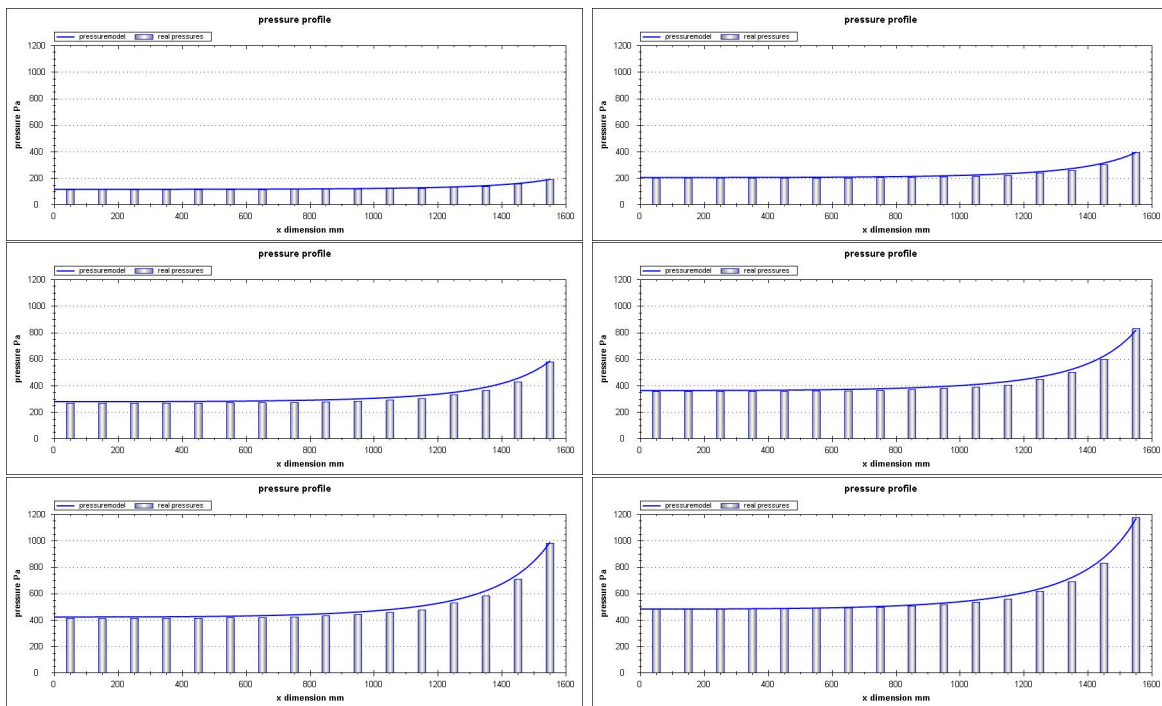
Figure A.6: flow model pressure measurements geometry 6

Matlab code flow model

```matlab
%**************************************************************************
%* Description: function generator for a ductflow with a porous side    *
%* author:       Jeroen Bink                                             *
%* context:      Master Thesis TuDelft @ Actiflow B.V.                   *
%* date:         June 2008                                               *
%* version:      0.4                                                     *
%*                                                                       *
%**************************************************************************

function F =...
generateEquationsA( x, A, As, rho, R1, R2 ,endpressure, startspeed, cc)

%-------------------------------------------------------------------------
% x:  vector with airflow parameters
%              1 to    cellcount+1 = speedvalues through pipe, V(i)
%     cellcount+2 to 2*cellcount+1 = speedvalues through porous skin, Vs(i)
%   2*cellcount+2 to 3*cellcount+2 = pressurevalues, p(i)
%
% A:  vector with pipe geometry (hights or surfaces from intersections)
%              1 to    cellcount+1 = cellhights(z) or cellsurfaces, A(i)
%
% As: cell length(x) or cellsurface (in case of surface, A must be surfaces)
%
% rho:           density of flow medium
% R1,R2:         friction coefficients from porous skin
% endpressure:   pressure at the last cell
% startspeed:    inlet speed at the first cell (0 for closed duct)
% cc:            celcount, the number of cells in the model
%-------------------------------------------------------------------------

F = [
%function specification in form  F(x)= 0, x a vector

        %massbalance
        A(2:cc+1).*x(2:cc+1)-A(1:cc).*x(1:cc)-As.*x(cc+2:2*cc+1);
        %A(i+1)*V(i+1)-A(i)*V(i)-As*Vs(1)=0

        %forcebalance
        A(2:cc+1).*x(2*cc+3:3*cc+2) ...            % p(i+1)*A((i+1)
        - A(1:cc).*x(2*cc+2:3*cc+1) ...            %-p(i)*A(i)
        - ((x(2*cc+3:3*cc+2)+x(2*cc+2:3*cc+1))./2) ...
        .*(A(2:cc+1)-A(1:cc)) ...                  %-((p(i+1)+p(i))/2)*
         ...                                       %(A(i+1)-A(i))
        + rho*As.*x(cc+2:2*cc+1).^2 ...            %+rho*As(i)*Vs(i)^2
        + rho.*A(1:cc).*x(1:cc).^2;                %+rho*A(i)*V(i)^2
```

```
                                                               %=0

        %skinpressure
        (x(2*cc+3:3*cc+2)+x(2*cc+2:3*cc+1))./2  ...   % (p(i+1)+p(i))/2
50      -  R1*x(cc+2:2*cc+1).^2   ...                 %- R1*Vs(i)^2
        -  R2*x(cc+2:2*cc+1);                         %- R2*Vs(i)
                                                      %=0

        %initial conditions
55      x(3*cc+2)-endpressure;                        %p(end)=endpressure
        x(1)-startspeed;                              %v(1)  =startspeed

    ];
```

```
1   %*************************************************************************
    %* Description: pressure and speed calculator for a duct flow          *
    %* author:      Jeroen Bink                                            *
    %* context:     Master Thesis TuDelft @ Actiflow B.V.                  *
5   %* date:        June 2008                                              *
    %* version:     0.1                                                    *
    %* to compile:  mcc -B csharedlib:flowmodellib flowmodel.m             *
    %*************************************************************************

10  function [V,Vs,p] = ...
    solveEquationsA(A, As, rho, R1, R2 ,endpressure, startspeed, cc)
    %-------------------------------------------------------------------
    % return arguments:
    % V:  vector with cellnumber+1 ductspeeds
15  % Vs: vector with cellnumber speeds through porous skin
    % p:  vector with cellnumber +1 pressures in the duct
    %
    % input arguments:
    % A:  vector with pipe geometry (hights or, surfaces from intersections)
20  %             1 to   cellcount+1 = cellhights(z) or cellsurfaces, A(i)
    %
    % As: cel length(x) or cellsurface (in case of surface, A must be surfaces)
    %
    % rho:          density of flow medium
25  % R1,R2:        friction coefficients from porous skin
    % endpressure:  pressure at the last cell
    % startspeed:   inlet speed at the first cell (0 for closed duct)
    % cc:           celcount, the number of cells in the model
    %-------------------------------------------------------------------
30
    %initial guess for fsolve optimalisation
    x0=ones(cc*3+2,1);
    x0(2*cc+2:3*cc+2)=100;

35  %optimalisation routine
    x= ...
    fsolve(@(x)solvecellsuniversal(x, A, As, rho, R1, R2 ,endpressure,startspeed,cc),x0);

    %mapping output of optimalisation to correct return parameter vector
40  V= x(1:cc+1);
    Vs=x(cc+2:2*cc+1);
    p =x(2*cc+2:3*cc+2);
```

Airflow quality measurement techniques in wind tunnels

To determine the quality of boundary layer suction, different airflow properties are to be measured. Most important the amount of boundary layer reduction of the system needs to be determined. Local dynamic pressure measurements are needed at a small distance from the ground plane of the test section to determine the near ground air speeds.

The undesired effects of ground plane boundary layer suction in a wind tunnel are also a measure of the quality of such a system. Most important they include static pressure gradients and flow angularities. Methods used in wind tunnels to measure static pressure, dynamic pressure and flow angularities are explored in this section.

C.1   Static pressure measurement

One of the oldest devices for measuring pressures, and one of the easiest to build, is a manometer, a term normally applied to a device used to measure differential pressure [3]. Figure C.1 shows a U-tube manometer. A glass tube is bend in a u-shape and filled with a liquid. The pressure difference at the two ends of the tube can be measured by the difference in height of the liquid.
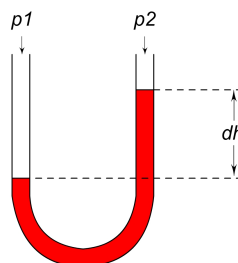

Figure C.1: U-tube manometer

A pressure measurement device which generates an electrical signal, is called a pressure transducer. The term transducer is explained by the conversion of a pressure difference, into an

electronic signal [11]. This conversion is needed to build systems in which the pressure information needs to be processed without human intervention. The most common used pressure transducers are of the diaphragm type, which means that the basic sensing mechanism is a thin sheet of material that deforms as the pressure across it changes [3]. A diaphragm is illustrated in figure C.2.
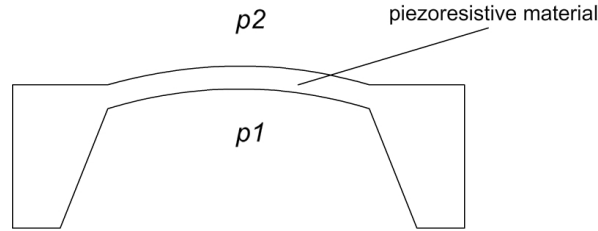

Figure C.2: bended diaphragm due to a pressure difference

These diaphragms can be made with a piezoresistive material like silicon or metal. The most frequently used silicon pressure sensors are based on piezoresistors diffused into a thin silicon diaphragm, which is obtained by chemical etching technologies [11]. The resistivity is a function of the deformation of the piezoresistive layer. When a piezoresitive material bends the length, L increases while the cross section, O, decreases. This causes an increment of the resistance, R.

$$R = \frac{\rho_L}{O} \Omega$$

This effect can also be seen in metal, however the specific resistivity, ρ, in silicon also has a positive strain sensitivity. This leads to a larger resistance response to the deformation in silicon than in metal. The response factor to deformation of the diaphragm is called the *gauge factor, K*.

$$K = \frac{dR/R}{\epsilon_L}$$

with dR/R, the relative difference in resistance, and ϵ_L the relative increase of the length.

So silicon diaphragm-type pressure sensors can be made cheaper than metal ones, also the higher gauge factor of silicon can be an advantage. A disadvantage however is that silicon pressure sensors are more susceptible to drift than the typical stainless steel diaphragm transducers. Therefore the silicon sensors needs a higher frequency of calibration [3].

In addition to pressure transducers with a resistive output, pressure transducers with a capacitive output can be made. A diaphragm also forms an electrical capacitance with its surroundings. When the diaphragm bends, due to a pressure change, this capacitance also changes. This change can be determined and is a measure of the pressure change. A sensor can be built with a parallel plate capacitor as shown in figure C.3. The capacitive effect is between 10 to 20 times more sensitive than the piezoresistive effect, but needs additional circuitry to turn the change in capacitance into an electronic signal [11].

C.2   Dynamic pressure measurement

Flow speed uniformity is as said before an important property of a wind tunnel test section. Differences in flow speed due to boundary layer development over the ground plane of the
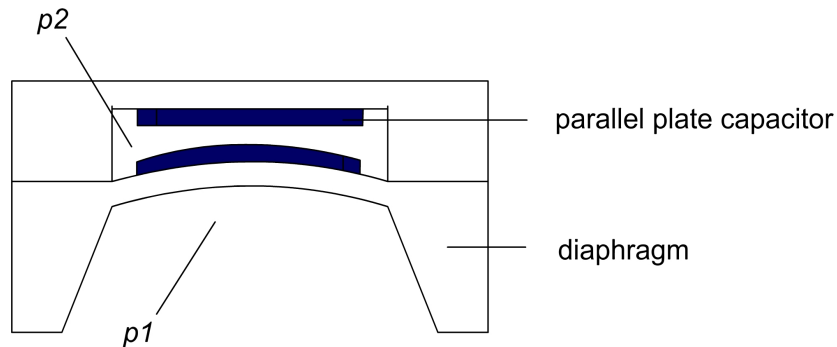
Figure C.3: diaphram with bended capacitor

test section is of special interest in this research. In most wind tunnels flow uniformity is measured by pitot static (Prandtl) tubes. A pitot static tube measures the total pressure and the static pressure. When these two are subtracted, the result is an estimate of the dynamic pressure q.

$$q = \tfrac{1}{2}\rho V^2$$

with q the dynamic pressure and ρ the density of air. The flow speed, V, can be derived from the dynamic pressure. A pitot-static tube is shown in figure C.4.
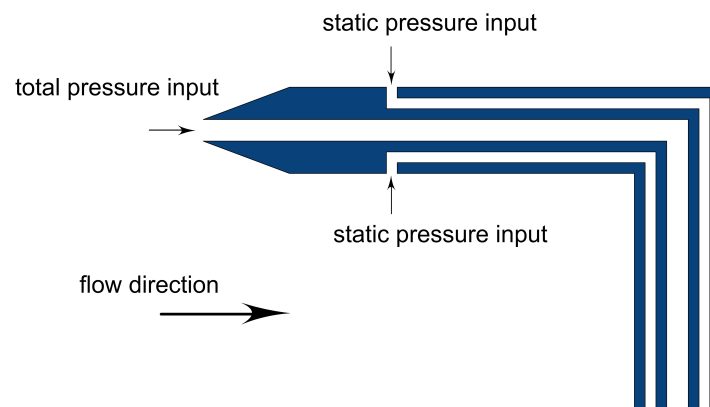
Figure C.4: pitot-static tube

For boundary layer measurement a rake with multiple pitot tubes can be constructed and placed in a wind tunnel as shown in figure C.5. Because the flow speed near the ground plane is of special interest the pitot tubes in this area are closer to each other, the higher situated tubes are mainly measuring the free stream velocity. The tubes can be placed as close as 1 or 2mm to a surface. At 2 mm above the ground plane, typical flow speed values would be 98 or 99 percent of the free stream velocity.
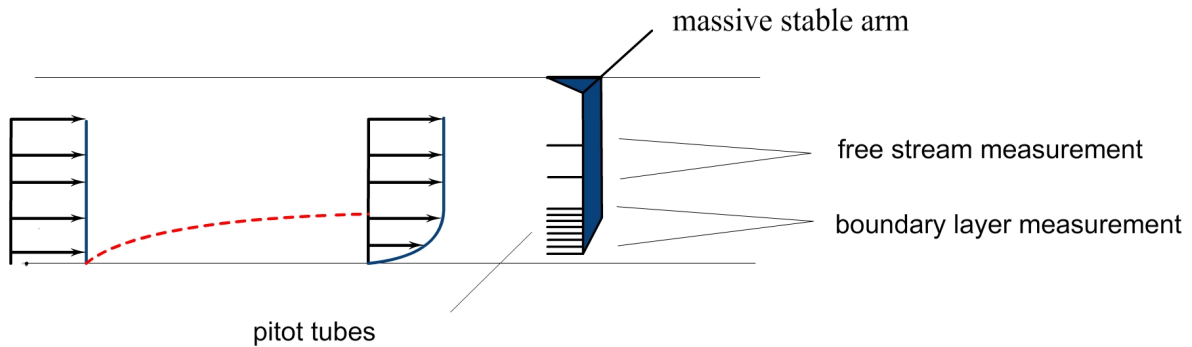
Figure C.5: a pitot tube configuration in a wind tunnel test section

C.3   Angularity measurement

To measure flow angularity different types of devices are used in wind tunnels, including yaw heads, claws and thermal anemometers. Yaw heads and claws make use of 2 or more pressure tubes placed in a fixed angle to each other. When a flow with no angularity is applied, the difference between these tubes should be zero. Calibration to this zero value is required. From the relative pressure differences the flow angularity can be derived. Thermal anemometers use hot wires or hot films, in which the temperature response is a function of the air speed. Multiprobe anemometers can be used to detect flow angularities [3].

Appendix D

Specifications of the used hardware

D.1   duct composition

porous upper side

movable plates

hose connection

actuator 1

actuator 2

under side

D.2   pump characteristics

Kodering
EPN 250/250-4

kunststof ventilator
aansluitdiameter
type schoepenwiel
pooltal motor
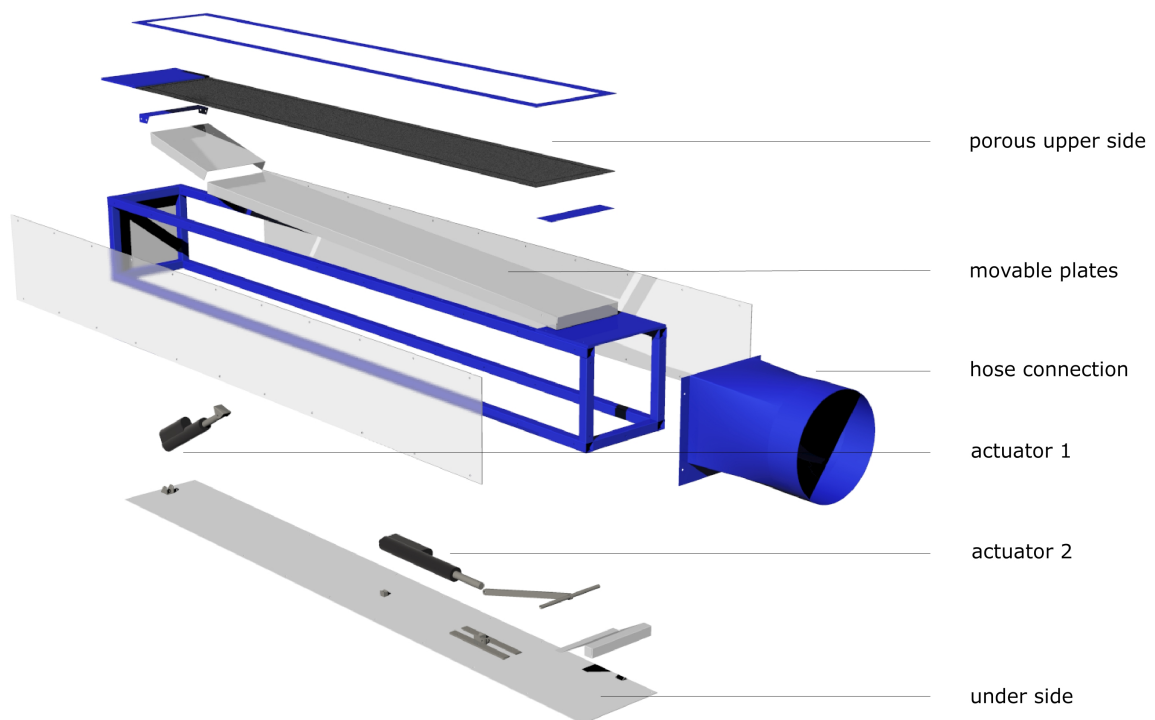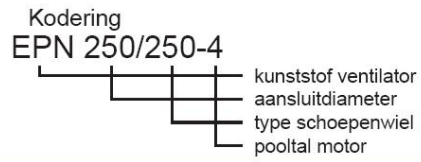
EPN 250/250

Technische specificatie

RPM	P_{motor}
(min^{-1})	(kW)
2850	**2,2 - 2p**
2500	1,5
2200	1,1
1800	0,75
1450	**0,37 - 4p**
1200	0,25
950	**0,18 - 6p**
750	**0,18 - 8p**

$\boxed{D}$ = Direkt gedreven
$\boxed{R}$ = Indirekt gedreven
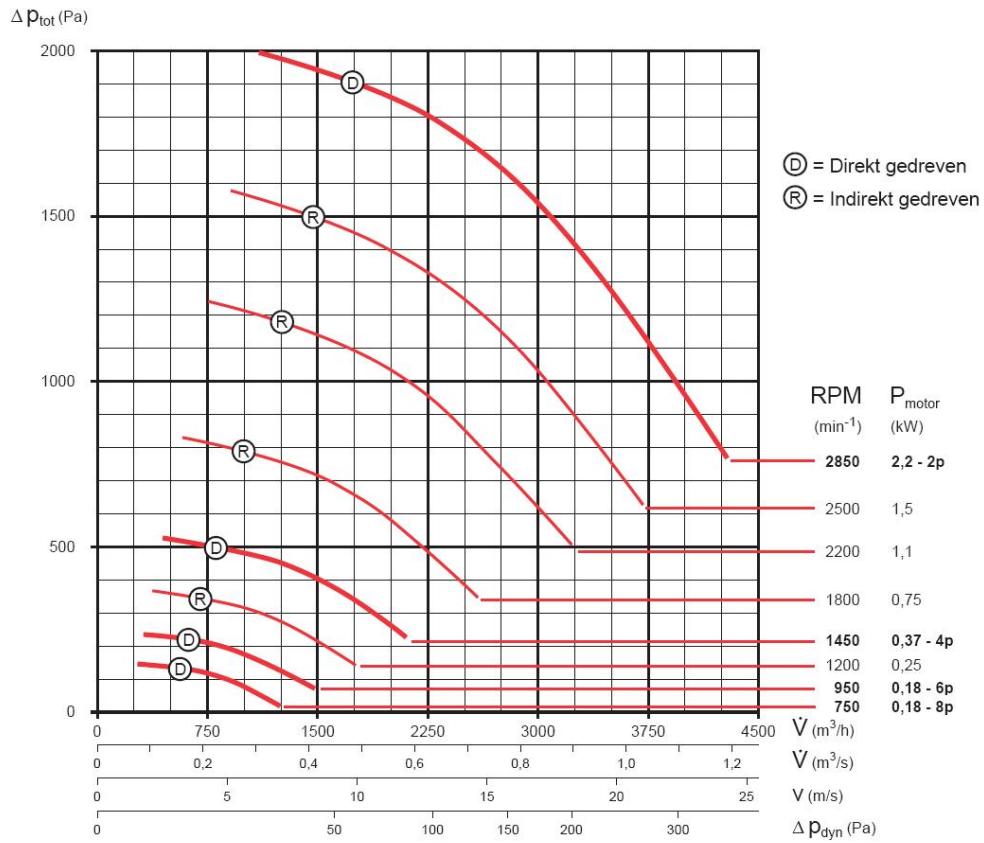
D.3   actuators

Electrak LA1-S and LA1-SP

Technical data

Available input voltages [Vdc]	12, 24 or 36
Available screw types	Acme
Max. static load at fully retracted [N]	1300
Min. / max. standard stroke [inch] S-model SP-model	 1 / 6 2 / 6
Duty cycle @ 25° C [%]	25
Temperature limits at operation [°C]	- 25 to + 65
Protection degree	IP65
Max. end play [mm]	0,9
Restraining torque [Nm] S-model SP-model	 2,3 –
Wire cross section [mm²]	1
Wire length [mm]	100
Connector included	yes

Features for both LA1-S and LA1-SP

- Small
- Weather resistant (IP65)
- Withstand 96 hour salt spray test
- Motor with auto reset thermal overload protection
- Self locking acme screw
- Can operate in a large temperature range
- Accepts large input voltage variations
- Maintenance free
- Models with higher load capacity possible on demand

Features for LA1-S

- End of stroke limit switches
- Six standard strokes

Features for LA1-SP

- Potentiometer feedback
- Anti rotation mechanism
- Three standard strokes

Options

- Custom RAL color

Engineering notes

- No clutch

Performance table

Model	Max. dynamic load [N]	Speed @ min. load [mm/s]	Speed @ max. load [mm/s]
S(P)12–09A04	110	75	52
S(P)24–09A04	110	75	52
S(P)12–09A08	225	45	33
S(P)24–09A08	225	45	33
S(P)12–17A08	340	26	17
S(P)24–17A08	340	26	17
S(P)12–17A16	340	14	7
S(P)24–17A16	340	14	7

Standard strokes

LA1-S ordering stroke	Actual stroke S [mm]
01	21
02	46
03	72
04	97
05	122
06	148

LA1-SP ordering stroke	Actual stroke S [mm]
02	59
04	115
06*	171

* not possible with gear ratio 16:1

D.4   actuator drivers
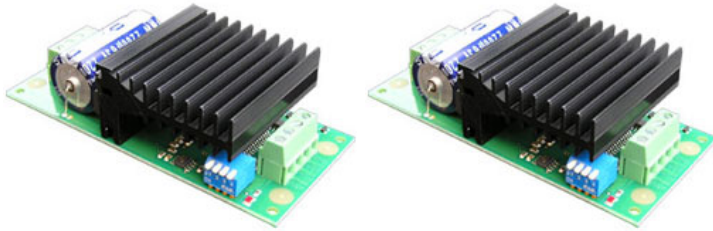
The MD03 is a medium power motor driver, designed to supply power beyond that of any of the low power single chip H-Bridges that exist. Main features are ease of use and flexibility. The motor's power is controlled by on-board Pulse Width Modulation (PWM) generators driving the H-Bridge Transistors.

Features Voltage - 5v logic supply and 5v - 50v for the motor
Current - 50mA Max for logic and up to 20A for the motor
Control 1 - 0v - 2.5v - 5v
Analogue for Reverse - Stop - Forward
Control 2 - 0v - 5v (or PWM equiv.) with separate direction control Control 3 - RC Mode - Controlled by standard Radio Control system. Direct connection to RC receiver. (1mS - 2mS pulse with 1.5mS center off).
Control 4 - I2C Interface, full control, acceleration and status reporting. Up to 8 modules on bus. SCL speed up to 1MHz
Current limiter - Preset at 20A
Temperature limiter - Reduces power gracefully if module overheats
Size - 113mm x 52mm x 30mm

D.5   digital pressure array

Model **DSA® 3217/3218**

Digital Sensor Array
Data Sheet No. G 511

Scanivalve Corp.

Digital Pressure Measurement

Features

• Intelligent pressure modules

• Ethernet TCP/IP Protocol "Network Ready"

• 0 - 750 psi pressure range

• Temperature compensated pressure sensors

• Dual pressure ranges available

• ±.05% full scale long term accuracy

• Time stamped data available

• 500 samples/channel/second EU

DSA3217 (Shown)

General Description

The DSA3200 series pressure acquisition systems represent the next generation of multi-point electronic pressure scanning. Model DSA3217/3218, Digital Sensor Array, incorporates 16 temperature compensated piezoresistive pressure sensors with a pneumatic calibration valve, RAM, 16 bit A/D converter, and a microprocessor in a compact self-contained module. The result is a network ready intelligent pressure scanning module.

The microprocessor compensates for temperature changes and performs engineering unit conversion. The microprocessor also controls the actuation of an internal calibration valve to perform on-line zero and multipoint calibrations. This on-line calibration capability virtually eliminates sensor thermal errors with a long term system accuracy of ±.05% FS.

Pressure data are output in engineering units via Ethernet using TCP/IP protocol.

Scanivalve offers an optional multi-range calibration. This allows the DSA modules to have multiple pressure ranges. The calibration valve and transducers are manifolded in groups of 8. The user can specify up to 3 pressure ranges within that group of 8 as long as the ratio for all 3 full scale ranges doesnt exceed 3:1 from highest to lowest range.

Applications

The DSA3217/3218 Digital Sensor Array is ideal for flight and turbine engine testing applications, where ambient temperatures vary. It is also ideal for industrial pressure measurement where long calibration intervals are required or temperatures can vary greatly. The DSA temperature compensated pressure sensors are more than ten times less sensitive to temperature than typical piezoresistive pressure sensors. They are not attitude sensitive, so the units may be close coupled to the pressure sources to be measured.

When further temperature stability is required or for use below 0°C, it is recommended that the Model DSA3218 be used. The Model DSA3218 is basically a DSA3217 installed in an insulated, environmental box. All Px input and control pressure fittings are 1/8 inch Swagelok® fittings. Optional DSA3218 fittings are 1/16 and 1/4 inch Swagelok® fittings.

DSA® is a registered trademark of Scanivalve Corp.
Windows® and MS-DOS® are registered trademarks of Microsoft Corp.
VEE® is a registered trademark of Agilent.
LabVIEW® is a registered trademark of National Instruments.
Swagelok® is a registered trademark of Swagelok Corp.

D.6 controller used for position control and feedback control

EX9188A8D Support 8 RS232/485 devices
COM1 can be used to download program and can be RS232 port
Watchdog support for system recovery
CPU 80188, 40MHZ
SRAM 256KB
FLASH ROM 512KB
EEPROM 2KB
RTC
EMBEDDED OS RomDos(Datalight)
3000V Isolation option
Advantech / ICP fully compatible
Series: EX9188A8D-512, EX9188B8D, EX9188B8D-512, EX9188C8D, EX9188C8D-512

Bibliography

[1] Aerodynamic testing of road vehicles - testing methods and procedures. *SAE, Surface Vehicle Information Report*, 1993.

[2] Adaptive wall technology for improved wind tunnel testing techniques - a review. *Elsevier Science*, 1995.

[3] Jewel B. Barlow, W.H. Rae Jr., and Alan Pope. *Low-Speed Wind Tunnel Testing, third edition*. 1999.

[4] Trevor J. Bender. The new lola cars 50 percent scale aerodynamic wind tunnel. *SAE International*, 2000.

[5] Geoffrey W. Carr and Winfried Eckert. A further evaluation of the ground-plane suction method for ground simulation in automotive wind tunnels. *SAE International*, 1994.

[6] W. Eckert, N. Singer, and J.D. Vagt. The porsche wind tunnel floor-boundary-layer control - a comparison with road data and results from moving belt. *SAE International*, 1992.

[7] W.T. Eckert and E. Mercker. The effect of groundplane boundary layer control on automotive testing in a wind tunnel. *SAE International*, 1988.

[8] Gene F. Franklin, J. David Powell, and Abbas Emami-Naeini. *Feedback Control of Dynamic Systems, Fifth edition*. 2006.

[9] Guy L. Larose and Bernard Tanguay. the new boundary layer control system for nrc's 9m x 9m wind tunnel. *AIAA Journal*, 2001.

[10] Edzard Mercker and Jochen Wiedemann. Comparison of different ground simulation techniques for use in automotive wind tunnels. *SAE International*, 1990.

[11] S. Middelhoek, S.A. Audet, and P.J. French. *Silicon Sensors, Lecture*. 2000.

[12] E. Terry, R. Campe, O. van Dijk, and J. Bink. Boundary layer control for wind tunnels. *patent EP08075165*, 2008.

[13] P.M. Wadby-Smith and W.J. Rainbird. Some principles of automotive aerodynamic testing in wind tunnels with examples from slotted wall test section facilities. *SAE Technical Paper Series*, 1985.

[14] Frank M. White. *Fluid mechanics third edition*. 1994.

[15] Gerhard Wickern and Norbert Lindener. The audi aeroacoustic wind tunnel: Final design and first operational experience. *SAE International*, 2000.

[16] Jochen Wiedemann and Oliver Fischer. Further investigations on gradient effects. *SAE International*, 2004.